Earth-Science Reviews 150 (2015) 68–94

Contents lists available at ScienceDirect

Earth-Science Reviews

journal homepage: www.elsevier.com/locate/earscirev

The role of Indian and Tibetan lithosphere in spatial distribution of Cenozoic magmatism and porphyry Cu–Mo deposits in the Gangdese belt, southern Tibet

Rui Wang [a,*], Jeremy P. Richards [a], Li-min Zhou [b], Zeng-qian Hou [c], Richard A. Stern [a], Robert A. Creaser [a], Jing-jing Zhu [d]

[a] Department of Earth and Atmospheric Sciences, University of Alberta, Edmonton, Alberta, T6G 2E3, Canada
[b] National Research Center for Geoanalysis, Chinese Academy of Geological Sciences, Beijing 100037, PR China
[c] Institute of Geology, Chinese Academy of Geological Sciences, Beijing 100037, PR China
[d] State Key Laboratory of Ore Deposit Geochemistry, Institute of Geochemistry, Chinese Academy of Sciences, Guiyang 550002, PR China

ARTICLE INFO

Article history:
Received 7 November 2014
Received in revised form 24 June 2015
Accepted 2 July 2015
Available online 18 July 2015

Keywords:
Gangdese
Indian and Tibetan lithosphere
Miocene
Os–Sr–Nd–O–Hf isotopes
Porphyry deposits

ABSTRACT

The 1600 km-long Gangdese magmatic belt features extensive Paleocene–Eocene I-type intrusive rocks and coeval volcanic successions, abundant but more localized Oligo-Miocene calc-alkaline to alkaline plutons, and Miocene potassic to ultrapotassic volcanic rocks. These Cenozoic igneous rocks record geodynamic changes related to the India–Asia collision which began at ~55–50 Ma. New and published lithogeochemical and multiple isotopic (Os–Sr–Nd–O–Hf) analyses of these Cenozoic igneous rocks reveal that the Paleocene–Eocene magmas have similar compositions to continental arc rocks throughout the belt, but later Miocene magmas show sharp longitudinal contrasts in geochemical and isotopic compositions, which are also correlated with the occurrence of porphyry-type mineralization.

Sparse Miocene high-K calc-alkaline to shoshonitic volcanic rocks in the eastern Gangdese belt have low to moderate $(^{87}Sr/^{86}Sr)_i$ ratios (0.7057–0.7121), moderately negative εNd_i values (−9.4 to −3.4), low $(^{187}Os/^{188}Os)_i$ ratios (0.154–0.210), highly variable εHf_i values (−5.9 to +10.1), and low zircon $\delta^{18}O$ values (+5.0–+6.7‰), which are interpreted to reflect derivation by partial melting of subduction-modified Tibetan sub-continental lithospheric mantle (SCLM). In contrast, Miocene high-K calc-alkaline to shoshonitic volcanic rocks in the western Gangdese belt have higher $(^{87}Sr/^{86}Sr)_i$ ratios (0.7069–0.7263), more negative εNd_i values (−17.5 to −6.0) and εHf_i values (−15.2 to +0.7), and crust-like zircon $\delta^{18}O$ values (+6.2–+8.8‰), but mantle-like $(^{187}Os/^{188}Os)_i$ values (0.156–0.182), and high Ni and Cr contents. These features suggest that potassic to ultrapotassic magmas in the western Gangdese belt were also derived from partial melting of Tibetan SCLM but with ~3–25% input of melts ± fluids from the underthrust Indian plate ($^{87}Sr/^{86}Sr$ = 0.74–0.76, εNd = −18 to −10, $\delta^{18}O$ = +10 – +14‰). In contrast, Miocene alkaline magmas to the east were unaffected by this source.

Oligo-Miocene calc-alkaline to high-K calc-alkaline granitoids related to large porphyry Cu–Mo deposits in the eastern Gangdese belt (east of ~89° E) are geochemically broadly similar to the early Paleocene–Eocene rocks. They are thought to be derived from partial melting of subduction-modified lower crust with mixing of alkaline melts from partial melting of SCLM, and have relatively low $(^{87}Sr/^{86}Sr)_i$ ratios (0.7047–0.7076), high εNd_i values (−6.1 to +5.5) and εHf_i values (1.4–8.7), moderate $(^{187}Os/^{188}Os)_i$ ratios (0.224–0.835), and low zircon $\delta^{18}O_{VSMOW}$ values (+5.5–+6.6‰). These magmas also had high water contents (weak Dy/Yb enrichment, characterized with amphibole fractionation) and oxidation states (ΔFMQ 0.8–2.9), which explain their unique association with porphyry Cu–Mo mineralization. In contrast, Miocene high-K calc-alkaline to shoshonitic granitoids in the western Gangdese belt (west of ~89° E) show differences in geochemical and isotopic compositions to the earlier Paleocene–Eocene magmatism, and are characterized by crust-like zircon $\delta^{18}O$ values (+6.2–+8.8‰), high $(^{87}Sr/^{86}Sr)_i$ ratios (0.7147–0.7165), negative εNd_i values (−11.3 to −7.9), crust-like $(^{187}Os/^{188}Os)_i$ values (0.550–1.035), and low εHf_i values (−13.0 to 3.9). These magmas are interpreted to reflect involvement of melts ± fluids from the underthrust Indian plate and high degrees of crustal contamination upon emplacement. Only one small porphyry Cu–Mo deposit is known to be associated with these western granitoids. We suggest that this difference reflects the variable extent of underthrusting of the Indian plate continental lithosphere beneath Tibet in the Oligo-Miocene, and diachronous breakoff of the Greater India slab. In the absence of

* Corresponding author at: Mineral Resources Flagship at CSIRO, Dick Perry Avenue, Kensington, WA 6151, Australia.
E-mail addresses: rw5@ualberta.ca, Rui.Wang@csiro.au (R. Wang).

http://dx.doi.org/10.1016/j.earscirev.2015.07.003
0012-8252/© 2015 Elsevier B.V. All rights reserved.

underthrust Indian lithosphere to the east of ~89° E in the Oligo-Miocene, slab breakoff triggered asthenospheric upwelling and partial melting of previously subduction-modified Tibetan lithosphere, generating hydrous, oxidized calc-alkaline magmas with the potential to generate porphyry Cu–Mo deposits. In contrast, underthrusting of the Indian plate to the west at this time limited the involvement of asthenospheric melts and the extent of partial melting of subduction-modified lithosphere, with the result that melts ± fluids derived from the underthrust lithosphere were infertile.

© 2015 Elsevier B.V. All rights reserved.

Contents

1. Introduction

The Gangdese magmatic belt is located along the southern margin of the Tibetan plateau, and records a series of magmatic events starting with Late Triassic–Early Jurassic subduction of the Neo-Tethyan ocean (Chu et al., 2006), followed by early collision of Greater India and oceanic slab breakoff in the Eocene ("soft collision" at ~55–50 Ma; Allégre et al., 1984; de Sigoyer et al., 2000; Gao et al., 2008; Van der Voo et al., 1999). "Hard-collision" of the Indian craton with the Asian margin occurred at ~35 Ma (Replumaz et al., 2010; van Hinsbergen et al., 2012), with late-collisional processes in the Oligocene and Miocene. Breakoff of the Greater India slab started in the western part of the belt at ~25 ± 5 Ma, and the tear propagated eastward until final detachment beneath eastern Tibet at ~10 ± 5 Ma (Van der Voo et al., 1999; Replumaz et al., 2010). A large number of small-volume calc-alkaline to high-K alkaline and shoshonitic granitoids and high-K calc-alkaline to shoshonitic lava flows were intruded or erupted in the Gangdese belt between ~30 and 9 Ma, and constitute a 1600 km-long late (or post)-collisional magmatic belt (Fig. 2; Chung et al., 2003, 2005; Ding et al., 2003; Gao et al., 2007; Guo et al., 2013; Hou et al., 2004, 2009; Leng et al., 2013; Li et al., 2011; Liu et al., 2011; Miller et al., 1999; Turner et al., 1996; Wang et al., 2014a, 2014b, 2014c; Williams et al., 2004; Wu et al., 2014; Yang et al., 2009; Zhao et al., 2009; Zheng et al., 2012; Zheng et al., 2014a)

The Oligo-Miocene igneous rocks in the Gangdese belt show a sharp longitudinal distinction in petrography, geochemistry, and association with porphyry-type mineralization, with a boundary at ~89° E. The eastern Gangdese group (longitude ~89°–94° E) is characterized mainly by intermediate–felsic calc-alkaline to high-K calc-alkaline plutons (which are locally associated with porphyry Cu–Mo deposits), and minor high-K calc-alkaline to shoshonitic volcanic rocks. These calc-alkaline to high-K calc-alkaline granitoid magmas are characterized by high Sr/Y and $[La/Yb]_N$ ratios (e.g. Chung et al., 2003; Hou et al., 2004, 2009; Li et al., 2011; Wang et al., 2014b). In contrast, the western Gangdese group (longitude ~80°–89° E) is characterized mainly by high-K calc alkaline to shoshonitic volcanic rocks and sparse porphyritic plutons that are mostly barren. These alkaline volcanic rocks have high Th and K_2O contents, and low to moderate Sr/Y ratios (Miller et al., 1999; Williams et al., 2004; Guo et al., 2013; Wang et al., 2014b). The cospatial porphyritic plutons with similar mineralogical and geochemical compositions to the western alkaline volcanic rocks are likely their equivalents (e.g. Wang et al., 2012; Yu et al., 2013).

Previous isotopic studies of Miocene potassic to ultrapotassic volcanic rocks in the western Gangdese belt demonstrate that their compositions are characterized by extremely low εNd_i values (−17.4 to −7.1), but high $(^{87}Sr/^{86}Sr)_i$ and $\delta^{18}O_{VSMOW}$ values (0.7068–0.7399 and +8–+11‰, respectively) (e.g., Miller et al., 1999; Williams et al., 2004; Zhao et al., 2009). These compositions suggest that the Indian lithosphere (with low εNd = −18 to −10, and high $^{87}Sr/^{86}Sr$ = 0.74–0.76 and $\delta^{18}O$ = +10–+14‰; France-Lanord et al., 1988; Inger and Harris, 1993) was a likely source. Prior to this study, it was not clear whether eastern Gangdese belt Miocene magmatism was also affected by this source, partly because there are few reported occurrences of Miocene potassic to ultrapotassic rocks in this part of the belt. Oligo-Miocene granitoids from the eastern Gangdese belt have been studied for Sr–Nd isotopic compositions, but no O isotopic data have been published. In addition, many of these previously studied intrusive rocks are associated with porphyry-type deposits and have been affected by pervasive hydrothermal alteration, rendering whole-rock Sr and O isotopic compositions suspect.

In this study, we collected fresh and minimally altered Cenozoic igneous rocks from throughout the 1600 km-long Gangdese magmatic belt, focusing on previously unsampled occurrences of Miocene rocks. By combining our new data with published lithogeochemical and multiple isotopic (Os–Sr–Nd–O–Hf) analyses, we show that differential involvement of Indian plate lithosphere, subduction-modified Tibetan lithosphere, and asthenospheric melts explains the observed spatial and temporal distribution of magmatism, and restriction of porphyry-type mineralization to the eastern Miocene Gangdese belt.

2. Tectonic setting

The Himalayan–Tibetan orogen is composed of the Himalayas, Lhasa terrane, Qiangtang terrane, and Songpan–Ganze complex, from south to north, separated from each other by the Indus–Yarlung Zangbu, Bangong–Nujiang, and Jinsha River sutures (Yin and Harrison, 2000; Fig. 1). The geological setting of the Lhasa terrane has been described in detail by several authors (e.g., Pan et al., 2004; Mo et al., 2005, 2007, 2008; Wen, 2007; Zhu et al., 2011, 2013; Zhang et al., 2013; Wang et al., 2014a), and is only briefly summarized here. The core of the Lhasa terrane is thought to consist of Archean and Proterozoic crystalline basement that rifted from the Gondwana margin in the Carboniferous–Middle Permian or earlier (Zhu et al., 2010), and was covered by Paleozoic and Mesozoic metasedimentary and volcanic rocks (Pan et al., 2004; Zhu et al., 2009, 2011). The Lhasa terrane is thought to have collided with the Qiangtang terrane to the north in the Early Cretaceous (Yin and Harrison, 2000; Kapp et al., 2005), and northward subduction of Neo-Tethyan oceanic lithosphere beneath its southern margin began in the Late Triassic or Early Jurassic (Chu et al., 2006). This Andean-style continental subduction produced voluminous Mesozoic–Cenozoic I-type plutons and coeval volcanic rocks, which constitute the 1600 km-long Gangdese magmatic belt (Pan et al., 2004; Mo et al., 2005; Wen, 2007; Zhu et al., 2011; Niu et al., 2013). Whole-rock Nd isotopic and zircon Hf isotopic compositions of crustal xenoliths in Neogene volcanic rocks (mostly εNd > −5, εHf = −5 to +20; Chan et al., 2009; C.Z. Liu et al., 2014; Mo et al., 2005, 2007, 2008; Zhu et al., 2011) suggest that the crust beneath the Gangdese belt is mostly juvenile.

The India–Asia collision started at ~55–50 Ma when the Greater India plate (Indian continental margin; Ali and Aitchison, 2005) first collided with the Lhasa terrane ("soft collision": Meng et al., 2012; van Hinsbergen et al., 2012). The thicker and more rigid Indian craton (plate) later began to underthrust the Asian margin at ~35 Ma ("hard collision": Replumaz et al., 2010; van Hinsbergen et al., 2012). Following detachment of the Greater India slab in the Oligo-Miocene, the Indian plate continued to underthrust the Lhasa terrane to the present day (Kind and Yuan, 2010; Replumaz et al., 2010; Zhao et al., 2010). Seismic tomographic studies indicate that the Indian continental lithosphere (100 to 200 km thick) extends northward below the Tibetan plateau, but the extent of underthrusting decreases from west (reaching ~33° N at ~87° E, to the north of the Bangong–Nujiang suture) to east (reaching ~30° N at ~93° E), with a NE-directed convergence vector

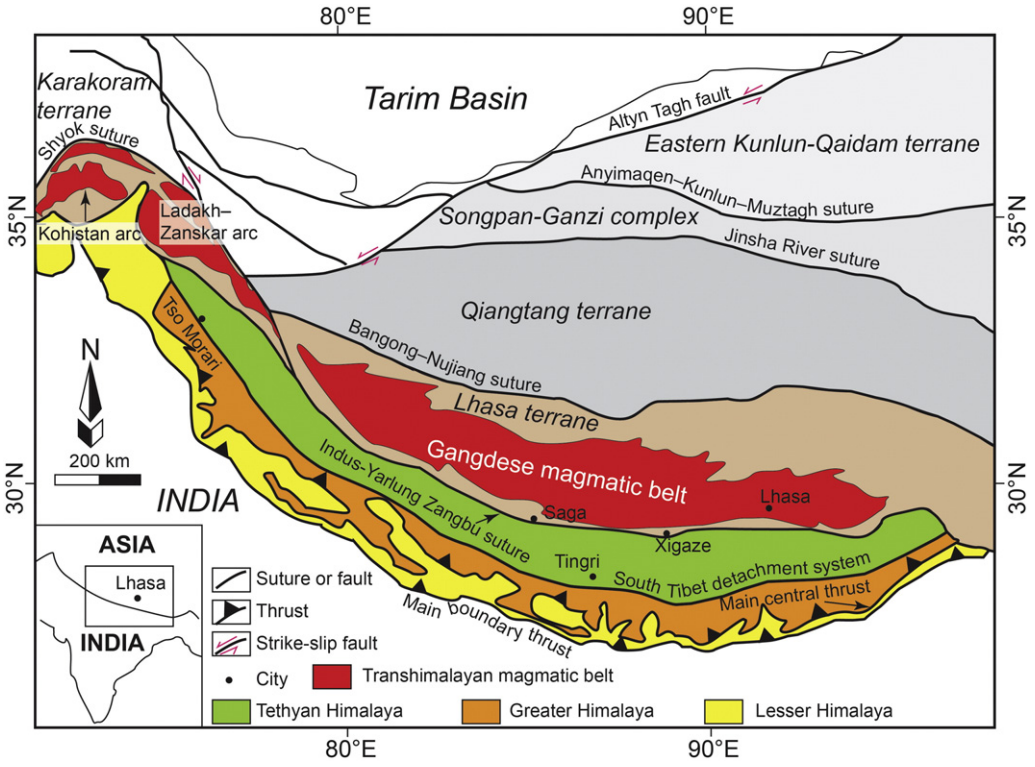

Fig. 1. Map indicating major tectonic units, boundaries, and magmatic belts within the Tibet–Qinghai Plateau. Modified from Aitchison et al. (2007), White et al. (2011) and Wang et al. (2014a).

(Kumar et al., 2006; Li et al., 2008; Huang et al., 2009; Kind and Yuan, 2010; Zhao et al., 2010; Shokoohi Razi et al., 2014). Orogen-parallel (east–west extension) began at ~19–4 Ma in response to plateau collapse or subcontinental mantle lithospheric delamination or Indian plate breakoff led to numerous north–south-trending extensional faults and rift basins, which facilitated the ascent of deeply derived magmas (Fig. 2; Armijo et al., 1986; Blisniuk et al., 2001; Burchfiel et al., 1991; Cogan et al., 1998; Copley et al., 2012; Tapponnier et al., 2001).

3. Magmatism

3.1. Pre-collisional magmatism

North-directed Neo-Tethyan subduction beneath southern Tibet produced voluminous Cretaceous calc-alkaline magmatism in the Lhasa terrane (Harris et al., 1986; Wen, 2007; Mo et al., 2008; Lee et al., 2011). Rollback of the Neo-Tethyan slab at ~69–53 Ma triggered a magmatic flare-up (Kapp et al., 2007; Wen, 2007), represented by extensive Paleocene–Eocene I-type intrusive rocks and widespread Linzizong volcanic successions (Fig. 2). The magmas through the whole Gangdese belt are characterized by moderate εNd_i values (−0.6 to +4.0), positive εHf_i values (+3.8 to +7.1), moderate $\delta^{18}O$ values (+5.0‰ to +6.5‰), and low Th/Y and La/Yb ratios (<20). These magmas were derived from the mantle with minor crustal contamination in response to Neo-Tethyan slab rollback as proposed by previous studies (Wen, 2007; Mo et al., 2008; Wang et al., 2015).

3.2. Syn-collisional magmatism

"Hard collision" between the Indian craton and the Asian margin at ~35 Ma generated a large number of small-volume calc-alkaline to alkaline intrusions and potassic to ultrapotassic volcanic rocks that were emplaced or erupted in southern Tibet during the Oligo-Miocene (Ding et al., 2003; Hou et al., 2009; Wang et al., 2014a, 2014b).

3.2.1. Granitoid plutons

Oligocene and Miocene granitoid plutons in the eastern Gangdese belt are calc-alkaline to high-K calc-alkaline (monzonites, quartz monzonites, granodiorites, granites; Fig. 2). They are associated with several large porphyry Cu–Mo deposits, and have low $(^{87}Sr/^{86}Sr)_i$ ratios (0.7047–0.7076), highly variable εNd_i values (−6.2 to +5.5), and high La/Yb and Sr/Y ratios (Hou et al., 2004; Li et al., 2011; Wang et al., 2014a, 2014b). Suggested petrogenetic models have included partial melting of a subducted oceanic slab (Qu et al., 2004, 2007), partial melting of slab melt-modified mantle sources (Gao et al., 2007, 2010), partial melting of thickened lower crust (Chung et al., 2003; Hou et al., 2004), and partial melting of subduction-modified Tibetan lithosphere (Guo et al., 2007; Hou et al., 2009; Li et al., 2011; Zheng et al., 2012; Wang et al., 2014a, 2014b). These intrusions formed ~35 m.y. after the onset of India–Asia collision, and cannot therefore be directly related to subduction or any relict oceanic lithosphere was present beneath this region. Therefore, partial melting of a subducted oceanic slab is not considered for the formation of these intrusions. Published Sr–Nd isotope compositions of Gangdese Oligo-Miocene igneous rocks overlap those of the cospatial Cretaceous Gangdese arc batholith, thus a source for these relatively evolved (chemically and isotopically) late-collisional magmas must be sought in either the previously subduction-modified Tibetan lithosphere, or the underthrust Indian lithosphere, or the asthenospheric mantle.

In contrast, there are no Oligocene granitoids in the western part of the belt, and few Miocene granitoids have been reported. Those that are known have high-K calc-alkaline to shoshonitic compositions (Zheng et al., 2007; Gao et al., 2010; Wang et al., 2012; Yu et al., 2013). The western granitoids are mostly barren, and little studied, but granodiorite intrusions in a small Zhunuo porphyry Cu–Mo deposit have moderate $(^{87}Sr/^{86}Sr)_i$ ratios (0.7071–0.7096), and negative εNd_i values (−7.4 to −4.1).

3.2.2. Alkaline volcanism

Sparse late Oligocene high-K calc-alkaline to shoshonitic volcanic rocks mainly occur in the Qiangtang terrane to the north of the western Gangdese belt, where no coeval granitoids are known (Fig. 2). They have basaltic trachyandesitic, tephriphonolitic, trachyandesitic, and trachytic compositions, moderate $(^{87}Sr/^{86}Sr)_i$ ratios (0.7060–0.7092), and negative εNd_i values (−9.2 to −3.8) (Ding et al., 2003; Liu et al., 2008). These alkaline volcanic rocks are thought to be derived from partial melting of enriched lithospheric mantle (Ding et al., 2003; Liu et al., 2008).

In contrast, alkaline volcanic rocks were erupted widely in the Miocene, especially in the western Gangdese belt (Fig. 2; minor occurrences also occur in the eastern part of the belt; Miller et al., 1999; Wang et al., 2014a; Williams et al., 2004; Zhou et al., 2004, 2009).

The western Miocene alkaline volcanic rocks have high $(^{87}Sr/^{86}Sr)_i$ ratios (0.7069–0.7399), low εNd_i values (−17.4 to −7.1), and low

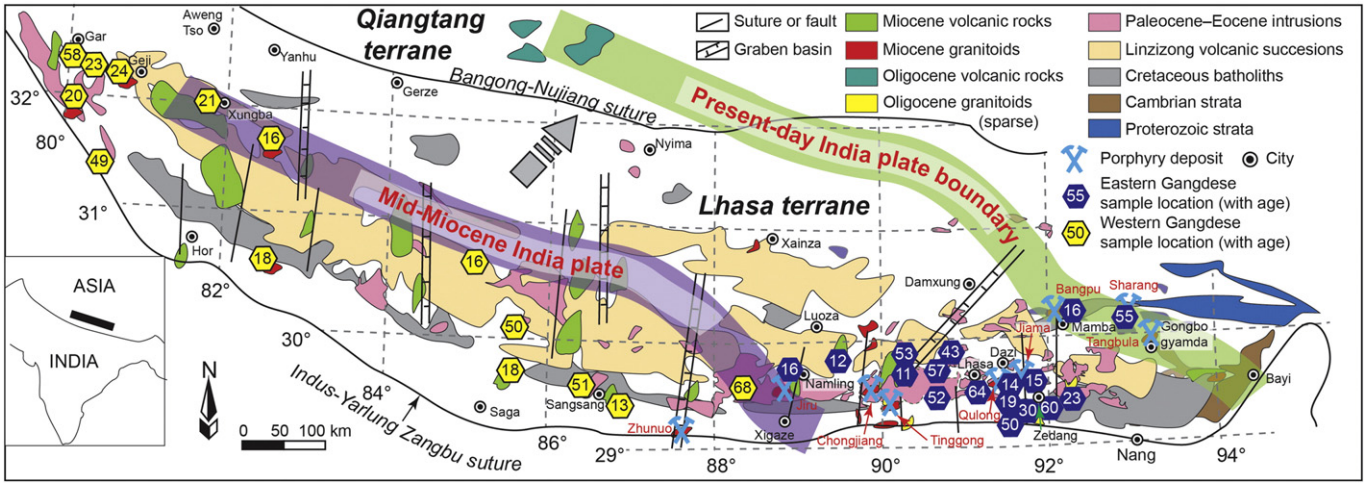

Fig. 2. Geology of the Gangdese magmatic belt in the Lhasa terrane, showing the locations of samples described in this paper (modified from Wang et al., 2014b; Zhao et al., 2009). The broad green line represents the present northern limit of the underthrust Indian plate beneath the Tibetan plateau, whereas the broad purple line is its estimated location in the mid-Miocene; the convergence direction is shown with a gray arrow (for details see Wang et al., 2014b). Yellow and blue hexagons with numerals mark the locations and ages of samples in the western Gangdese belt and eastern Gangdese belt, respectively (see Table 1 for precise locations, and sources of data from the literature). The locations of major porphyry Cu–Mo deposits in the Gangdese belt are also shown.

Sr/Y ratios, quite distinct from the eastern calc-alkaline to high-K calc-alkaline granitoids (Miller et al., 1999; Williams et al., 2004; Guo et al., 2013; Wang et al., 2014a, 2014b). Petrogenesis of these volcanic rocks is under debate, and their magmas have been interpreted to be derived from the Indian middle-lower crust (Hébert et al., 2014), enriched lithospheric mantle (e.g. Miller et al., 1999; Williams et al., 2004; Zhao et al., 2009), or India plate melt (±fluid)-modified mantle wedge (Guo et al., 2013). We think these alkaline volcanic rocks are rooted deeper than middle-lower crust, because many of these Miocene lavas carry crustal or mantle xenoliths (Chan et al., 2009; Liu et al., 2011; D. Liu et al., 2014) and also have high Cr and Ni contents. The mineralogy and geochemistry of peridotite xenoliths from the Salipu area suggest that a hydrous and metasomatized (i.e., phlogopite bearing) lithospheric mantle existed below this part of Gangdese belt at this time (Liu et al., 2011; D. Liu et al., 2014). In addition, the newly reported enriched O isotopic values ($\delta^{18}O = +.03 \pm 0.28‰$; C.Z. Liu et al., 2014) of olivine from Salipu xenoliths identified the metasomatized mantle, and suggest the subducted/underthrusted Indian continental material ($\delta^{18}O = +10–+14‰$; France-Lanord et al., 1988; Inger and Harris, 1993) is the most likely candidate for metasomatic melts.

Miocene alkaline volcanic rocks are sparse in the eastern Gangdese belt (Wang et al., 2014b; Yang, 2008; Zhou et al., 2009; Fig. 2), and little studied. The only reported Qulong high-Mg diorites have relatively low εNd_i values (−5.4 to −5.1), high ($^{87}Sr/^{86}Sr)_i$ ratios (0.70070–0.70720), and intermediate εHf_i values (−3.0–+5.9) (Yang et al., 2015), which are quite different from alkaline volcanic rocks in the western Gangdese belt.

4. Porphyry deposits

Paleocene–Eocene igneous rocks in the Gangdese belt are mostly barren, and only three small porphyry deposits have been discovered to date: the Yaguila Pb–Zn vein-type deposit (62.4 ± 0.6 Ma) with minor associated porphyry Mo mineralization (Huang et al., 2012), the Sharang porphyry Mo deposit (52.25 ± 0.31 Ma; 10 Mt @ 0.061% Mo; Zhao et al., 2011, 2014), and the Jiru porphyry Cu deposit (49.2 ± 1.7 Ma; 41.9 Mt @ 0.43 Cu; Zheng et al., 2014b).

In contrast, high-K calc-alkaline plutons in the Oligocene are associated with several porphyry and skarn Cu deposits in the eastern Gangdese belt, including the Nuri porphyry and skarn Cu deposit (23.36 ± 0.49 Ma; 79.4 Mt at 0.73% Cu; Li et al., 2006; Chen et al., 2011, 2012; Zhang et al., 2012), and the smaller Mingze, Liebu, and Chongmuda deposits.

The largest porphyry Cu–Mo deposits occur in association with Miocene calc-alkaline to high-K calc-alkaline intrusive rocks, and are mainly restricted to the eastern Gangdese belt (Fig. 2; Hou et al., 2009; Wang et al., 2014a). These include the Qulong porphyry Cu–Mo deposit (16.4 ± 0.5 Ma; 1420 Mt @ 0.5% Cu; Yang et al., 2009), the Jiama porphyry Cu–Mo deposit (14.8 ± 0.33 Ma; 1054 Mt @ 0.44% Cu; Ying et al., 2014), and several small- to medium-sized porphyry Cu–Mo deposits such as Bangpu, Tangbula, Lakang'e, Dabu, Gangjiang, Chongjiang, and Tinggong (as reviewed in Hou et al., 2009).

In the western part of the belt, Miocene high-K calc-alkaline to shoshonitic plutons are associated with only a few, small porphyry deposits (e.g., the Zhunuo porphyry Cu–Mo deposit; Zheng et al., 2007). Thus, significant porphyry and skarn Cu–Mo mineralization is restricted in space (east of ~89° E), time (Oligo-Miocene), and magmatic association (calc-alkaline to high-K calc-alkaline plutons) in the Gangdese belt.

5. Sampling and analysis strategy

Large amounts of lithogeochemical and geochronological data have been published on Cenozoic igneous rocks from the Gangdese belt (as reviewed in Wang et al., 2014a, 2014b, 2014c, 2015), but few whole-rock osmium isotope, zircon oxygen and hafnium isotope data exist. In particular, few such analyses have been reported for Miocene potassic and ultrapotassic volcanic and subvolcanic rocks from the eastern Gangdese belt. For this reason, sampling was focused on the latter lithologies, aiming to complement existing data from other areas (see Table 1 for sample locations). Fresh or minimally altered igneous rocks were selected, and mafic end-members of igneous suites were prioritized in order to evaluate least-evolved compositions. Six previously undated Miocene intrusions and volcanic rocks were selected for dating by the zircon U–Pb method.

Multiple isotopic (Os–Nd–O) analyses were applied on collected samples for understanding their petrogenesis. Re–Os and Sm–Nd elements have different geochemical behaviors during mantle and crustal processes, including magmatic differentiation. Crust and mantle have contrasting Re and Os abundances, and initial Os isotopic compositions, therefore Re–Os compositions of magmas are traceable to the crustal vs. mantle sources (Shirey and Walker, 1998). Consequently, more constraints on petrogenetic processes, such as crustal contamination, can be achieved when their Nd and O isotopic compositions are known. The strength of Sm–Nd method is that it can see back through weak to moderate alteration, high-grade metamorphism, and magmatic differentiation (Dickin, 2005). O isotope compositions are traceable to the magmatic sources and contaminants as well; however, the whole-rock O isotope compositions are susceptible to hydrothermal alteration, which is pervasive in the eastern Gangdese belt because of porphyry-type mineralization. Zircon, as a common high-temperature refractory accessory mineral in igneous rocks, can resist younger thermal events and hydrothermal alterations, and therefore be able to supply reliable and robust estimates of primary magmas (Valley et al., 1994). In addition, the mantle is thought to be homogeneous in O isotope (Eiler, 2001), and igneous zircons in equilibrium with mantle-derived magmas have diagnostic values of 5.3 ± 0.3‰ (Valley et al., 1998).

6. Petrography and mineralogy

Lithological names used below are based on the TAS classification scheme of Le Maitre (1989) and Middlemost (1994), using whole-rock compositions presented in a later section. The following descriptions are based on a combination of new and published samples and observations.

6.1. Paleocene–Eocene suite

Eighteen samples of igneous rocks were collected from Paleocene–Eocene calc-alkaline to high-K calc-alkaline intrusions (twelve samples) and Linzizong volcanic rocks (six samples) in the Gangdese belt.

The Linzizong volcanic rocks include basalt, basaltic trachyandesite, trachyandesite, andesite, dacite, and rhyolite. The basaltic to trachyandesitic and andesitic lavas are composed of clinopyroxene, plagioclase, and minor amphibole phenocrysts, with accessory minerals such as magnetite, rutile, and titanite set in a hyalopilitic groundmass of plagioclase microlites in glass (Fig. 3A). In contrast, the dacites and rhyolites are mainly composed of plagioclase and quartz phenocrysts, set in a glassy or fine-grained quartz-feldspathic groundmass (Fig. 3B).

The intrusive rocks include gabbro, gabbroic diorite, monzodiorite, monzonite, quartz monzonite, granodiorite, and granite. The mafic to intermediate intrusions are composed of coarse-grained orthopyroxene (Fig. 3C), clinopyroxene, plagioclase, and interstitial amphibole, whereas the felsic intrusions are composed plagioclase, K-feldspar, quartz, and minor interstitial biotite (Fig. 3D). The samples collected are mostly fresh, and are representative of the lithologies and spatial distribution of such rocks across the region, as determined by our previous work (Wang et al., 2014a, 2014c) and that of others (e.g., Dong, 2002; Chen, 2006; Dong et al., 2006a, 2006b; Wen, 2007; Mo et al., 2008; Ji et al., 2009; Lee et al., 2009). There are no clear petrographic or mineralogical differences in the Paleocene–Eocene suite either spatially or temporally along the Gangdese belt.

Table 1
Cenozoic igneous rock locations from Gangdese belt, their ages, and applied lithogeochemical and isotopic analyses.

Sample number	Location	Lithology	Longitude (E)	Latitude (N)	Altitude (m)	Sr–Nd isotope	$\delta^{18}O$ isotope	Zircon Hf isotope	Lithogeo-chemistry	Age (Ma)
WR-13-37	Close Gaer	Basalt	80°02′35″	32°23′03″	4391				This study	58
WR-13-40	Close Gaer	Basalt	80°02′35″	32°23′03″	4391	This study				58
WR-13-42	Geji	Andesite	80°14′55″	32°23′54″	4459		Zircon			51
WR-12-40	Gangre	Monzogranite	80°33′28″	31°27′11″	4717					49.3
WR-13-81	Cogen-Saga	Monzonite	85°24′49″	30°07′46″	5500	This study	Zircon		This study	49.9
WR-12-33	Sangsang	Granodiorite	86°19′06″	29°33′17″	5090		Amphibole			50.7
WR-12-30B	Xietongmen	Quartz monzonite	88°19′11″	29°32′54″	4706	This study	Zircon		This study	67.7
WR-13-117	Majiang peak	Trachyandesite	90°07′57″	29°53′53″	5376	This study	Zircon		This study	53
WR-13-118	Majiang peak	Dacite	90°07′57″	29°53′53″	5376				This study	53
WR-13-2	Quxu	Monzonite	90°43′16″	29°21′20″	3500	Chen (2006)	Zircon		Wen (2007)	51.5
WR-12-8	Gurong	Granodiorite	90°43′52″	29°43′52″	3954		Amphibole			56.8
WR-13-109	Gurong	Monzodiorite	90°45′30″	29°48′02″	3789	This study			This study	43.2
WR-13-113A	Gurong	Gabbroic diorite	90°45′30″	29°48′02″	3789	This study			This study	43.2
WR-13-113B	Gurong	Rhyolite	90°45′30″	29°48′02″	3789	This study	Zircon		This study	43.2
WR-12-1	Lhasa	Granodiorite	91°10′59″	29°38′06″	3673					64.3
XG-12-9	Xiongga	Granodiorite	91°36′09″	29°18′34″	3646		Amphibole			50
XG-12-3	Xiongga	Diorite porphyry	91°42′47″	29°16′47″	3661		Amphibole			50
GZ-12-1	Gazhang	Granite	91°53′38″	29°26′27″	4496					60.1
CB-5	Zedang	Quartz monzonite	91°54′51″	29°16′08″	3650		Zircon		Wang et al. (2014b)	29.8
XB-12-1	Xueba	Granite porphyry	92°19′46″	29°24′17″	3954					23.4
XB-12-3	Xueba	Granite porphyry	92°19′46″	29°24′17″	3954			This study	Wang et al. (2014b)	23.4
XB-12-7	Xueba	Diorite	92°18′47″	29°28′34″	4381					23.4
WR-13-36	Gaer	Trachyandesite	80°02′35″	32°23′03″	4391		Zircon	This study		23.19 ± 0.09
WR-13-31	Zhaxigang	Quartz monzonite porphyry	80°11′24″	31°51′13″	4615				This study	20
WR-12-52	Gaer	Trachyandesite	80°19′43″	32°22′36″	4496		Phlogopite		Turner et al. (1996)	16
WR-13-48	Geji	Quartz monzonite porphyry	80°29′50″	32°21′18″	4684	This study	Zircon	This study	This study	23.6 ± 1.9
WR-13-53	Xungba	Trachyandesite	81°52′30″	32°02′36″	4624	This study			This study	21.2
10YR07	Yare	Quartz monzonite porphyry	82°19′48″	31°28′48″	4900		Zircon/Yu et al. (2013)		Unpublished data	16
WR-13-26	Mayum	Granodiorite porphyry	82°26′33″	30°36′10″	5169	This study			This study	18.4
WR-13-74	Cogen	Granodiorite porphyry	85°05′03″	30°49′54″	4722		Zircon	This study		15.56 ± 0.22
WR-13-83	Jiadacuo	Trachydacite	85°46′00″	29°50′10″	5180	Williams (2000)	Zircon	This study	This study	17.68 ± 0.37
WR-13-85	Jiadacuo	Trachyandesite	85°46′00″	29°50′10″	5180	Williams (2000)			This study	17.68
WR-13-18	Sangsang	Trachyandesite	87°01′03″	29°19′15″	4502	This study			Williams (2000)	13
JR-5	Jiru	Monzonite porphyry/volcanic rocks	88°53′16″	29°39′24″	4697	This study	Zircon	This study	Wang et al. (2014b)	16
WR-13-14	Suojin	Trachydacite	89°35′04″	29°40′56″	4336	Williams (2000)	Zircon	This study	Williams (2000)	12.26 ± 0.25
WR-13-122	Yangying	Trachyandesite	90°22′38″	29°43′12″	4615	This study	Zircon	This study	This study	10.48 ± 0.15
WR-13-100	Qulong	Monzonite porphyry/Volcanic rocks	91°36′51″	29°36′30″	5184	This study	Zircon	This study	Yang (2008)	14
QL02-04-2	Qulong	Granodiorite porphyry	91°36′51″	29°36′30″	5184	Yang (2008)	Amphibole		Yang (2008)	19
QL02-07	Qulong	Granodiorite porphyry	91°36′51″	29°36′30″	5184	Yang (2008)	Amphibole		Yang (2008)	19
JM11-34	Jiama	Quartz monzonite porphyry	91°45′13″	29°41′43″	4650		Zircon		Hou et al. (2004)	15

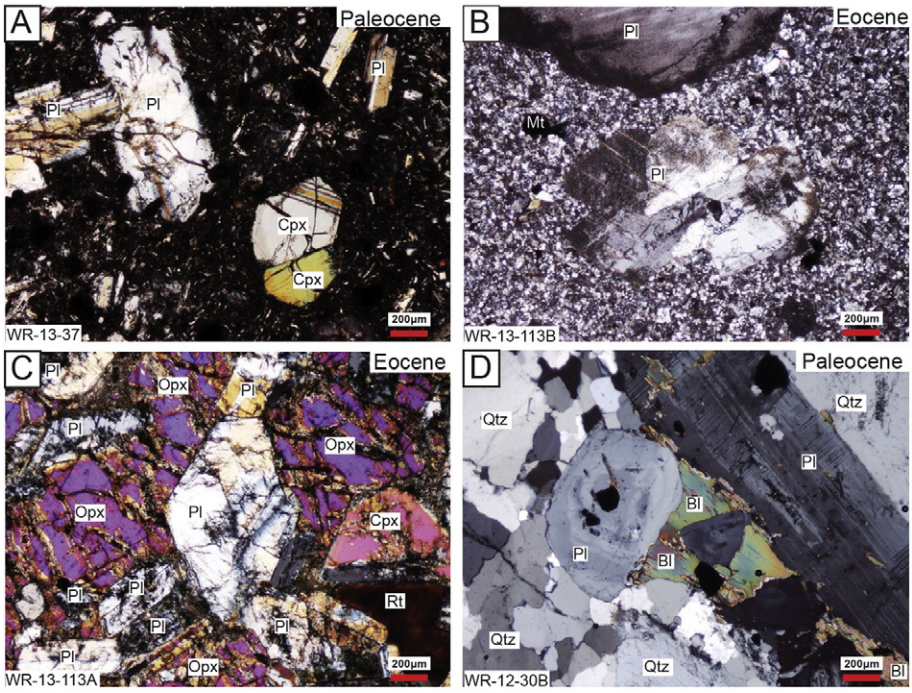

Fig. 3. Photomicrographs showing: A. Paleocene basalt (sample WR-13-37) with plagioclase and clinopyroxene; cross-polarized light; B. Eocene rhyolite (WR-13-113B) with plagioclase phenocrysts; cross-polarized light; C. Eocene gabbroic diorite (WR-13-113A) with orthopyroxene and plagioclase; cross-polarized light; D. Paleocene quartz monzonite (WR-12-30B) with biotite, plagioclase, and K-feldspar; cross-polarized light. Abbreviations: Bi = biotite; Cpx = clinopyroxene; Kfs = K-feldspar; Mt = magnetite; Opx = orthopyroxene; Phl = phlogopite; Pl = plagioclase; Rt = rutile.

6.2. Oligocene suite in the eastern Gangdese belt

Oligocene igneous rocks are sparse in the Gangdese belt, and all known occurrences are located in the eastern part of the belt (e.g., Harrison et al., 2000; Zheng et al., 2012; Wang et al., 2014b). The main lithologies observed are monzonite, quartz monzonite, and granite porphyry, with minor diorite. The diorites are mainly composed of equigranular coarse-grained amphibole and plagioclase, whereas the quartz monzonite and granite porphyry are mainly composed of amphibole, plagioclase, biotite, quartz, and K-feldspar phenocrysts set in a phaneritic matrix of quartz, plagioclase, and biotite.

6.3. Miocene suite in the eastern Gangdese belt

Miocene igneous rocks in the eastern Gangdese belt occur as shallowly-emplaced calc-alkaline to high-K calc-alkaline granitoid plutons, and minor high-K calc-alkaline to shoshonitic volcanic rocks, that intrude or cover earlier Cretaceous–Eocene intrusive and volcanic rocks (Fig. 2).

The collected alkaline volcanic rocks include one trachyandesite, one trachydacite, and two porphyritic trachyandesite dike samples (JR-5 and WR-13-100, Table 1). Trachyandesite and trachydacite lavas consist of clinopyroxene, amphibole, plagioclase, phlogopite, sanidine, and K-feldspar phenocrysts set in a fine-grained, trachytic groundmass (Fig. 4A, B). The porphyritic trachyandesite dike samples have a hyalopilitic texture, and are composed of amphibole and minor plagioclase phenocrysts set in a fine-grained amphibole-feldspathic groundmass (Fig. 4C).

Two samples of granodiorite porphyry (Fig. 4D), one sample of quartz monzonite porphyry, and one sample of granite were collected from intrusions associated with the Qulong, Jiama, and Bangpu porphyry deposits (Table 1), and are common rock types in this part of the belt (e.g., Hou et al., 2004; Yang et al., 2009; Li et al., 2011; Wang et al., 2014a). The quartz monzonite porphyry and granodiorite porphyry samples consist of plagioclase, K-feldspar, amphibole, and quartz phenocrysts set in a phaneritic matrix of quartz, plagioclase, and biotite. The granite sample consists of amphibole, plagioclase, K-feldspar, biotite, and quartz with an equigranular texture. All samples were collected well away from the actual porphyry deposits to minimize the effects of hydrothermal alteration.

6.4. Miocene suite in the western Gangdese belt

Miocene igneous rocks collected from the western Gangdese belt consist of six high-K calc-alkaline to shoshonitic volcanic rocks (lava flows and pyroclastic deposits), and five high-K calc-alkaline to shoshonitic porphyritic granitoids. The alkaline volcanic rocks are trachyandesitic and trachydacitic, and are mainly composed of phlogopite, sanidine, and amphibole phenocrysts set in an aphanitic or hyalopilitic matrix (Fig. 4E, F). These samples are representative of the lithologies and spatial distribution of such rocks as described in the literature (e.g., Miller et al., 1999; Ding et al., 2003; Williams et al., 2004; Zhao et al., 2009; Guo et al., 2013).

Three samples of quartz monzonite porphyry and two samples of granodiorite porphyry were collected, and consist of amphibole, plagioclase, sanidine, biotite, phlogopite, and quartz phenocrysts set in a fine-grained matrix (Fig. 4G, H). These porphyritic granitoids are mineralogically and geochemically similar to the alkaline volcanic rocks, and therefore are equivalents of the alkaline volcanic rocks.

7. Analytical techniques

7.1. Lithogeochemical analysis

Fresh samples of igneous rock for lithogeochemical analysis were prepared by crushing (using corundum plates) and grinding in an agate disk mill at the Hebei Geological Survey Laboratory, China. The expected contamination of Si and Al by these methods from agate disk mill is estimated to be less than one weight percent (as assessed from

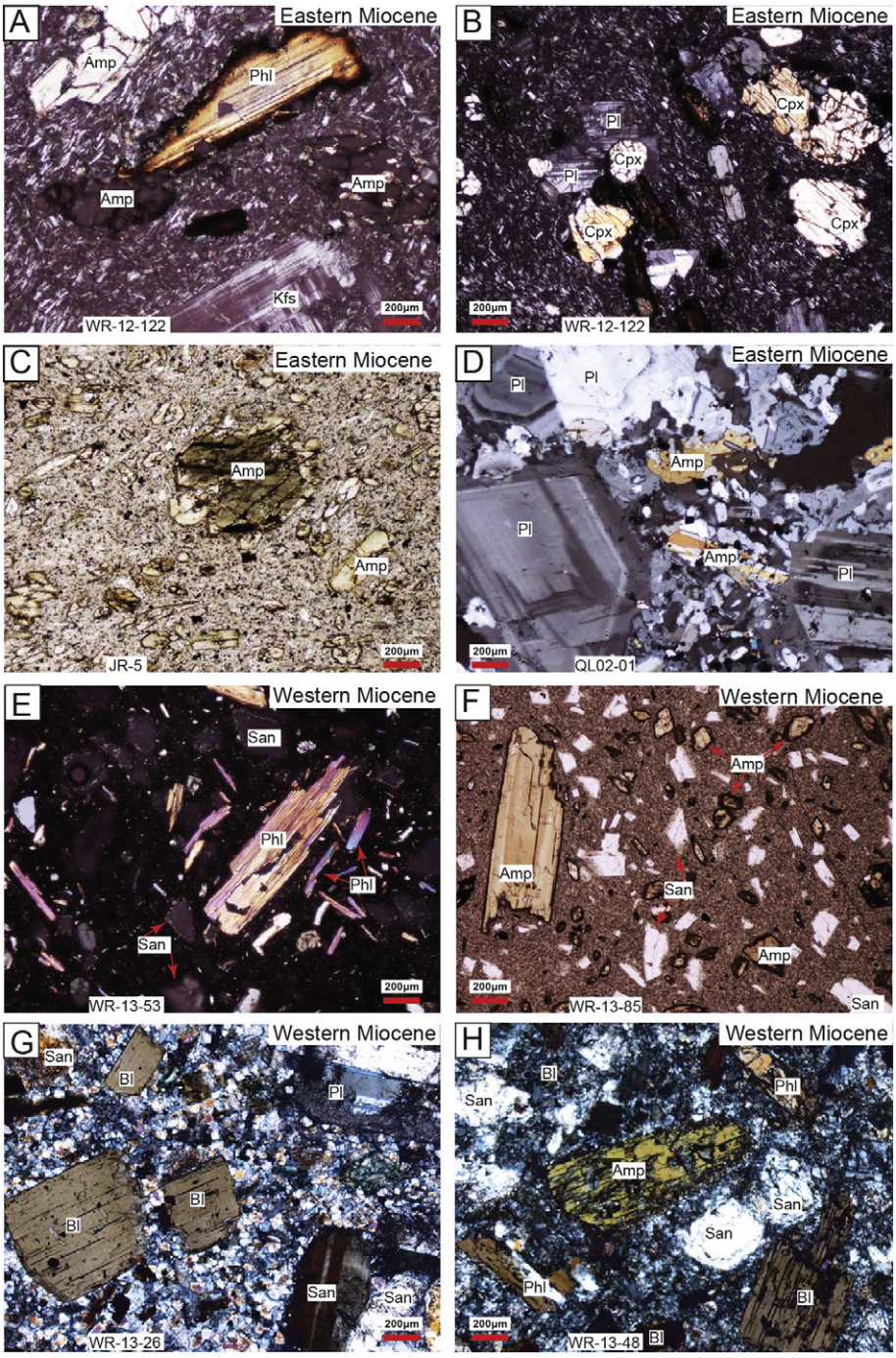

Fig. 4. Miocene igneous rocks from the eastern (A–D) and western (E–F) Gangdese belts. Photomicrographs showing: A and B. trachyandesite (WR-13-122) with phlogopite, K-feldspar, and amphibole, and clinopyroxene phenocrysts (cross-polarized light); C. porphyritic trachyandesitic dyke (JR-5) with amphibole phenocrysts (plane-polarized light); D. quartz monzonite porphyry (QL02-01) with amphibole and plagioclase (cross-polarized light); E and F. trachyandesite (WR-13-53 and WR-13-85), G. granodiorite porphyry (WR-13-26), and H. quartz monzonite porphyry (WR-13-48) with phlogopite, biotite, sanidine, and amphibole phenocrysts. (E, G, H): cross-polarized light; (F): plane-polarized light; Abbreviations: Amp = amphibole; Bi = biotite; Cpx = clinopyroxene; Kfs = K-feldspar; Phl = phlogopite; Pl = plagioclase; San = sanidine.

analyses of standards and blanks). All samples were analyzed at the National Research Center of Geoanalysis, Chinese Academy of Geological Science, in Beijing. Major elements were analyzed by wavelength dispersive X-ray fluorescence spectrometry. Accuracy for major elements, as determined by reproducibility of standards and duplicates, is typically within five relative percent (<2 relative % for SiO_2 and Al_2O_3). Trace elements were analyzed with a Finnigan MAT inductively coupled plasma mass spectrometer (ICP-MS, Thermo Scientific X Series 2). Analytical accuracy for most trace elements is better than five relative percent. The detailed analytical methods and precision for most elements have been described by Yang et al. (2015).

7.2. Nd–Sr isotope analyses

Finely ground sample powders (prepared as above) of seven igneous rocks from the Paleocene–Eocene suite, and eight igneous rocks from the Miocene suite were processed and analyzed for Nd–Sr isotopes at the Radiogenic Isotope Facility, University of Alberta.

Rock powders were accurately weighed and spiked with a known amount of mixed ^{150}Nd–^{149}Sm tracer solution, which has been calibrated directly against the Caltech mixed Sm/Nd normal spike described by Wasserburg et al. (1981). Dissolution used 3 mL mixed 24 mol/L HF + 16 mol/L HNO_3 media in sealed PFA Teflon vessels, held at 160 °C for 5 days, followed by 3 mL 6 mol/L HCl. Chemical processing blanks are <500 pg for Sm and Nd, and are insignificant relative to the amounts of Sm or Nd in the samples. Further details can be found in Creaser et al. (1997) and Unterschutz et al. (2002). The isotopic compositions of Sm and Nd were determined in static mode by multi-collector ICP-mass spectrometry, and detailed procedures are described in Schmidberger et al. (2007). The Geological Survey of Japan Nd isotope standard "Shin Etsu: J-Ndi-1" (Tanaka et al., 2000) was used to monitor Nd isotopic measurements. The long-term average value for this standard obtained in the Radiogenic Isotope Facility is 0.512098 ± 11 [1δ, n = 66, past 6 years], compared to the recommended value of 0.512107 ± 7 when normalized to $^{146}Nd/^{144}Nd = 0.7219$. This represents an accuracy of ±0.17 epsilon units.

Rb/Sr analyses were performed using isotope dilution and thermal ionization mass spectrometry (TIMS) using methods described in detail by Creaser et al. (2004). Accurately weighed sample powders were dissolved in HF/HNO_3 as above, together with a known quantity of a mixed ^{87}Rb–^{84}Sr tracer, and Sr and Rb were separated by conventional cation exchange chromatography. The isotopic composition of Rb and Sr was measured using a Micromass Sector 54 instrument using single-filament analysis methods and static Faraday cup detection. The average value of the NIST SRM987 Sr isotope standard measured during the course of the analyses was 0.710279 ± 28 (1δ, n = 28), and all Sr isotope data presented here are adjusted to a value for SRM987 of 0.71025.

7.3. Amphibole and phlogopite O isotope analysis

Crystals of amphibole and phlogopite from fresh igneous rocks were hand separated after coarse crushing, and were then reacted with BrF_5 at 625 °C to liberate oxygen (Clayton and Mayeda, 1963). Oxygen was then converted to CO_2 and analyzed for oxygen isotopic ratios on a Finnigan-MAT 252 mass spectrometer in the Stable Isotope Laboratory, University of Alberta. The data are reported in the usual delta notation with respect to Vienna Standard Mean Ocean Water (VSMOW). Analytical reproducibility for $\delta^{18}O$ values was ±0.1‰ (2σ).

7.4. Os isotope analyses

Chemistry and mass spectrometric analyses were performed at the National Research Center of Geoanalysis, Chinese Academy of Geological Science, in Beijing. Four grams of thirty-three finely ground igneous rock powders was spiked with a known amount of mixed ^{185}Re–^{190}Os tracer solution (Du et al., 2004), and put into a clean, dry, chilled Pyrex® borosilicate glass Carius tube. 3 mL of purified 12 mol/L HCl, 5 mL of purified 15 mol/L HNO_3, and 1 mL H_2O_2 (30%) were added to the tube, and then the tube was sealed. The digestions were performed at about 230 °C for 24–48 h in an oven. An improved distillation technique was used for the separation of Os, and solvent extraction was used to extract Re (Zhou, 2012; Zhou et al., 2012).

The purified Re and Os were loaded onto platinum filaments, and analyzed by a Thermo Fisher Scientific Triton-plus TIMS (Creaser et al., 1991; Völkening et al., 1991). Re isotope ratios were measured as $^{185}ReO_4^-$ and $^{187}ReO_4^-$ using static-mode Faraday cups. Osmium isotope ratios were measured as $^{186}OsO_3^-$, $^{187}OsO_3^-$, $^{188}OsO_3^-$, $^{189}OsO_3^-$, $^{190}OsO_3^-$, and $^{192}OsO_3^-$ using multi-Faraday cups. Measured Re and Os ratios were corrected for mass fractionation using $^{185}Re/^{187}Re = 0.59738$ (Gramlich et al., 1973) and for spike and blank contributions using $^{192}Os/^{188}Os = 3.0827$ (Luck and Allègre, 1983). Total procedural blanks for Re and Os are 1.39 and 0.3 pg/g, respectively. The reference value for applied Chinese First Class Standard GBW04477 (JCBY sulfide, Certificate No. 1325) has Re of 38.61 ± 0.54 (ng/g), Os of 16.23 ± 0.17 (ng/g), and $^{187}Os/^{188}Os$ ratio of 0.3363 ± 0.0029. The reproducibility of standard sample during analysis is 38.13 ± 0.11 (ng/g) for Re, 16.11 ± 0.05 (ng/g) for Os, and 0.3354 ± 0.0017 for $^{187}Os/^{188}Os$ ratio. Blank correction has been applied on analyzed samples.

7.5. Zircon U–Pb dating with SIMS

Zircons were separated from 2–3 kg of crushed rock samples by heavy-liquid and magnetic methods followed by hand-picking at the Hebei Geological Survey Laboratory, China. Selected crystals were typical of magmatic zircons: euhedral, clear, colorless, devoid of mineral and fluid inclusions, and 50–150 μm in diameter. The zircons were mounted in epoxy and polished to reveal their interiors. Cathodoluminescence (CL, Fig. A1–A6), backscattered electron (BSE), and secondary electron (SE) images were obtained for the zircon grain mounts prior to analysis, to reveal internal zonations.

One epoxy grain mount was prepared containing three unknown zircon groups and reference zircons TEM2 (416.8 Ma; Black et al., 2004) and 6266 (559.0 Ma; Stern and Amelin, 2003). Secondary ion mass spectrometer (SIMS, Cameca IMS 1280) analyses of U–Pb isotopes were carried out in one session (I14022, divided into 3 sub-sessions for data processing) in March 2014. The primary beam characteristics included $^{16}O_2^-$ (3–6 nA); impact energy = 23 keV; and projected (Kohler) image mode, with 15 μm × 25 μm probe dimensions. The primary beam was rastered around the analysis site for 2 min prior to data collection with a stationary primary beam. IMS1280 secondary ion extraction conditions included a sample image magnification of 200× at the field aperture, entrance slit width = 65 μm, and field aperture width = 8 mm. The energy slit was maintained full open. Positive secondary ions were collected sequentially with the axial electron multiplier and an exit slit width = 185 μm, giving a mass resolution (1% peak height definition) 4500–4900. Ten secondary ion mass positions (typical count times in seconds) were collected over 5 cycles: $^{196}Zr_2O^+$ (2), $^{204}Pb^+$ (20), $^{204.05}background^+$ (20), $^{206}Pb^+$ (20), $^{207}Pb^+$ (30), $^{208}Pb^+$ (3), $^{238}U^+$ (3), $^{248}ThO^+$ (3), $^{254}UO^+$ (3), and $^{270}UO_2^+$ (5). Data were processed using SQUID2 software (Ludwig, 2009), in a custom version designed for processing data output from the IMS 1280. Weighted mean and age calculations were carried out using Isoplot v. 3.76 (Ludwig, 2012). Uranium decay constants are those of Jaffey et al. (1971). The $^{206}Pb/^{238}U$ ages were calibrated against TEM2 zircon, using a calibration constant ('a') determined from the relationship $^{206}Pb^+/^{270}UO_2^+ = a \cdot (^{270}UO_2^+/^{254}UO^+)^m$, where the *m* ranged from 0.84 to 0.90 for TEM2 data. Spot-to-spot excess uncertainties in the $^{206}Pb/^{238}U$ values (not accounted for by within-spot counting uncertainties) determined from analyses of TEM2 ranged from ±0.6% to 0.8% (68% confidence) (Stern and Ickert, 2010). Uranium abundances were calibrated against 6266 zircon with U = 903 ppm, utilizing $^{270}UO_2^+/^{196}Zr_2O^+$. The Th/U ratios and Th abundances were determined from $^{248}ThO^+/^{254}UO^+$ using measured $^{232}Th/^{238}U$ discrimination factors for the session (~1.0). The radiogenic Pb-isotopes were corrected for common Pb using ^{204}Pb, assuming a model crustal composition (Stacey and Kramers, 1975) at the $^{206}Pb/^{238}U$ age of the sample. All count rates were corrected for deadtime = 40 ns. The mean $^{206}Pb/^{238}U$ age determined for 6266 zircon (N = 61) analyzed concurrently is 560 ± 1.5 (MSWD = 2.4), a value that is within error of the reference age of 559 Ma. The corresponding mean $^{207}Pb/^{206}Pb$ age is 562.9 ± 2.7 Ma (MSWD = 0.86).

7.6. Zircon O isotope analysis with SIMS

Oxygen isotope analyses were carried out by SIMS (Cameca 1280) at the Canadian Centre for Isotopic Microanalysis (CCIM), University of Alberta. Pristine zircon core and rim domains (based on CL/BSE/SE images) were targeted for analysis using a 20 keV Cs^+ ion beam with

a spot size of ~15 μm diameter. Reported errors are a quadratic combination of the standard error of the analysis and the standard deviation of the reference materials analyzed together with the unknowns, and the uncertainties per analysis are typically ±0.2‰ (2σ). The primary reference material utilized in this study was the CCIM internal zircon S0081 with $\delta^{18}O_{VSMOW} = +4.87‰$. The accuracy of analyses for this study was evaluated from concurrent analyses of secondary reference zircon TEM2 with $\delta^{18}O_{VSMOW} = +8.20‰$ (Black et al., 2004). The mean of 94 analyses was $\delta^{18}O_{VSMOW} = +8.27‰$ ($1\sigma = 0.13‰$).

7.7. Zircon Hf isotope analyses

Hf isotopic compositions of zircons were analyzed using a Nu Plasma high-resolution (HR) MC–ICP-MS (Nu Instruments) coupled with Geolas 2005 LA system equipped with a 193 nm ArF-excimer laser at the State Key Laboratory of Continental Dynamics, Northwest University, Xi'an, China. The analytical spot size is around 44 μm, and the repetition rate is 10 Hz. The detailed descriptions of analytical procedures can be found in Wu et al. (2006) and Yuan et al. (2008), and Zircon 91500,

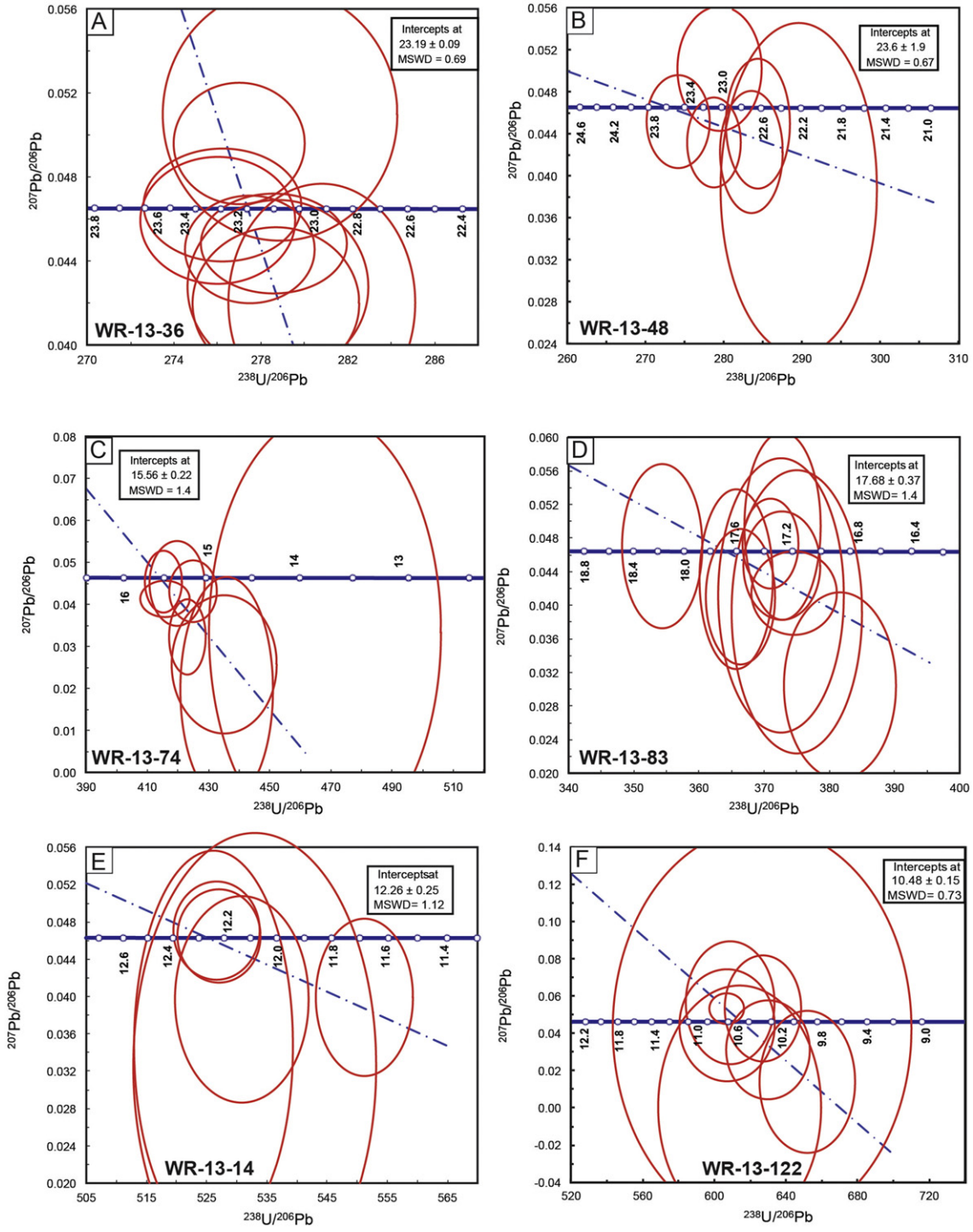

Fig. 5. Zircon U–Pb reverse concordia diagrams for intrusive and volcanic samples dated by SIMS. A. Sample WR-13-36; B. Samples WR-13-48; WR-13-74; WR-13-83; WR-13-14; and WR-13-122.

MON and GJ-1 were used as the secondary standards for data quality assessment, with recommended $^{176}Hf/^{177}Hf$ ratios of 0.282307, 0.282739 and 0.282015, respectively. Model ages of the samples were calculated with an assumption that the $^{176}Lu/^{177}Hf$ ratio of average crust is 0.015, and the $^{176}Hf/^{177}Hf$ and $^{176}Lu/^{177}Hf$ ratios of present chondrite and depleted mantle are 0.282772 and 0.0332, 0.28325 and 0.0384, respectively (Blichert-Toft and Albarède, 1997; Griffin et al., 2002; Vervoort and Patchett, 1996). The decay constant of ^{176}Lu used for this study is 1.865×10^{-11} (Scherer et al., 2001).

8. Zircon U–Pb dating results

Six intrusive and volcanic rocks from the Miocene Gangdese belt were selected for zircon U–Pb dating. Four of them are undated, and two of them were previously dated with Ar–Ar method. The dating results are reported in Table A1.

Sample WR-13-36 was collected from the trachyandesitic lava near Gaer town. This sample contains a homogeneous population of zircons, and which yielded a concordia intercept age of 23.19 ± 0.09 Ma (MSWD = 0.69; Fig. 5A). This date is interpreted to be the emplacement age of this rock.

Sample WR-13-48 was collected from a quartz monzonite porphyritic intrusion near Geji town. It contains a homogeneous population of zircons, and which yielded an intercept age of 23.6 ± 1.9 Ma (MSWD = 0.67; Fig. 5B). This date is interpreted to be the crystallization age of this rock.

Sample WR-13-74 was collected from a granodioritic intrusion near Cogen town. It contains a homogeneous population of zircons, and which yielded an intercept age of 15.56 ± 0.22 Ma (MSWD = 1.4; Fig. 5C). This date is interpreted to be the crystallization age of this rock.

Sample WR-13-83 was collected from the trachydacitic lava near Jiadacuo Lake. The previous Ar–Ar dating results on whole rock and hornblende suggest that the formation of the lavas at 17.3–19.3 Ma (Williams, 2000). The collected sample contains a homogeneous population of zircons, and which yielded an intercept age of 17.68 ± 0.37 Ma (MSWD = 1.4; Fig. 5D). This date is consistent with previous dating results, and interpreted to be the emplacement age of this rock.

Sample WR-13-14 was collected from the trachydacitic lava near Suojin town. The collected sample contains a homogeneous population of zircons, and which yielded an intercept age of 12.26 ± 0.25 Ma (MSWD = 1.12; Fig. 5E). This date is interpreted to be the emplacement age of this rock.

Sample WR-13-122 was collected from the trachyandesitic lava near Yangying town. The previous Ar–Ar dating results on sanidine and biotite suggest that the formation of the lavas at 10.73–11.40 Ma (Zhou et al., 2004). The collected sample contains a homogeneous population of zircons, and which yielded an intercept age of 10.48 ± 0.15 Ma (MSWD = 0.73; Fig. 5F). This date is consistent with previous dating results, and interpreted to be the emplacement age of this rock.

9. Geochemical and isotopic results and petrogenesis

Whole-rock geochemical data, Sr–Nd–Os isotope data, and mineral (amphibole, phlogopite, and zircon) O, and zircon Hf isotope data from this study are listed in Tables 2–6, and Table A2. These data are supplemented with data from the literature as reviewed in (Wang et al., 2014a, 2014b, 2014c, 2015) in the following discussions.

Whole-rock geochemical data are plotted on lithological discrimination diagrams in Fig. 6, and normalized trace element diagrams in Fig. 7. Mineral oxygen isotopic compositions are plotted in Fig. 8, whole-rock Sr–Nd–Os isotopic compositions are plotted in Figs. 9 and 10, and zircon hafnium isotopic compositions are plotted in Fig. 11,

9.1. Paleocene–Eocene magmatism

Cospatial and coeval Paleocene–Eocene intrusive and volcanic rocks show a similar compositional range. Five samples of Paleocene–Eocene intrusions have gabbroic, dioritic, monzodioritic, monzonitic, and quartz monzonitic compositions, whereas four samples of Linzizong volcanic rocks are basaltic, trachyandesitic, dacitic, and rhyolitic (Fig. 6A). They are mostly subalkalic and plotted in the calc-alkaline to high-K calc-alkaline fields (Fig. 6A, B). Data for other Paleocene–Eocene igneous rocks from the literature show similar but much broader ranges of compositions.

All samples have low Sr/Y and $[La/Yb]_N$ ratios (Fig. 6C, D), and show weakly listric normalized rare earth element (REE) patterns with moderate enrichments of light rare earth elements (LREE) relative to middle and heavy rare earth elements (MREE and HREE) ($[La/Yb]_N = 8.7 \pm 3.3$, range = 3.7–14.2; Figs. 6D, 7A). They mostly have distinct negative Eu anomalies, indicating fractionation of plagioclase feldspar from relatively dry melts (Wang et al., 2014a). On a primitive mantle-normalized trace element diagram these samples show relative depletions in Nb, Ta, P, and Ti, and enrichments in Th, U, Pb, and K (Fig. 6B), typical of arc-related igneous rocks worldwide (Pearce, 1982; Perfit et al., 1984; Arculus and Powell, 1986). Our data fall within the typical ranges of Paleocene–Eocene igneous rocks from the literature, shown as gray fields in Figs. 6 and 7.

Zircon $\delta^{18}O$ values from these rocks show a small range from +5.1‰ to +6.4‰ (Fig. 8A). Two mafic samples with low zircon $\delta^{18}O$ values plot in the mantle range (+5.3 ± 0.3‰: Valley et al., 1998), and four intermediate–felsic samples have $\delta^{18}O$ values between +5.6‰ and +6.4‰ (Fig. 8A). These values are similar to values for amphibole, which range from +5.3‰ to +6.7‰ (Fig. 8B). These values are close to the range expected for minerals in equilibrium with mantle-derived magmas, and indicate only minor crustal contamination (Kyser, 1986; Mattey et al., 1994a, 1994b; Chazot et al., 1997; Eiler, 2001).

The $(^{87}Sr/^{86}Sr)_i$, εNd_i, and $(^{187}Os/^{188}Os)_i$ values for these samples range from 0.7046 to 0.7079 (Fig. 9C), from −4.3 to +6.3 (Fig. 9A, B), and from 0.226 to 0.464 (Fig. 10), respectively. Our new Sr–Nd isotopic data mostly overlap the ranges of Paleocene–Eocene igneous rocks from the literature (Fig. 9A–C). In addition, Cretaceous Gangdese arc rocks have $(^{87}Sr/^{86}Sr)_i$ compositions ranging from 0.7032 to 0.7048, and εNd_i values from +0.2 to +5.3 (Wen, 2007; Zheng et al., 2014a) and that in combination with our new $(^{187}Os/^{188}Os)_i$ values suggest that these magmas were derived from the mantle in response to Neo-Tethyan subduction, with variable amounts of crustal contamination.

In order to assess the effect of crustal contamination, we have used the Energy-Constrained-Assimilation and Fractional Crystallization (EC-AFC) model of Bohrson and Spera (2001) and Spera and Bohrson (2001) to simulate interaction between the most isotopically primitive basalt (WR-13-40, western Gangdese) and gabbro (AG0364-2, eastern Gangdese) and possible crustal contaminants (Fig. 12A). The crustal contaminants are average upper and lower crusts (Bohrson and Spera, 2001). The reason for using different starting primitive magma candidates for eastern Gangdese group and western Gangdese group is that, generally, Paleocene–Eocene igneous rocks in the eastern Gangdese belt have lower $(^{87}Sr/^{86}Sr)_i$ ratios and higher compositions εNd_i values than the counterparts in the western Gangdese belt (Figs. 10A, and 12A). We think the geochemical heterogeneity of Tibetan lithosphere from the west to the east might exist. The simulations indicate that upper crustal contaminations (within 10%) could explain the trend of Sr–Nd isotopic data of the Paleocene–Eocene igneous rocks (Fig. 12A). εNd_i vs. SiO_2 plots for Paleocene–Eocene igneous rocks verify this crustal contamination, because the more evolved magmas have lower εNd_i values (Fig. 12C, D). This crustal contamination trend is also shown on Os isotopic system (Fig. 10C, D), where the felsic samples have higher $(^{187}Os/^{188}Os)_i$ ratios than the mafic ones.

Table 2
Major and trace element analysis of igneous rock samples from the Cenozoic Gangdese magmatic belt.

Sample	WR-13-37	WR-13-81	WR-12-30B	WR-13-117	WR-13-118	WR-13-109	WR-13-113A	WR-13-113B	WR-13-53	WR-13-31	WR-13-26	WR-13-48	WR-13-84	WR-13-85	WR-13-122
wt. n															
SiO_2	49.18	57.84	66.01	62.37	64.12	54.33	54.76	74.22	59.39	65.28	66.72	65.58	64.10	62.76	60.42
TiO_2	0.77	1.08	0.57	0.75	0.79	1.14	1.05	0.18	1.22	0.62	0.59	0.82	0.67	0.75	0.78
Al_2O_3	19.13	16.55	15.54	14.86	15.06	17.29	17.90	13.74	12.48	15.89	15.35	14.86	16.22	16.45	15.19
TFe_2O_3	7.84	7.12	4.58	5.56	6.04	11.22	8.80	2.04	4.46	3.71	3.63	3.36	4.06	4.09	5.07
MnO	0.10	0.16	0.10	0.10	0.08	0.32	0.25	0.05	0.08	0.06	0.05	0.06	0.06	0.06	0.13
MgO	3.04	2.95	1.60	1.73	1.73	3.09	3.10	0.27	4.63	1.46	1.82	2.20	2.19	2.24	2.58
CaO	11.08	5.06	3.57	3.25	2.19	3.49	6.04	0.93	4.63	2.62	3.25	2.67	4.41	4.47	4.13
Na_2O	2.70	3.33	3.81	3.71	4.39	5.42	4.14	4.70	1.04	3.77	3.83	3.30	4.14	4.10	3.67
K_2O	0.28	4.81	3.69	3.35	2.63	0.98	1.27	3.95	7.92	5.20	3.41	6.24	3.14	3.06	5.54
P_2O_5	0.14	0.38	0.15	0.22	0.22	0.32	0.44	0.03	1.09	0.24	0.21	0.43	0.22	0.24	0.61
LOI	6.38	0.64	0.30	4.00	3.13	3.10	1.79	0.57	2.07	1.54	1.52	0.78	0.29	1.69	1.43
Total	100.62	99.92	99.91	99.89	100.38	100.70	99.54	100.68	99.00	100.39	100.38	100.67	99.50	99.89	99.55
ppm															
Sc	22.3	14.5	13.4	13.6	16.1	18.6	14	8.3	18.3	9.2	9.0	8.5	7.4	10.2	13.5
V	203.8	157	79.7	73.4	85.1	170	151	5.6	123	70.0	77.6	67.2	75.4	83.7	124
Cr	17.9	28.1	7.2	5.8	8.7	bdl	11.8	4.6	529	8.6	22.8	48.9	518	30.2	66.2
Co	30.8	18.3	10.4	8.9	9.7	11.8	14.9	1.4	20.2	9.4	11.8	9.6	20.9	13.1	20.5
Ni	19.1	18.8	5.5	3.6	5.0	9	10	0.5	112.7	8.7	15.2	31.4	167.4	20.2	41.7
Rb	4.80	213.7	142.0	99.6	79.5	66	88	109	786	242	133	445	121	100	392
Ba	76.8	661	525	818	514	148	311	915	3102	1426	889	2148	752	705	4000
Th	2.00	31.86	17.49	19.82	19.29	4.03	3.55	14.27	206	64.09	12.64	109.0	14.62	9.61	102.3
U	0.47	4.00	2.78	4.22	4.19	2.73	2.56	3.12	25.18	8.68	3.89	14.07	2.87	2.18	14.27
Nb	1.31	14.26	8.43	7.64	7.70	7.7	4.1	7.02	26.81	17.45	7.54	21.06	6.43	4.76	20.17
Ta	0.13	1.29	0.88	0.81	0.79	0.37	0.3	0.78	1.94	2.39	0.99	1.70	0.57	0.41	1.43
La	7.97	61.77	28.77	34.67	38.99	23.9	20.8	31.91	80.70	78.55	33.89	91.08	33.50	28.68	158
Ce	17.14	122.4	52.30	67.08	65.23	50.9	42.1	59.53	204.5	135	63.28	188	58.72	52.49	310
Pb	5.66	14.57	22.49	5.53	5.71	19	19	21.51	63.38	51.86	30.62	104	30.03	25.78	126
Pr	2.54	14.84	6.44	8.46	8.92	6.64	5.36	7.36	31.47	15.05	7.99	23.55	7.74	6.57	35.85
Sr	414	679	316	156	127	180	480	79.5	590	713	691	858	826	868	1529
Nd	11.39	55.41	23.30	32.50	34.57	27.4	22.3	27.23	150.3	50.06	30.68	92.68	29.65	25.23	132.5
Sm	2.88	10.32	4.45	6.38	6.71	6.05	4.63	5.47	33.05	6.90	5.36	15.24	5.21	4.19	20.9
Zr	47.93	332	194	269	266	310	305	215	514	246	139	460	116	140	565
Hf	1.66	9.33	6.04	7.78	7.45	6.1	6.1	6.59	15.72	8.19	4.30	13.51	3.72	4.28	15.12
Eu	0.92	1.85	1.01	1.37	1.47	1.63	1.65	1.13	4.96	1.29	1.23	2.71	1.20	1.12	4.00
Gd	2.90	7.97	4.24	6.00	6.48	5.72	3.89	4.95	17.37	4.19	4.06	8.03	3.69	3.24	12.53
Tb	0.43	1.08	0.63	0.87	0.95	0.92	0.59	0.73	1.61	0.44	0.49	0.84	0.42	0.36	1.31
Dy	2.69	6.05	3.71	5.41	5.54	5.31	3.31	4.41	7.07	2.07	2.53	3.61	2.17	1.70	5.68
Y	13.37	27.28	18.81	26.94	28.77	30	17	22.51	27.26	8.74	11.44	13.66	9.28	6.93	22.56
Ho	0.54	1.10	0.75	1.09	1.10	1.07	0.66	0.88	1.11	0.34	0.46	0.55	0.36	0.28	0.91
Er	1.54	3.14	2.20	3.00	3.14	3.04	1.92	2.60	3.33	1.11	1.24	1.62	0.99	0.78	2.66
Tm	0.24	0.45	0.33	0.46	0.48	0.447	0.277	0.41	0.36	0.13	0.17	0.18	0.13	0.10	0.28
Yb	1.57	3.11	2.35	3.01	3.12	3.04	1.81	2.69	2.54	0.85	1.12	1.11	0.83	0.65	2.01
Lu	0.24	0.45	0.36	0.48	0.47	0.502	0.295	0.43	0.35	0.14	0.17	0.15	0.13	0.09	0.28

Table 3
Zircon O isotope data for the Cenozoic Gangdese magmatic rocks.

Sample	Spot name	$^{18}O/^{16}O$	$\delta^{18}O_{(VSMOW)}$ (‰)	2σ (‰)
WR-13-42	S2811_1@1	0.00201555	5.16	0.22
WR-13-42	S2811_11@1	0.00201547	5.12	0.18
WR-13-42	S2811_15@1	0.00201553	5.15	0.19
WR-13-42	S2811_20@1	0.00201552	5.15	0.19
WR-13-42	S2811_26@1	0.00201584	5.31	0.20
WR-13-42	S2811_26@2	0.00201579	5.28	0.18
WR-13-42	S2811_3@1	0.00201561	5.19	0.19
WR-13-42	S2811_7@1	0.00201547	5.12	0.19
WR-13-81	S2791_1@1	0.00201775	6.26	0.29
WR-13-81	S2791_11@1	0.00201735	6.06	0.26
WR-13-81	S2791_12@1	0.00201663	5.70	0.29
WR-13-81	S2791_12@2	0.00201705	5.91	0.26
WR-13-81	S2791_13@1	0.00201721	5.99	0.26
WR-13-81	S2791_14@1	0.00201742	6.09	0.25
WR-13-81	S2791_15@1	0.00201719	5.98	0.25
WR-13-81	S2791_16@1	0.00201745	6.11	0.24
WR-13-81	S2791_18@1	0.00201760	6.18	0.26
WR-13-81	S2791_19@1	0.00201727	6.02	0.22
WR-13-81	S2791_20@1	0.00201736	6.07	0.25
WR-13-81	S2791_21@1	0.00201764	6.21	0.26
WR-13-81	S2791_4@1	0.00201727	6.02	0.22
WR-13-81	S2791_5@1	0.00201720	5.98	0.24
WR-13-81	S2791_6@1	0.00201731	6.04	0.25
WR-13-81	S2791_7@1	0.00201725	6.01	0.25
WR-13-81	S2791_9@1	0.00201709	5.93	0.25
WR-12-30B	S2796_1@1	0.00201776	6.26	0.25
WR-12-30B	S2796_11@1	0.00201689	5.83	0.25
WR-12-30B	S2796_12@1	0.00201770	6.23	0.25
WR-12-30B	S2796_13@1	0.00201787	6.32	0.23
WR-12-30B	S2796_14@1	0.00201712	5.95	0.26
WR-12-30B	S2796_14@2	0.00201702	5.89	0.23
WR-12-30B	S2796_17@1	0.00201708	5.92	0.25
WR-12-30B	S2796_19@1	0.00201742	6.10	0.26
WR-12-30B	S2796_19@2	0.00201701	5.89	0.27
WR-12-30B	S2796_2@1	0.00201703	5.90	0.24
WR-12-30B	S2796_21@1	0.00201693	5.85	0.24
WR-12-30B	S2796_3@1	0.00201701	5.89	0.26
WR-12-30B	S2796_4@1	0.00201698	5.88	0.24
WR-12-30B	S2796_5@1	0.00201760	6.19	0.24
WR-12-30B	S2796_6@1	0.00201737	6.07	0.26
WR-12-30B	S2796_6@2	0.00201686	5.81	0.25
WR-12-30B	S2796_7@1	0.00201687	5.82	0.24
WR-12-30B	S2796_8@1	0.00201803	6.40	0.22
WR-13-117	S2800_1@2	0.00201684	5.80	0.26
WR-13-117	S2800_11@3	0.00201695	5.86	0.23
WR-13-117	S2800_12@1	0.00201681	5.79	0.23
WR-13-117	S2800_13@3	0.00201703	5.90	0.26
WR-13-117	S2800_14@3	0.00201693	5.85	0.24
WR-13-117	S2800_14@4	0.00201695	5.86	0.24
WR-13-117	S2800_16@1	0.00201740	6.09	0.24
WR-13-117	S2800_21@2	0.00201653	5.65	0.23
WR-13-117	S2800_3@2	0.00201714	5.96	0.23
WR-13-117	S2800_4@2	0.00201718	5.98	0.24
WR-13-117	S2800_5@2	0.00201684	5.81	0.24
WR-13-117	S2800_8@3	0.00201667	5.72	0.23
WR-13-2	S2797_1@1	0.00201723	6.00	0.24
WR-13-2	S2797_11@1	0.00201703	5.90	0.24
WR-13-2	S2797_11@2	0.00201674	5.75	0.23
WR-13-2	S2797_12@2	0.00201715	5.96	0.25
WR-13-2	S2797_18@1	0.00201713	5.95	0.23
WR-13-2	S2797_19@1	0.00201646	5.61	0.27
WR-13-2	S2797_19@2	0.00201680	5.79	0.24
WR-13-2	S2797_20@1	0.00201728	6.02	0.24
WR-13-2	S2797_3@1	0.00201698	5.88	0.23
WR-13-2	S2797_3@2	0.00201688	5.82	0.22
WR-13-2	S2797_4@1	0.00201711	5.94	0.24
WR-13-2	S2797_5@1	0.00201701	5.89	0.30
WR-13-2	S2797_5@2	0.00201759	6.18	0.24
WR-13-2	S2797_9@1	0.00201716	5.96	0.22
WR-13-2	S2797_9@2	0.00201758	6.17	0.23
WR-13-113B	S2808_1@1	0.00201610	5.44	0.19
WR-13-113B	S2808_12@1	0.00201606	5.42	0.20
WR-13-113B	S2808_16@1	0.00201610	5.44	0.19
WR-13-113B	S2808_2@1	0.00201567	5.22	0.19
WR-13-113B	S2808_20@1	0.00201535	5.06	0.19
WR-13-113B	S2808_21@1	0.00201612	5.45	0.18
WR-13-113B	S2808_23@1	0.00201646	5.62	0.20
WR-13-113B	S2808_5@1	0.00201617	5.47	0.18
WR-13-113B	S2808_5@2	0.00201583	5.30	0.18
CB-5	S2861_1@1	0.002017547	6.16	0.18
CB-5	S2861_3@1	0.002017561	6.16	0.15
CB-5	S2861_4@1	0.002017535	6.15	0.14
CB-5	S2861_4@2	0.002017818	6.29	0.18
CB-5	S2861_5@1	0.002017319	6.04	0.18
CB-5	S2861_5@2	0.002017602	6.19	0.15
CB-5	S2861_6@1	0.002017823	6.29	0.21
CB-5	S2861_7@1	0.002016709	5.74	0.22
CB-5	S2861_9@1	0.002017717	6.24	0.18
CB-5	S2861_12@1	0.002017873	6.32	0.16
CB-5	S2861_14@1	0.002017445	6.11	0.16
CB-5	S2861_16@1	0.002017746	6.26	0.20
CB-5	S2861_18@1	0.002017222	6.00	0.15
CB-5	S2861_18@2	0.002017901	6.33	0.23
WR-13-36	S2805_10@1	0.002021831	8.29	0.18
WR-13-36	S2805_10@2	0.002020755	7.76	0.21
WR-13-36	S2805_12@1	0.002021268	8.01	0.21
WR-13-36	S2805_14@1	0.002020733	7.75	0.19
WR-13-36	S2805_2@1	0.002020277	7.52	0.20
WR-13-36	S2805_2@2	0.002020936	7.85	0.21
WR-13-36	S2805_20@1	0.002021391	8.07	0.21
WR-13-36	S2805_20@1	0.00202042	7.59	0.20
WR-13-36	S2805_4@1	0.00202094	7.85	0.19
WR-13-36	S2805_8@1	0.002020811	7.79	0.20
WR-13-84	S2792_10@1	0.00201985	7.30	0.25
WR-13-84	S2792_11@1	0.00201960	7.18	0.26
WR-13-84	S2792_12@1	0.00201907	6.91	0.22
WR-13-84	S2792_12@2	0.00201905	6.91	0.23
WR-13-84	S2792_15@1	0.00201944	7.10	0.24
WR-13-84	S2792_17@1	0.00201985	7.30	0.26
WR-13-84	S2792_18@1	0.00201965	7.20	0.25
WR-13-84	S2792_19@1	0.00201910	6.93	0.26
WR-13-84	S2792_19@3	0.00201938	7.07	0.24
WR-13-84	S2792_2@1	0.00201949	7.13	0.25
WR-13-84	S2792_20@1	0.00202033	7.55	0.26
WR-13-84	S2792_21@1	0.00201961	7.19	0.26
WR-13-84	S2792_21@2	0.00201928	7.02	0.26
WR-13-84	S2792_4@1	0.00201919	6.97	0.27
WR-13-84	S2792_5@1	0.00201933	7.05	0.27
WR-13-84	S2792_6@1	0.00201926	7.01	0.26
WR-13-84	S2792_6@2	0.00201948	7.12	0.24
WR-13-84	S2792_7@1	0.00201925	7.01	0.23
WR-13-84	S2792_9@1	0.00201932	7.04	0.24
WR-13-84	S2792_9@2	0.00201902	6.89	0.29
WR-13-48	S2810_1@1	0.00202088	7.82	0.18
WR-13-48	S2810_12@1	0.00202117	7.96	0.18
WR-13-48	S2810_13@1	0.00201976	7.26	0.19
WR-13-48	S2810_18@1	0.00202135	8.06	0.19
WR-13-48	S2810_21@1	0.00202112	7.94	0.18
WR-13-48	S2810_21@2	0.00201909	6.92	0.18
WR-13-48	S2810_23@1	0.00202137	8.06	0.21
WR-13-48	S2810_3@1	0.00202095	7.85	0.19
WR-13-48	S2810_5@1	0.00202117	7.96	0.19
WR-13-74	S2799_1@1	0.01189047	6.16	0.24
WR-13-74	S2799_12@1	0.01455912	6.57	0.29
WR-13-74	S2799_14@1	0.01240131	6.40	0.25
WR-13-74	S2799_16@1	0.01354501	6.54	0.27
WR-13-74	S2799_18@1	0.01389026	6.22	0.28
WR-13-74	S2799_20@1	0.01193790	6.50	0.24
WR-13-74	S2799_21@1	0.01247303	6.41	0.25
WR-13-74	S2799_23@1	0.01167091	6.32	0.23
WR-13-74	S2799_24@1	0.01289896	6.42	0.26
WR-13-74	S2799_24@2	0.01305577	6.44	0.26
WR-13-74	S2799_25@1	0.01358415	6.51	0.27
WR-13-74	S2799_5@1	0.01115805	6.39	0.22
WR-13-74	S2799_5@2	0.01357411	6.37	0.27
WR-13-74	S2799_7@1	0.01221998	6.52	0.24
JR-5	S2803_11@1	0.00201579	5.28	0.19
JR-5	S2803_16@1	0.00201594	5.35	0.20
JR-5	S2803_16@2	0.00201594	5.36	0.19
JR-5	S2803_18@1	0.00201583	5.30	0.18
JR-5	S2803_4@1	0.00201578	5.28	0.21

Table 3 (*continued*)

Sample	Spot name	$^{18}O/^{16}O$	$\delta^{18}O_{(VSMOW)}$ (‰)	2σ (‰)
JR-5	S2803_5@1	0.00201593	5.35	0.18
JR-5	S2803_9@1	0.00201600	5.38	0.19
WR-13-14	S2794_1@1	0.00201832	6.54	0.24
WR-13-14	S2794_10@1	0.00201857	6.67	0.26
WR-13-14	S2794_12@1	0.00201796	6.37	0.25
WR-13-14	S2794_15@1	0.00201804	6.40	0.22
WR-13-14	S2794_16@1	0.00201836	6.56	0.23
WR-13-14	S2794_18@1	0.00201653	5.65	0.24
WR-13-14	S2794_18@2	0.00201636	5.57	0.26
WR-13-14	S2794_19@1	0.00201840	6.58	0.27
WR-13-14	S2794_2@1	0.00201789	6.33	0.24
WR-13-14	S2794_2@2	0.00201821	6.49	0.24
WR-13-14	S2794_3@1	0.00201851	6.64	0.25
WR-13-14	S2794_3@2	0.00201833	6.55	0.23
WR-13-14	S2794_4@1	0.00201816	6.46	0.26
WR-13-14	S2794_7@1	0.00201793	6.35	0.24
WR-13-14	S2794_7@2	0.00201796	6.36	0.23
WR-13-14	S2794_9@1	0.00201728	6.03	0.23
WR-13-122	S2806_1@1	0.00201719	5.98	0.21
WR-13-122	S2806_13@1	0.00201715	5.96	0.20
WR-13-122	S2806_16@1	0.00201720	5.98	0.19
WR-13-122	S2806_2@1	0.00201725	6.01	0.19
WR-13-122	S2806_21@1	0.00201602	5.39	0.21
WR-13-122	S2806_22@1	0.00201779	6.28	0.18
WR-13-122	S2806_23@1	0.00201770	6.23	0.21
WR-13-122	S2806_3@1	0.00201738	6.07	0.19
WR-13-122	S2806_8@1	0.00201525	5.01	0.19
WR-13-122	S2806_8@2	0.00201623	5.50	0.21
WR-13-122	S2806_9@1	0.00201733	6.05	0.20
WR-13-100	S2802_13@1	0.00201703	5.90	0.22
WR-13-100	S2802_14@1	0.00201737	6.07	0.19
WR-13-100	S2802_18@1	0.00201746	6.11	0.19
WR-13-100	S2802_2@1	0.00201699	5.88	0.21
WR-13-100	S2802_2@2	0.00201705	5.91	0.21
WR-13-100	S2802_23@1	0.00201726	6.01	0.20
WR-13-100	S2802_3@1	0.00201702	5.90	0.19
WR-13-100	S2802_4@1	0.00201720	5.99	0.22
WR-13-100	S2802_5@1	0.00201746	6.12	0.21
WR-13-100	S2802_7@1	0.00201693	5.85	0.20
JM11-34	S2804_13@1	0.00201740	6.09	0.22
JM11-34	S2804_17@1	0.00201724	6.01	0.19
JM11-34	S2804_17@2	0.00201725	6.01	0.19
JM11-34	S2804_2@1	0.00201709	5.93	0.19
JM11-34	S2804_2@2	0.00201698	5.87	0.20
JM11-34	S2804_20@1	0.00201681	5.79	0.21
JM11-34	S2804_20@2	0.00201707	5.92	0.19
JM11-34	S2804_22@1	0.00201689	5.83	0.20
JM11-34	S2804_3@1	0.00201712	5.95	0.21
JM11-34	S2804_6@1	0.00201767	6.22	0.20
JM11-34	S2804_6@2	0.00201716	5.96	0.18
JM11-34	S2804_9@1	0.00201703	5.90	0.20
BP-1	S2798_1@1	0.00201720	5.99	0.26
BP-1	S2798_1@2	0.00201707	5.92	0.25
BP-1	S2798_10@1	0.00201707	5.92	0.23
BP-1	S2798_11@1	0.00201718	5.98	0.25
BP-1	S2798_13@1	0.00201740	6.08	0.28
BP-1	S2798_15@1	0.00201729	6.03	0.22
BP-1	S2798_15@2	0.00201746	6.11	0.24
BP-1	S2798_2@1	0.00201726	6.02	0.25
BP-1	S2798_20@1	0.00201617	5.47	0.27
BP-1	S2798_20@2	0.00201714	5.96	0.24
BP-1	S2798_22@1	0.00201650	5.64	0.24
BP-1	S2798_5@2	0.00201680	5.79	0.27
BP-1	S2798_6@1	0.00201744	6.10	0.24
BP-1	S2798_6@2	0.00201731	6.04	0.24
BP-1	S2798_7@1	0.00201690	5.83	0.24
BP-1	S2798_8@1	0.00201731	6.04	0.24
BP-1	S2798_9@1	0.00201844	6.60	0.25

9.2. Eastern Oligocene magmatism

Intrusions from the eastern Gangdese belt (none are known to occur in the western part of the belt) have high-K calc-alkaline quartz monzonitic to granitic compositions, similar to the range of published data for these lithologies (Fig. 6A, B). They are somewhat more depleted in HREE relative to the Paleocene-Eocene suite (Fig. 6D), and have pronounced listric-shaped normalized REE patterns that mostly lack significant negative Eu anomalies. These patterns indicate fractionation of hornblende (which preferentially partitions MREE, leading to listric-shaped normalized REE patterns; Davidson et al., 2007; Green and Pearson, 1985; Müntener et al., 2001; Rollinson, 1993; Rooney et al., 2011) and suppression of plagioclase crystallization and fractionation (Naney, 1983; Ridolfi et al., 2010). In combination with the abundance of amphibole phenocrysts in these rocks, these geochemical features suggest that the Oligocene magmas were relatively hydrous (>4 wt.% H_2O: Wang et al., 2014a).

Zircon $\delta^{18}O$ values of sample CB-5 (+5.7‰ and +6.3‰; Fig. 8A) are similar to the values from Paleocene–Eocene rocks, as are the $(^{87}Sr/^{86}Sr)_i$, εNd_i, and $(^{187}Os/^{188}Os)_i$ values (0.7062 to 0.7063, −3.4 to −2.5, and 0.224 to 0.359, respectively). Zircon Hf isotopic values of CB-5 and XB-12-3 are positive, and vary from 3.1 to 6.5 (Zheng et al., 2012) and 0.8 to 6.3 (Table A2), respectively.

The Oligocene igneous rocks have calc-alkaline continental arc-like compositions, with enrichments in LILE (Rb, Ba, Th, U, and K), and depletions in HFSE (Nb and Ta). Published Sr–Nd isotope compositions of Gangdese Oligo-Miocene igneous rocks overlap those of the cospatial Cretaceous Gangdese arc batholith. Despite the compositional and isotopic similarity to the subduction-related Paleocene–Eocene rocks, the Oligocene rocks are unlikely to have been directly subduction-derived, because they formed ~25 m.y. after the onset of India–Asia collision. We suggest that they were likely derived from partial melting of subduction-modified Tibetan lower crust (juvenile) or subcontinental lithospheric mantle in a collisional setting (Hou et al., 2009; Zheng et al., 2012; Wang et al., 2014a).

Table 4
Amphibole and phlogopite O isotope data for the Cenozoic Gangdese magmatic rocks.

Sample number	Mineral	$\delta^{18}O_{(VSMOW)}$ (‰)	2σ (‰)
WR-12-8	Amphibole	6.7	0.1
XG-12-9	Amphibole	6.5	0.1
XG-12-3	Amphibole	5.9	0.1
WR-12-33	Amphibole	5.3	0.1
QL10-4-22	Amphibole	6.3	0.1
QL10-4-9	Amphibole	6.4	0.1
WR-12-52	Phlogopite	9.8	0.1

9.3. Miocene alkaline volcanic rocks

Potassic to ultrapotassic volcanic rocks from across the Gangdese belt have high-K calc-alkaline to shoshonitic, trachyandesitic to trachydacitic compositions (Fig. 6A, B). The eastern Miocene volcanic rocks have high Sr/Y and $[La/Yb]_N$ ratios (Figs. 6D, 7E), with steeper normalized REE patterns from high LREE to low HREE compared with the Paleocene–Eocene and Oligocene rocks. These compositions are similar to those reported in the literature for alkaline volcanic rocks from the western Gangdese belt (Figs. 6 and 7).

Although there are some differences between the chemical compositions of these alkaline rocks from east to west, they do show distinct isotopic compositions. Zircon and amphibole $\delta^{18}O$ values for eastern samples range from +5.0‰ to +6.7‰ (similar to the Paleocene–Eocene and Oligocene rocks), whereas zircons from the western suite have higher values (+6.9 to +8.3‰; Fig. 8A), and whole rocks and phlogopite extend this range to +11.0‰ (Fig. 8B). In addition, zircon Hf isotopic values for eastern samples range from −5.9 to 10.1, whereas zircons from the western suite have lower values (−15.2 to 0.7‰; Fig. 11). One sample from eastern suite has relatively low εHf and εNd values (both below 0), and high $\delta^{18}O$ values. This sample is geographically close to the boundary at

Table 5
Sr–Nd isotope data for the Cenozoic Gangdese magmatic rocks.

Sample number	Age (Ma)	Rb (ppm)	Sr (ppm)	Sm (ppm)	Nd (ppm)	$^{87}Rb/^{86}Sr$	$^{87}Sr/^{86}Sr$	2σ	$(^{87}Sr/^{86}Sr)_i$	$^{147}Sm/^{144}Nd$	$^{143}Nd/^{144}Nd$	2σ	εNd	$(^{143}Nd/^{144}Nd)_i$	$εNd_i$
WR-13-40	58.0	2.2	528.3	3.05	13.58	0.012	0.70515	0.00002	0.70514	0.1357	0.512643	0.000012	0.1	0.51262	0.5
WR-13-81	49.9	208.2	684.7	9.07	49.96	0.880	0.70650	0.00002	0.70588	0.1098	0.512418	0.000009	−4.3	0.51238	−3.7
WR-12-30B	67.8	138.1	306.5	4.37	23.27	1.304	0.70583	0.00002	0.70458	0.1136	0.512657	0.000008	0.4	0.51261	1.1
WR-13-117	53.0	97.3	167.1	5.79	29.83	1.685	0.70862	0.00002	0.70735	0.1173	0.512391	0.000007	−4.8	0.51235	−4.3
WR-13-109	43.2	104.6	311.2	7.28	26.96	0.972	0.70615	0.00002	0.70555	0.1633	0.512619	0.000007	−0.4	0.51257	−0.2
WR-13-113A	43.2	75.9	401.8	4.36	21.01	0.546	0.70565	0.00002	0.70532	0.1253	0.512612	0.000010	−0.5	0.51258	−0.1
WR-13-113B	43.2	97.7	77.2	5.31	27.15	3.663	0.71014	0.00005	0.70789	0.1183	0.512600	0.000005	−0.7	0.51257	−0.3
WR-13-53	21.2	726.2	598.2	28.95	133.84	3.520	0.72732	0.00001	0.72626	0.1308	0.511855	0.000009	−15.3	0.51184	−15.1
WR-13-26	18.0	243.6	297.4	4.88	27.84	2.373	0.71705	0.00002	0.71645	0.1060	0.512222	0.000010	−8.1	0.51222	−7.9
WR-13-48	23.0	240.0	767.9	14.4	88.2	0.905	0.71504	0.00002	0.71474	0.0985	0.512043	0.000005	−11.6	0.51203	−11.3
WR-13-18	14.0	243.6	297.4	10.14	54.25	2.373	0.71705	0.00002	0.71658	0.1131	0.511933	0.000008	−13.8	0.51192	−13.6
JR-5	16.2	103.5	803.8	4.05	19.88	0.372	0.70574	0.00002	0.70566	0.1232	0.512458	0.000010	−3.5	0.51244	−3.4
WR-13-122	11.0	244.8	1110.5	14.12	93.27	0.638	0.71220	0.00002	0.71210	0.0915	0.512150	0.000005	−9.5	0.51214	−9.4
WR-13-100	14.0	145.0	683.0	7.44	41.82	0.614	0.70668	0.00002	0.70656	0.1076	0.512297	0.000008	−6.6	0.51229	−6.5
BP-1	16.0	84.7	126.3	1.76	7.32	1.939	0.70670	0.00002	0.70626	0.1451	0.512588	0.000009	−1.0	0.51257	−0.9

~89° E. We interpret the small variation of geochemistry is caused by the heterogeneity of crust and mantle.

Strontium and neodymium isotopic compositions are also distinct both from the earlier igneous rocks, and by longitude. The eastern volcanic rocks have higher $(^{87}Sr/^{86}Sr)_i$ values (0.7057 to 0.7121; Fig. 9C), and lower $εNd_i$ (−3.4 to −9.4; Figs. 9A, 11B) compared with the Paleocene–Eocene suite, while the western suite has even higher $(^{87}Sr/^{86}Sr)_i$ (0.7069 to 0.7263; Fig. 9C) and lower $εNd_i$ values (−6.0 to −15.1; Figs. 9A, 11B).

These Sr, Nd, O, Os, and Hf isotopic data all suggest a significant crustal involvement in the petrogenesis of these alkaline magmas, particularly for the western suite, but their low Os isotopic compositions, and high Ni (20.2–167.4 ppm) and Cr (22.8–529 ppm) compositions also indicate a mantle source. We thus consider that these magmas were likely derived by melting of Tibetan SCLM, with contamination by crustal melts. However, the extremely high Sr–O and low Nd–Hf isotopic compositions of the western suite extend well beyond the range of compositions thought to represent Tibetan crust in the Gangdese belt ($^{87}Sr/^{86}Sr < 0.71$, εNd > −10, and εHf > 0; as reviewed in Zhao et al., 2009; Zhu et al., 2011), but they are similar to the compositions of High Himalayan crystalline basement, which is commonly used as a proxy for the Indian plate lithosphere ($^{87}Sr/^{86}Sr = 0.74$ to 0.76), $δ^{18}O = +10 - +14‰$, εNd = −18 to −10; France-Lanord et al., 1988; Zhao et al., 2009). We therefore propose that the western alkaline

Table 6
Osmium isotope data for the Cenozoic Gangdese magmatic rocks.

Sample number	Analysis number	Weight (g)	Re (ppt)	2σ	Os (ppt)	2σ	$^{187}Re/^{188}Os$	2σ	$^{187}Os/^{188}Os$	2σ	$(^{187}Os/^{188}Os)_i$
WR-13-37	WR-13-37	4.0	43.0	0.1	7.76	0.05	27.3	0.2	0.2882	0.0024	0.262
WR-13-40	WR-13-40	4.0	285.4	0.9	7.32	0.03	194.8	1.0	0.4139	0.0031	0.226
WR-13-81	WR-13-81	4.0	205.4	0.7	2.53	0.01	423.2	2.8	0.7460	0.0070	0.394
WR-13-117	WR-13-117	4.0	44.0	0.1	0.75	0.01	305.1	2.8	0.7332	0.0085	0.464
WR-13-118	WR-13-118	4.0	52.2	0.2	1.02	0.00	261.3	1.5	0.5949	0.0061	0.364
CMD-17A	CMD-17A	4.0	7.3	0.3	9.02	0.09	3.9	0.2	0.2384	0.0047	0.236
CMD-17B	CMD-17B	4.0	8.4	0.2	6.62	0.11	6.1	0.2	0.3621	0.0099	0.359
CMD-32A	CMD-32A	4.0	8.2	0.2	4.65	0.04	8.5	0.2	0.2693	0.0086	0.265
CMD-32B	CMD-32B	4.0	13.2	0.3	4.38	0.03	14.3	0.3	0.2951	0.0031	0.288
CMD-33A	CMD-33A	4.0	17.8	0.5	5.28	0.05	16.3	0.5	0.2318	0.0111	0.224
CMD-33B	CMD-33B	4.0	11.0	0.3	3.82	0.06	13.8	0.4	0.3394	0.1424	0.332
WR-13-53	WR-13-53	4.0	157.3	0.5	160.5	1.9	4.7	0.1	0.1580	0.0027	0.156
WR-13-84	WR-13-84	4.0	9.6	0.1	2.93	0.01	16.0	0.2	0.1936	0.0015	0.188
WR-13-85	WR-13-85	4.0	34.1	0.1	3.33	0.02	49.7	0.3	0.1977	0.0016	0.182
WR-13-31	WR-13-31	4.0	133.2	0.4	1.02	0.01	723.0	7.0	1.2466	0.0149	1.006
WR-13-26	WR-13-26	4.0	53.2	0.2	1.06	0.01	269.5	1.8	1.0310	0.0085	0.948
10YR07	10YR07	4.0	76.7	0.3	0.89	0.00	442.6	2.3	0.6682	0.0059	0.550
WR-13-48	WR-13-48	4.0	20.6	0.1	2.99	0.02	37.2	0.3	1.0494	0.0097	1.035
WR-13-122	WR-13-123	4.0	54.3	0.4	4.93	0.03	53.5	0.6	0.1844	0.0021	0.175
WR-13-122	WR-13-124A	4.0	42.9	0.2	6.00	0.03	34.7	0.2	0.1656	0.0013	0.159
WR-13-122	WR-13-124B	4.0	39.7	0.3	5.23	0.03	36.7	0.3	0.1602	0.0014	0.153
WR-13-122	WR-13-125	4.0	68.8	0.2	3.87	0.02	86.7	0.6	0.2263	0.0024	0.210
WR-13-100	WR-13-100A	4.0	1348.4	6.0	39.04	0.35	168.4	1.7	0.2157	0.0029	0.176
WR-13-100	WR-13-100B	4.0	660.4	2.6	35.17	0.16	91.3	0.5	0.1997	0.0018	0.178
JR-5	JR-5	4.0	61.9	0.2	3.87	0.02	77.9	0.4	0.2130	0.0031	0.192
JM11-34	JM11-34	4.0	405.5	1.2	5.91	0.02	340.9	1.6	0.3602	0.0047	0.269
QL02-01	QL02-01	4.0	14.9	0.3	0.75	0.03	91.9	5.0	0.8647	0.0521	0.835
QL02-04-2	QL02-04-2	4.0	10.7	0.3	4.03	0.05	12.8	0.4	0.2900	0.0189	0.286
QL02-07	QL02-07	4.0	21.2	0.5	0.90	0.02	108.1	3.2	0.4872	0.0773	0.452
QL02-10	QL02-10	4.0	8.0	0.4	0.99	0.03	36.7	2.2	0.4233	0.0229	0.411
QL02-13	QL02-13	4.0	61.5	0.6	1.07	0.02	284.5	5.2	0.4262	0.0114	0.334
QL02-28	QL02-28A	4.0	8.4	0.2	1.24	0.03	32.7	1.3	0.5063	0.0249	0.496
QL02-28	QL02-28B	4.0	8.4	0.2	3.90	0.04	10.3	0.3	0.5390	0.0367	0.536

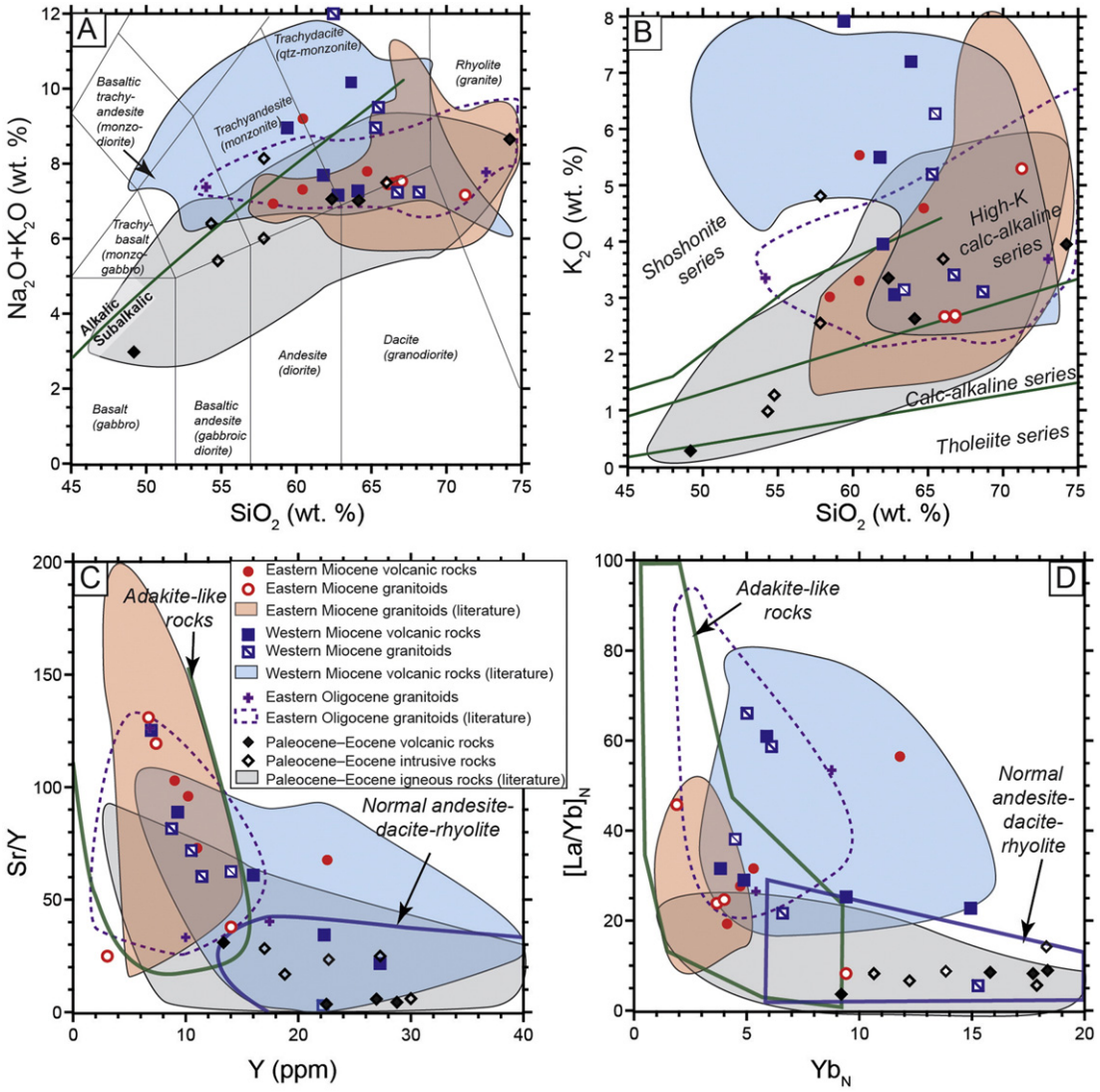

Fig. 6. A. Total alkali–silica diagram for Paleocene–Eocene, Oligocene, and Miocene igneous rock samples from this study (after Le Maitre, 1989, and Middlemost, 1994). The alkaline/subalkaline boundary of Irvine and Baragar (1971) is shown. B. SiO_2 vs. total K_2O (after Rickwood, 1989). C. Sr/Y vs. Y; "Adakite-like rock" field is from Defant and Drummond (1990). D. $[La/Yb]_N$ vs. Yb_N; "Adakite-like rock" field is from Martin (1999). Typical fields for Paleocene–Eocene, Oligocene, and Miocene igneous rock samples from the literature (see text for data sources) are shown.

volcanic rocks include a component of melt or fluids (~3–25%; Fig. 9C, D) from the underthrust Indian lithosphere.

9.4. Miocene granitoid plutons

Granitoid plutons from across the Gangdese belt have calc-alkaline to high-K calc-alkaline (rare shoshonitic), quartz monzonitic, granodioritic, and granitic compositions (Fig. 6A, B). They have high Sr/Y and $[La/Yb]_N$ ratios (Fig. 6C, D). The eastern granitoids have pronounced listric-shaped normalized REE patterns, similar to the Oligocene suite, whereas the western granitoids have steep normalized REE patterns from high LREE to low HREE (Fig. 7G), similar to the western alkaline volcanic rocks (Fig. 7E).

As for the alkaline volcanic rocks, zircon and amphibole $\delta^{18}O$ values for granitoid samples from the eastern Gangdese belt (+5.5‰ to +6.6%) are similar to values from the older Paleocene–Eocene and Oligocene rocks, but the western granitoids (like the western alkaline volcanic rocks) extend to higher values (up to +8.8‰; Fig. 8). In addition, the western granitoids have lower zircon Hf isotopic values ($\varepsilon Hf_i = -13.0$ to 3.9; Fig. 11; Table A2), whereas the eastern granitoids commonly have positive εHf_i (BP-1: 1.4–8.7, Table A2; $\varepsilon Hf_i > 0$ for Qulong and Jiama intrusions, Hou et al., 2012).

Strontium, neodymium, and osmium isotopic ratios for the eastern granitoids are also similar to the Paleocene–Eocene suite, but the western granitoids have higher $(^{87}Sr/^{86}Sr)_i$ ratios (0.7147 to 0.7165; Fig. 9C) and lower εNd_i values (−7.9 to −11.3; Fig. 9), comparable to the coeval western alkaline volcanic rocks. However, $(^{187}Os/^{188}Os)_i$ values are much higher than any of the other lithologies (0.550 to 1.035; Fig. 10).

We interpret these data to indicate that the eastern Miocene granitoids, like the cospatial Oligocene granitoids, were derived by partial melting of subduction-modified Tibetan lithosphere (mainly lower crust: Hou et al., 2004; Guo et al., 2007; Li et al., 2011; Wang et al., 2014a). In contrast, the isotopic compositions of the western granitoids suggest a similar source to the coeval and cospatial alkaline volcanic rocks, but with a higher degree of crustal contamination upon emplacement (as reflected in their crustal Os isotopic values; Fig. 10).

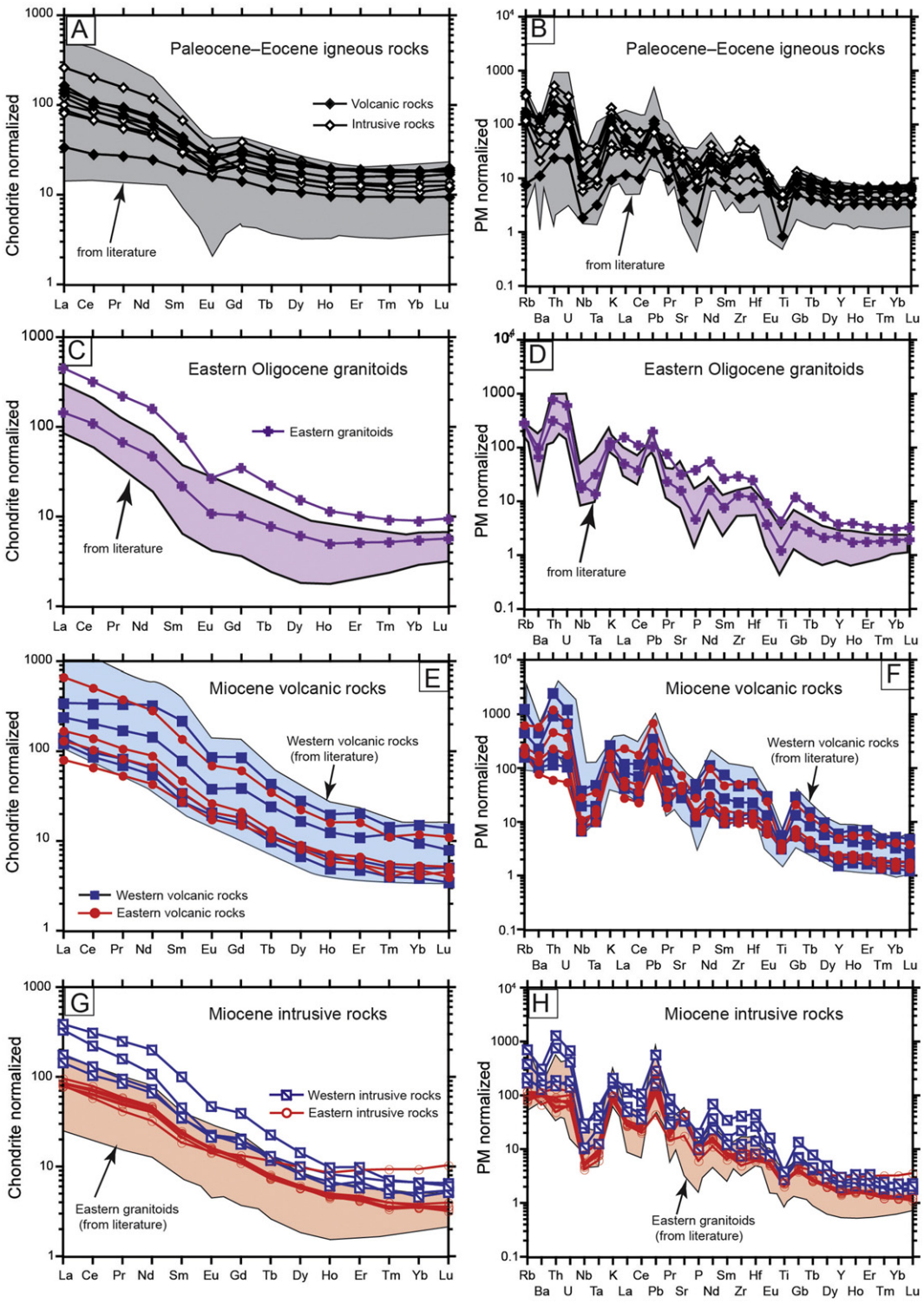

Fig. 7. Chondrite- and primitive mantle- (PM) normalized trace element diagrams for Paleocene–Eocene, Oligocene, and Miocene samples of igneous rocks from this study (see text and Table 1 for data sources): A and B. Paleocene–Eocene igneous rocks; C and D. Oligocene igneous rocks; E and F. Miocene volcanic rocks; G and H. Miocene intrusive rocks. Normalization values are from Sun and McDonough (1989). Typical fields for Paleocene–Eocene, Oligocene, and Miocene igneous rock samples from the literature (see text for data sources) are shown.

In order to validate the magmatic source of eastern Miocene granitoids, and assess the effect of crustal contamination for the formation of eastern Miocene granitoids, we have used the EC-AFC model to simulate interaction between the juvenile lower crust/subduction modified lower crust and possible crustal contaminants (Fig. 13A). Two juvenile lower crust candidates are used: one is Jurassic basalt (YB5-1: Hou et al., 2015) and the other is Eocene gabbro (AG0364-2: Dong et al., 2006b). The crustal contaminants are average upper and lower crusts (Bohrson and Spera, 2001). The simulations indicate that upper crustal contaminations could explain the trend of the trace element (such as Nd) and Sr–Nd isotopic data of Miocene granitoids (Fig. 13A). However, εNd_i vs. SiO_2 plot

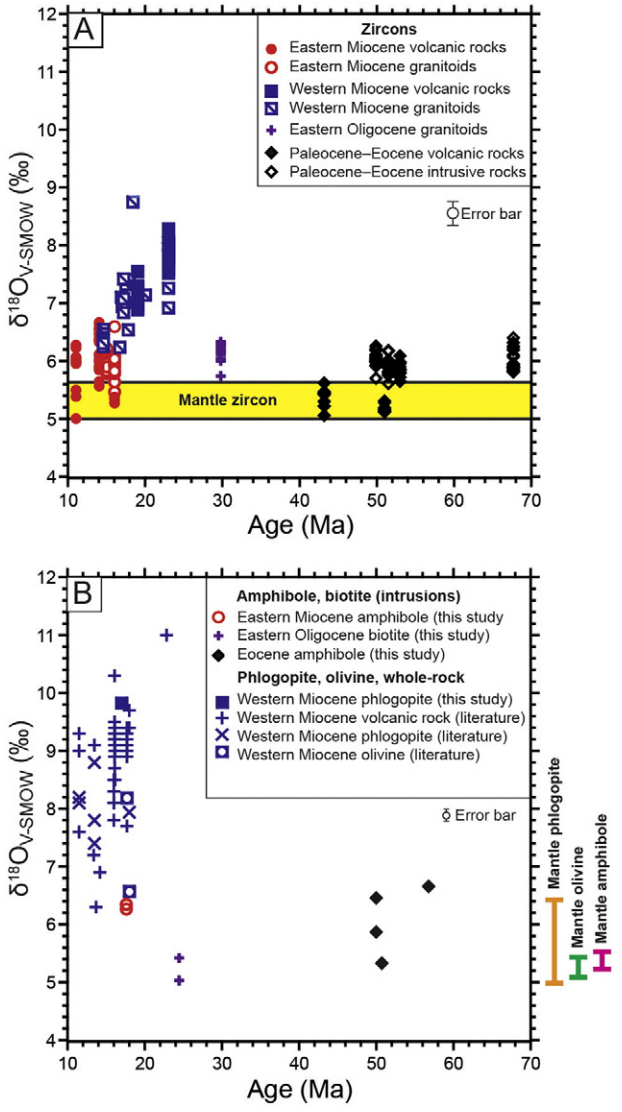

Fig. 8. Oxygen isotopic compositions versus age for (A) zircon, and (B) amphibole, clinopyroxene, phlogopite, olivine, and whole-rock for Cenozoic igneous rocks from the Gangdese belt (see text and Table 1 for data sources, 2 sd for all samples and references). Mantle phlogopite values: +5.74 ± 0.73‰ (Mattey et al., 1994a), mantle olivine values: +5.28 ± 0.18‰ (Mattey et al., 1994b), mantle amphibole values: +5.3–5.6‰ (Chazot et al., 1997), mantle zircon values: $\delta^{18}O = +5.3 \pm 0.3‰$ (Valley et al., 1998).

(Fig. 13B) for Miocene granitoids shows that the felsic intrusions have higher εNd_i values, which are hard to explain by crustal contamination. Therefore, a mixing model for the origin of the Miocene granitoids is proposed. In this model, the formation of these rocks occurred by mixing of mafic and low-εNd_i melts and felsic and high-εNd_i melts (Fig. 13B). The mafic and low-εNd_i melts are represented by potassic and ultrapotassic volcanic rocks, which are formed by partial melting of highly metasomatized lithospheric mantle (Fig. 13C). The felsic and high-εNd_i melts are represented by melts from partial melting of juvenile/subduction modified lower crust. We have used Sr–Nd two end-member mixing model (DePaolo, 1980) to simulate magma mixing between the melts from juvenile lower crust (Jurassic basalt of sample YB5-1 and the Eocene gabbro of sample AG0364-2) and highly metasomatized lithospheric mantle (Trachyandesite WR-13-122 with the lowest $(^{187}Os/^{188}Os)_i$ value of 0.153, Table 6). The simulations indicate the mixing of alkaline mafic melts from highly metasomatized lithospheric mantle with felsic melts from partial melting of Tibetan juvenile lower crust can generate trend of the trace element (such as Nd) and Sr–Nd isotopic data of Miocene granitoids.

10. Implications for geodynamic change

Our new geochemical and isotopic data for Cenozoic igneous rocks from the Tibetan Gangdese belt are interpreted to reflect the diachronous transition from subduction-related to collisional magmatism, and finally to underthrusting of the Indian lithosphere.

Paleocene–Eocene intermediate-composition intrusive and volcanic rocks are calc-alkaline to high-K calc-alkaline, and have similar geochemical and isotopic compositions to normal subduction-related magmatism. They are thought to have formed during the final stages of subduction of Neo-Tethyan lithosphere, and incipient collision between the Greater Indian plate and the accretionary Eurasian margin (i.e., the Lhasa terrane of southern Tibet). These early Paleogene rocks are associated with few porphyry-type deposits, possibly because the magmas appear to have been relatively anhydrous (evolved primarily by fractionation of pyroxene and plagioclase; Wang et al., 2014a) and less oxidized (−1.2 to +0.8; Wang et al., 2014c). We suggest that these infertile magmatic features (Lee et al., 2009, 2012; Wang et al., 2014a) are controlled by Neo-Tethyan slab rollback and breakoff (Chung et al., 2005; Wang et al., 2015). By the time of oceanic slab breakoff, the asthenosphere will rise rapidly into the lithosphere, the thermal anomaly can trigger subduction-modified lithosphere partial melting and generate a wide range of alkaline to calc-alkaline melts (Wang et al., 2015). This melting mechanism is different from the typical arc magmatism, where released water (accompanied with high oxidation materials) from oceanic slab dehydration is the trigger. We think the unique magma melting mechanism in the early Paleogene of Gangdese belt produced the relatively dry and less oxidized magmas.

Oligocene magmatism was restricted to the eastern Gangdese belt with high-K calc-alkaline granitoids, and to the Qiangtang terrane with high-K calc-alkaline to shoshonitic volcanic rocks. The granitoids mostly occur as small plutons, and are compositionally similar to the earlier Paleocene–Eocene suite, but show greater fractionation of REE, higher Sr/Y and $[La/Yb]_N$ ratios, and mostly lack significant Eu anomalies. These compositions have been interpreted by Wang et al. (2014a) to reflect increasing water content in these Oligocene magmas. The rocks are isotopically similar to the Paleocene–Eocene suite, and were likely derived by partial melting of previously subduction-modified Tibetan lithosphere. A few small porphyry deposits are associated with these Oligocene granitoid intrusions. The sparse alkaline volcanic rocks are barren, have moderate $(^{87}Sr/^{86}Sr)_i$ ratios (0.7060–0.7092) and negative εNd_i values (−9.2 to −3.8; Ding et al., 2003; Liu et al., 2008), and only erupted in the Qiangtang terrane (to the north of the western Gangdese belt; Fig. 2). This region was located to the north of the main Cretaceous–Paleocene Gangdese arc, therefore not fertilized by the previous subduction. We think less fluids and metals in the magmatic source (lower crust or SCLM) of this region result in infertile magmas and less mineralization (Lee et al., 2012; Richards et al., 2013). We suggest that the Oligocene alkaline volcanic magmas were derived by partial melting of enriched Tibetan SCLM during early breakoff of Greater India slab started in the western Tibet at ~25 ± 5 Ma (Fig. 14).

The Oligo-Miocene igneous rocks formed ~35–25 m.y. after the onset of India–Asia collision, and cannot therefore be directly related to subduction. A significant geochemical and isotopic change is observed in Miocene magmatism, which was characterized predominantly by calc-alkaline to high-K calc-alkaline plutonism in the eastern part of the Gangdese belt (east of ~89° E) and alkaline volcanism to the west (although minor high-K calc-alkaline to shoshonitic plutonism occurs in the west, and minor alkaline volcanism in the east).

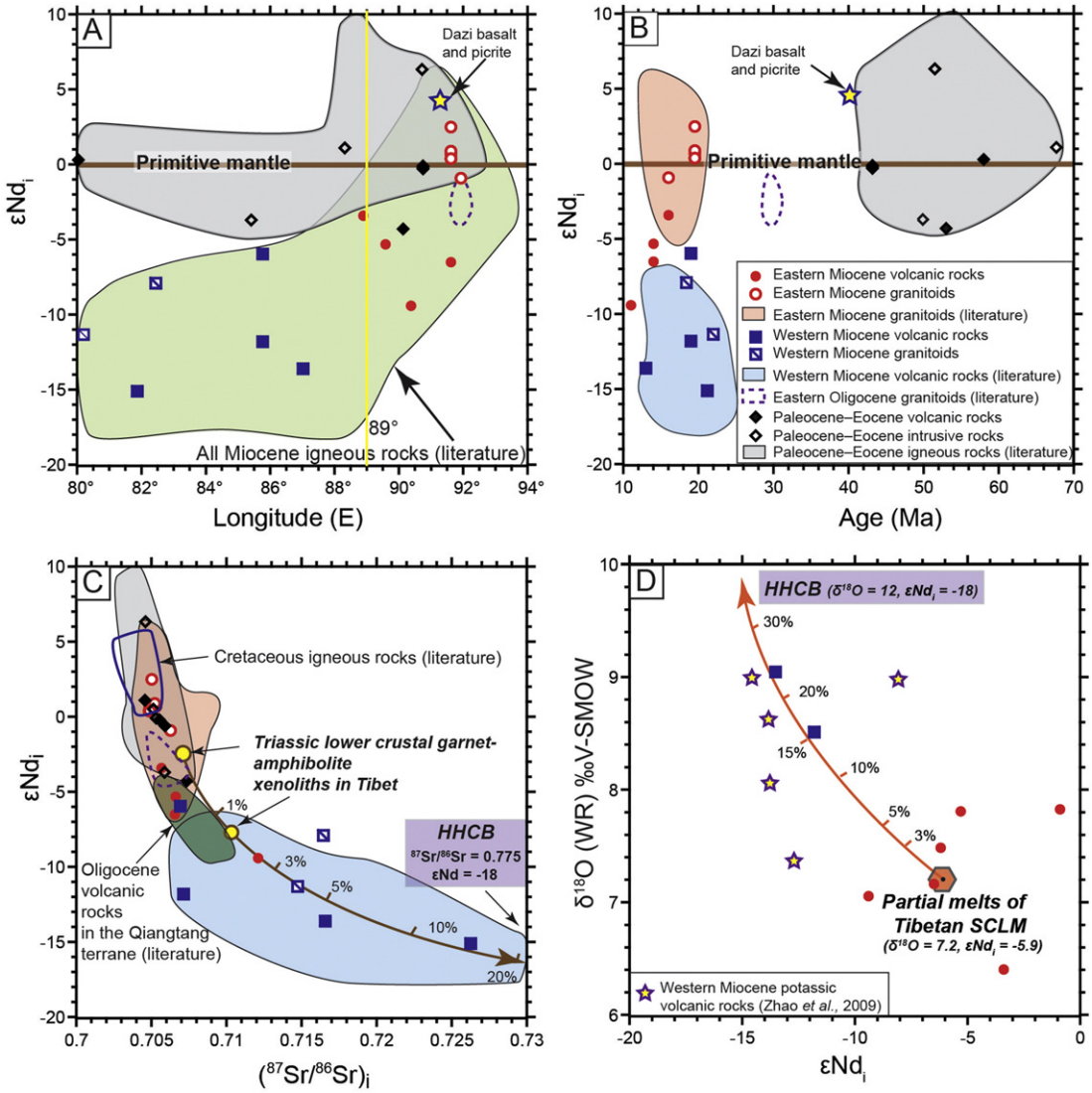

Fig. 9. A. εNd_i vs. longitude; B. εNd_i vs. age; C. εNd_i vs. $(^{87}Sr/^{86}Sr)_i$; (D) Whole-rock $\delta^{18}O$ vs. εNd_i. Values of Dazi basalt and picrite are from Gao et al. (2010). In C, the green line shows mixing between lower crustal garnet–amphibolite xenoliths in Tibet, which are thought to represent Tibetan lithospheric mantle and High Himalayan crystalline basement melts (HHCB: thought to represent the composition of the Indian craton) (for mixing model details, see Wang et al., 2014b). Qiangtang Oligocene volcanic rock compositions are from Ding et al. (2003) and Liu et al. (2008); Cretaceous igneous rock compositions are from Wen (2007) and Zheng et al. (2014a). In D, the orange line shows mixing (ticks on the curve give percentage of assimilation) between melts of HHCB ($\delta^{18}O = 12$, $\varepsilon Nd_i = -18$; France-Lanord et al., 1988; Inger and Harris, 1993) and partial melts of the Tibetan SCLM (represented by average of eastern Miocene alkaline volcanic rocks with mantle Os isotopic ratios: $\delta^{18}O = 7.2$, $\varepsilon Nd_i = -5.9$; magma $\delta^{18}O$ values were obtained from zircon $\delta^{18}O$ values, using $\delta^{18}O$ (Zircon-WR) $= \delta^{18}O$ (Zircon) $- \delta^{18}O$ (WR) ≈ -0.0612 (wt.% SiO_2) + 2.5: Valley et al., 2005). Abbreviations: HHCB = High Himalayan crystalline basement; SCLM = sub-continental lithospheric mantle.

The eastern calc-alkaline to high-K calc-alkaline granitoids are broadly compositionally similar to the Paleocene–Eocene and Oligocene suites, but show significant amphibole fractionation and lower Dy/Yb ratios, and are interpreted to be even more hydrous and oxidized than the earlier suites (Davidson et al., 2007; Zellmer et al., 2012; Wang et al., 2014a, 2014c). Sr–Nd isotopic compositions are also similar, but extend to higher $(^{187}Os/^{188}Os)_i$ values, which are interpreted to reflect crustal melts (partial melting of juvenile lower crust) in generation of these relatively felsic (granodioritic to granitic) rocks. The small number of granitoid plutons that occur in the western part of the Gangdese belt (west of ~89° E) are compositionally similar to their eastern counterparts, but they are slightly more potassic, and have significantly elevated $\delta^{18}O$, $(^{87}Sr/^{86}Sr)_i$, and $(^{187}Os/^{188}Os)_i$ ratios, and lower εNd_i values. These isotopic values are interpreted to reflect a significant crustal involvement in these magmas, but more specifically, the very low εNd_i and εHf_i values may indicate the involvement of partial melts from the underthrust Indian crust, because such low values are not known from any potential crustal sources in the Tibetan lithosphere in the southern Lhasa subterrane (mostly juvenile crust: Zhu et al., 2011).

High-K calc-alkaline to shoshonitic volcanism is widespread in the western Gangdese belt, but of limited extent in the east. The few eastern volcanic rocks sampled show slightly higher $(^{87}Sr/^{86}Sr)_i$, lower εNd_i and $\delta^{18}O$ values, and highly variable εHf_i values than their coeval eastern granitoids. In contrast, the western alkaline volcanic rocks show the highest $(^{87}Sr/^{86}Sr)_i$ and $\delta^{18}O$ values, and the lowest εNd_i and εHf_i values, and are interpreted to reflect the involvement of partial melts from the underthrust Indian lithosphere (Fig. 14).

Underthrusting of the Indian lithosphere beneath Tibet has been spotted by seismic tomographic studies, and the present-extent of

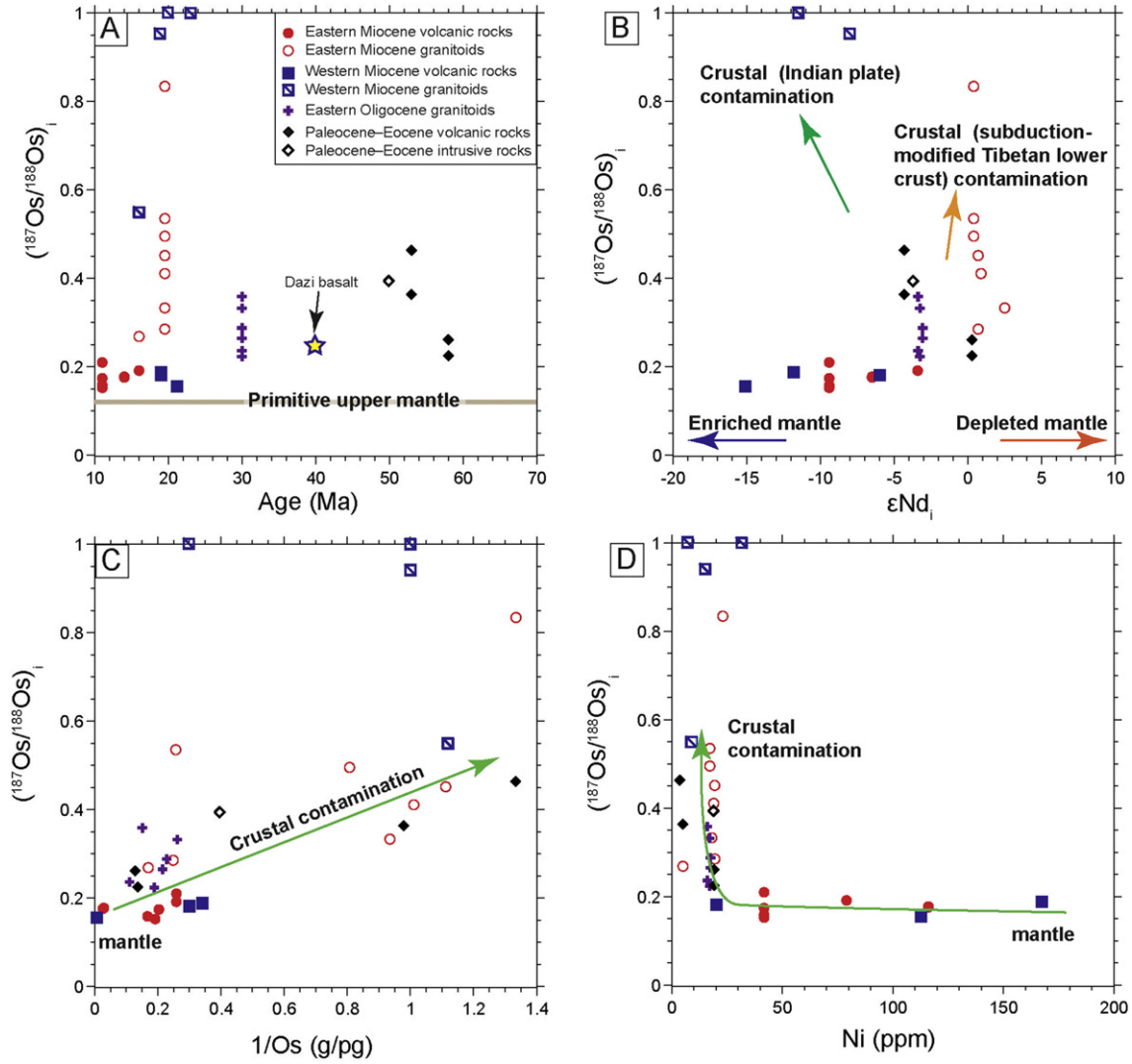

Fig. 10. A. $(^{187}Os/^{188}Os)_i$ vs. age; B. $(^{187}Os/^{188}Os)_i$ vs. εNd_i; C. $(^{187}Os/^{188}Os)_i$ vs. 1/Os (g/pg); D. $(^{187}Os/^{188}Os)_i$ vs. Ni. Present day primitive upper mantle $^{187}Os/^{188}Os = 0.1296 \pm 0.0008$ (Meisel et al., 2001). Value of Dazi basalt is from Zhou (2012). Apparent trends for crustal contamination are also shown ($^{187}Os/^{188}Os \approx 1$–1.5 for the crust, 0.1100–0.1500 for the mantle: Shirey and Walker, 1998; Widow et al., 1999).

underthrusting has passed the Bangong–Nujiang suture in the western Tibet, but not in the eastern Tibet (Kumar et al., 2006; Li et al., 2008; Kind and Yuan, 2010; Zhao et al., 2010; Shokoohi Razi et al., 2014). Fast seismic velocities (~8.4 km/s) were detected at the depth of ~90 km the Tibetan plateau, and are correspondent to eclogite at this depth (Huang et al., 2009; Shokoohi Razi et al., 2014). This fast-velocity material extends to the north of 32° N (to the north of Bangong–Nujiang suture), and such a long extension only exists in the western Tibet (Shokoohi Razi et al., 2014). This is likely localized formation of eclogite during underthrusting of the Indian lower crust in the Miocene. We suggest that the prograde metamorphism of the underthrust Indian lower crust released high $\delta^{18}O$ and low εNd and εHf melts ± fluids into the Tibetan SCLM, and triggered low-degree partial melting of the SCLM and formation of western ultrapotassic volcanic rocks. The dehydrated Indian lower crust transformed to eclogite, and shows the fast velocity feature in the western Tibet. The breakoff of Greater India slab started in the west at ~25 ± 5 Ma, and the tear propagated eastward until final detachment beneath eastern Tibet at ~10 ± 5 Ma (Van der Voo et al., 1999; Replumaz et al., 2010). We suggest that this diachronous breakoff event triggered upwelling of asthenospheric mantle and partial melting of previous subduction-modified Tibetan lithosphere, and generated late Oligocene magmatism (29–31 Ma: Ding et al., 2003; Liu et al., 2008) to the north of the western Gangdese belt (south Qiangtang terrane, Fig. 14) and Miocene magmatism in the Gangdese belt (Hou et al., 2009; Wang et al., 2014a, 2014b). Late Oligocene magmas to the north of western Gangdese belt were derived from partial melting of the SCLM with involvement of upwelling asthenospheric melts (Ding et al., 2003; Wang et al., 2014b). Miocene magmas in the western Gangdese belt were partially derived from the underthrust Indian plate lithosphere, which limited the involvement of asthenospheric melts and the extent of lithospheric partial melting (Fig. 14). In contrast, Miocene magmas in the eastern Gangdese belt were from partial melting of subduction-modified Tibetan lithosphere, and show similar lithogeochemical and isotopic compositions with Cretaceous–Eocene arc rocks.

11. Implications for metallogenesis

Arc magmatism can leave a large amount of hydrous residue at the base of the crust and SCLM (Kay and Mpodozis, 2001; Richards,

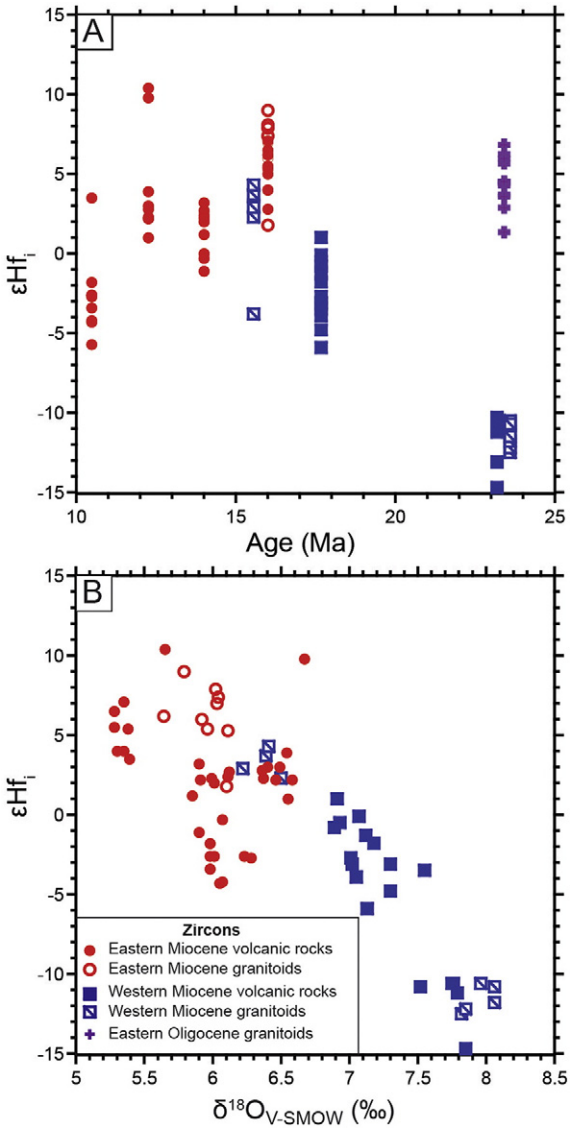

Fig. 11. Zircon hafnium isotopic compositions versus age (A), and oxygen isotopic compositions (B) for Oligo-Miocene igneous rocks from the Gangdese belt.

2009). Earlier arc Paleocene–Eocene magmas are less oxidized, and may have left much of their metals in the mantle and lower crust (Wang et al., 2014c). Therefore, the subduction modified Tibetan lithosphere is thought to be fertile. Miocene porphyry-type deposits are rare in the western Gangdese belt, and we interpret the evidence for Indian plate underthrusting in the western Gangdese belt to indicate that this process has limited the melting of subduction-modified Tibetan lower crust, and thereby limited the generation of fertile

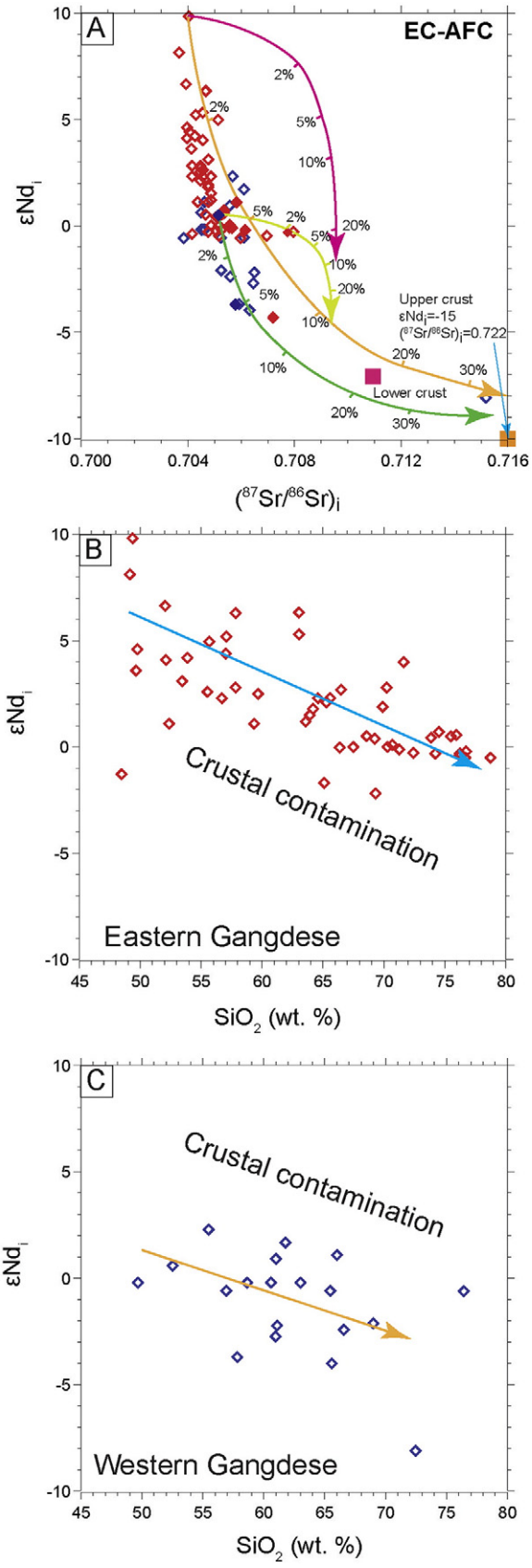

Fig. 12. A. $(^{87}Sr/^{86}Sr)i$ vs. εNd_i; B and C. εNd_i vs. SiO_2 plots for Paleocene–Eocene igneous rocks in Gangdese belt. Also shown are crustal contamination vectors calculated using EC-AFC thermodynamic model (Bohrson and Spera, 2001; Spera and Bohrson, 2001; input parameters are listed in Appendix A): the most isotopically primitive basalt WR-13-40 is used to model the composition of western Gangdese magma entering the crust; possible crustal contaminants are represented by average upper (yellowish green) and lower crust (green) from Bohrson and Spera (2001). The tick on curves indicates a percentage of assimilated contaminant. In addition, the most isotopically primitive gabbro AG0364-2 (Dong et al., 2006b) is used to model the composition of eastern Gangdese magma entering the crust; possible crustal contaminants are represented by average upper (orange) and lower crusts (pinkish red) from Bohrson and Spera (2001). Crustal contamination trend is shown in B and C.

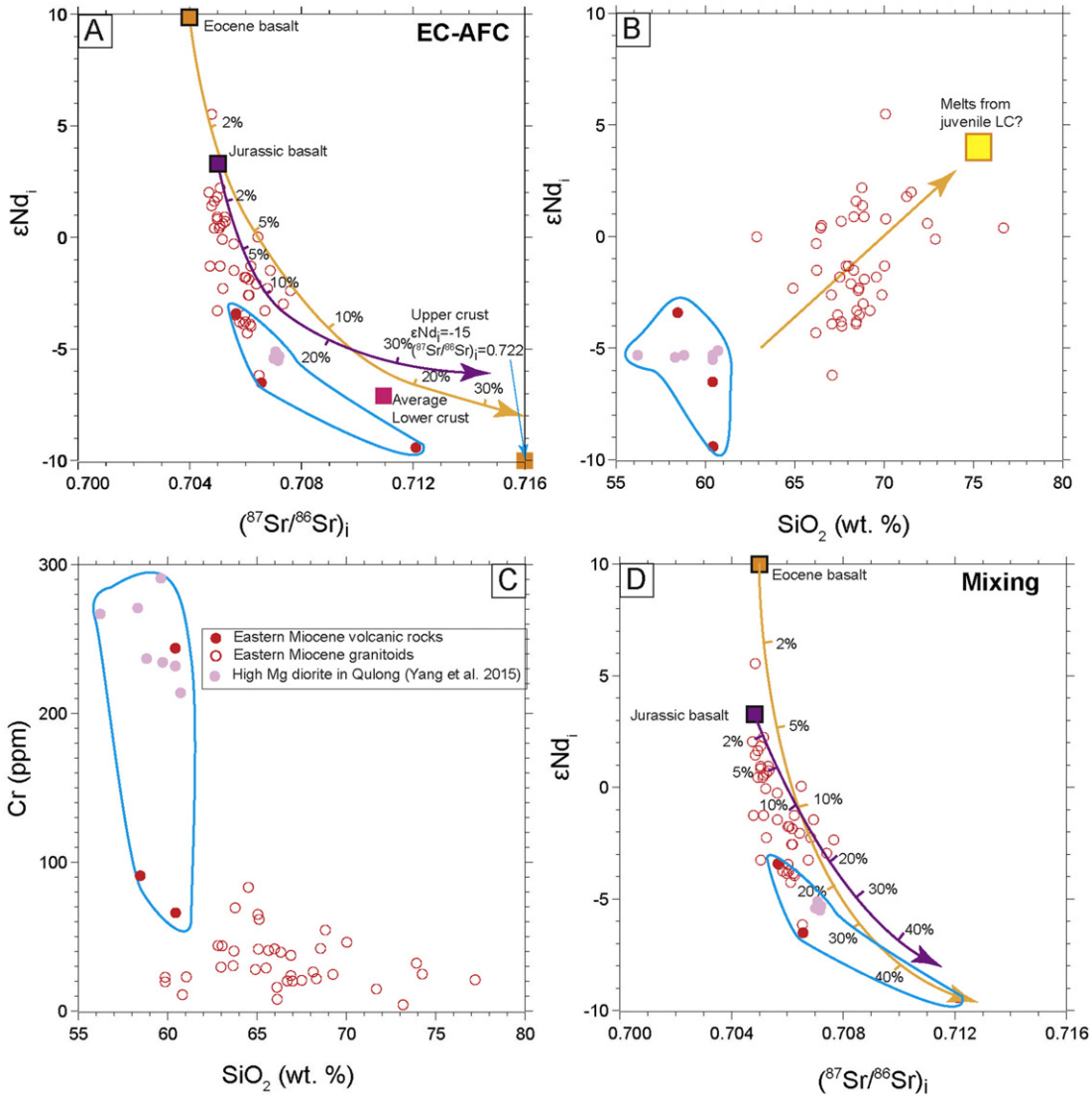

Fig. 13. A and B. $(^{87}Sr/^{86}Sr)_i$ vs. εNd_i; C. εNd_i vs. SiO_2; D. Cr vs. SiO_2 for Miocene igneous rocks in eastern Gangdese belt. In A: crustal contamination vectors calculated using EC-AFC thermodynamic model (Bohrson and Spera, 2001; Spera and Bohrson, 2001; input parameters are listed in Appendix A): the most isotopically primitive Eocene gabbro AG0364-2 (Dong et al., 2006b) and Jurassic basalt YB5-1 are used to model the composition of melts from juvenile lower crust entering the upper crust; possible crustal contaminants are represented by average upper (orange for Eocene juvenile lower crust, and purple for Jurassic lower crust) from Bohrson and Spera (2001). The tick on curves indicates a percentage of assimilated contaminant. The blue line cycles the Qulong high Mg diorite in eastern Gangdese belt (Yang et al., 2015). In B: the orange line shows mixing Eocene gabbro AG0364-2 (Dong et al., 2006b), which are thought to represent Tibetan juvenile lower crust, and High Himalayan crystalline basement melts (HHCB: thought to represent the composition of the Indian craton). Meanwhile, the purple line shows mixing Jurassic basalt YB5-1 (Hou et al., 2015), which is also thought to represent Tibetan juvenile lower crust, HHCB.

magmas. In contrast, in the eastern part of the belt below which underthrusting had not extended in the Miocene, upwelling asthenosphere (in response to slab breakoff; Fig. 14) caused partial melting of metasomatized SCLM and these fertile lower crustal sources, and gave rise to a suite of calc-alkaline to high-K calc-alkaline granitoids with high potential to form magmatic–hydrothermal porphyry deposits. Under more hydrous and oxidizing conditions ($\Delta FMQ > +1.5$; Wang et al., 2014a, 2014c), residual sulfides from prior arc magmatism left in the mantle or deep crust may have been remobilized, releasing metals into the melts and thus making them available for formation of post-subduction porphyry systems (Chiaradia et al., 2009; Richards, 2009; Tomkins et al., 2009; Lee et al., 2012; Richards and Mumin, 2013; Chiaradia, 2014; Wang et al., 2014b; Hou et al., 2015).

12. Conclusions

New lithogeochemical and Os–Sr–Nd–O–Hf isotopic data for Cenozoic igneous rocks collected from the 1600 km-long Gangdese magmatic belt reflect variable involvement of Indian plate lithosphere, subduction-modified Tibetan lithosphere, and asthenospheric mantle during the India–Asia collision, leading to different types of magmatism and association with porphyry Cu–Mo deposits along the belt. Paleocene–Eocene magmas throughout the Gangdese belt are typical of continental arc magmas, and likely formed in the final stages of Neo-Tethyan subduction, prior to slab breakoff. Later Oligo-Miocene magmas show a sharp longitudinal distinction of geochemical and isotopic compositions, and association with porphyry-type mineralization.

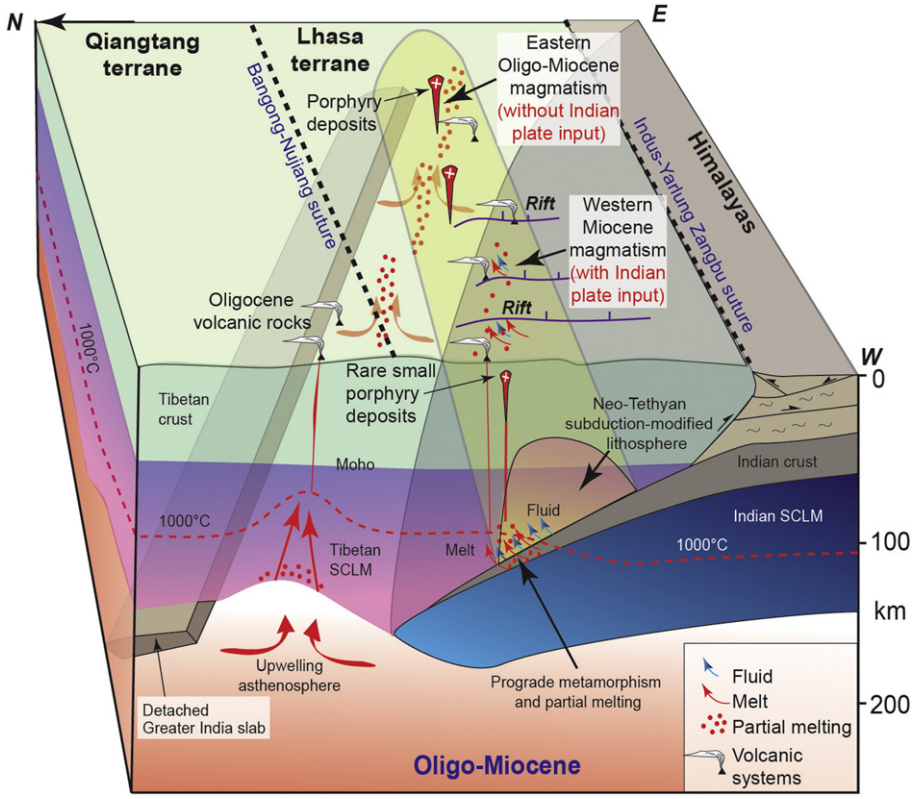

Fig. 14. Petrogenesis of late-collisional Oligo-Miocene igneous rocks in southern Tibet. The breakoff of Greater India slab started in the west at ~25 ± 5 Ma, and the tear propagated eastward until final detachment beneath eastern Tibet at ~10 ± 5 Ma (Van der Voo et al., 1999; Replumaz et al., 2010). This breakoff event triggered upwelling of asthenospheric melts and partial melting of the Tibetan SCLM, and produced a suite of Oligo-Miocene magmatism from west to east. The following underthrusting Indian lithosphere extended more in the western Gangdese belt. Prograde metamorphism Indian lithosphere released melts ± fluids into the Tibetan SCLM, and triggered its partial melting, then derived alkaline magmas ascended through rift zones. In contrast, the eastern Gangdese belt was not fully underthrust by Indian lithosphere in the Miocene. Upwelling of asthenospheric melts interacted with subduction-modified Tibetan lithosphere, and produced continental arc-like magmas and porphyry deposit systems. Thrust systems are inferred from Yin and Harrison (2000). Depths of the Moho, Indian lithosphere–asthenosphere boundary, and Tibetan lithosphere–asthenosphere boundary are estimated from seismic studies (Kumar et al., 2006; Zhao et al., 2010; Shokoohi Razi et al., 2014). Abbreviations: SCLM = sub-continental lithospheric mantle.

Miocene high-K calc-alkaline to shoshonitic granitoids in western Tibet are characterized by crust-like $(^{187}Os/^{188}Os)_i$, high $(^{87}Sr/^{86}Sr)_i$, low εNd_i and εHf_i, and high zircon $\delta^{18}O$ values, suggesting that these magmas involved a large component of melts ± fluids from the underthrust Indian plate, and experienced high degrees of crustal contamination during emplacement. These magmas are infertile, and are only associated with one known small porphyry Cu–Mo deposit. High-K calc-alkaline to shoshonitic volcanic rocks in the western Gangdese belt have extremely low εNd_i values (−7.1 to −17.4), crust-like zircon $\delta^{18}O$ values (+6.2–+8.8‰) and εHf_i values (−15.2 to 0.7), but low mantle-like $(^{187}Os/^{188}Os)_i$ ratios, and high Ni and Cr contents. We suggest that these magmas were derived from partial melting of the Tibetan SCLM but included ~3–25% melts ± fluids from the underthrust Indian plate.

Sparse high-K calc-alkaline to shoshonitic volcanic rocks in the eastern Gangdese belt are characterized by moderate εNd_i values (−9.4 to −3.4), mantle-like $(^{187}Os/^{188}Os)_i$ (0.154–0.210), and zircon $\delta^{18}O$ values (+5.0–+6.7‰) and εHf_i values (−5.9 to 10.1). These magmas are thought to have been derived largely from partial melting of enriched Tibetan SCLM, and show no evidence of an Indian plate source, suggesting that underthrusting had not extended this far east by the Miocene.

Oligo-Miocene granitoids in the eastern Gangdese belt are calc-alkaline to high-K calc-alkaline in compositions, and are characterized by similar $(^{87}Sr/^{86}Sr)_i$, εNd_i and zircon $\delta^{18}O$ values to the earlier Paleocene–Eocene igneous rocks. They were most likely derived from partial melting of juvenile (subduction modified) lower crust with mixing of enriched alkaline melts from highly metasomatized SCLM. These late-collisional magmas are hydrous and oxidized, and were able to remobilize Cu, Mo, and Au from deep crustal residues of prior arc magmatism, leading to a unique association with several large porphyry Cu–Mo deposits in eastern Tibet.

Supplementary data to this article can be found online at http://dx.doi.org/10.1016/j.earscirev.2015.07.003.

Acknowledgments

This study was funded by a Discovery Grant from the Natural Sciences and Engineering Research Council of Canada to Jeremy Richards, the Ministry of Science and Technology of China (973 project 2011CB403106), the China National Funds for Distinguished Scientists (No. 41302054) to Li-min Zhou, the IGCP/SIDA-600 Project (China), the National Natural Science Foundation Project (41303040) to Jing-jing Zhu, and student research grants from the Geological Society of America, and the Society of Economic Geologist Canada Foundation to Rui Wang. We thank Drs. Jin-xiang Li and Fang An for constructive discussions during their visit in the University of Alberta. Anna Oh, Huan-chun Qu, Qiu-yun Li, and Bo Xu are thanked for sample preparation.

Appendix A

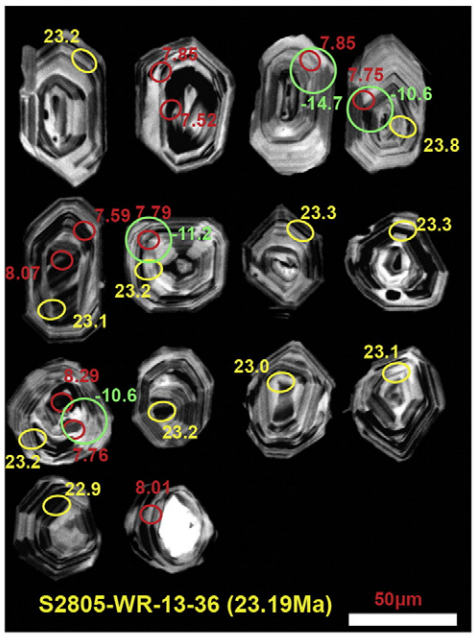

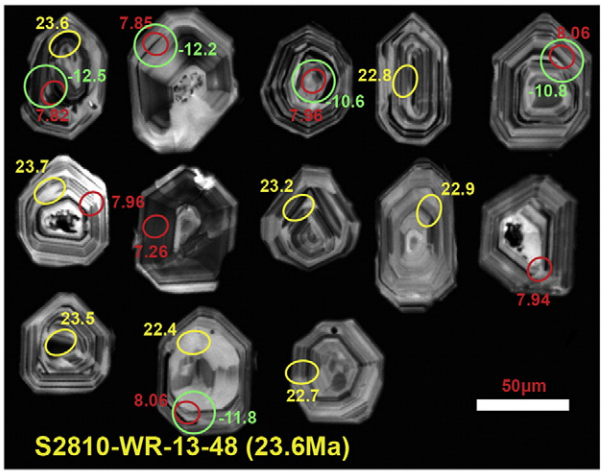

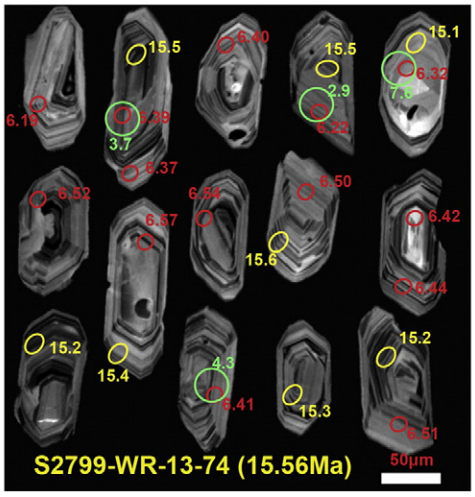

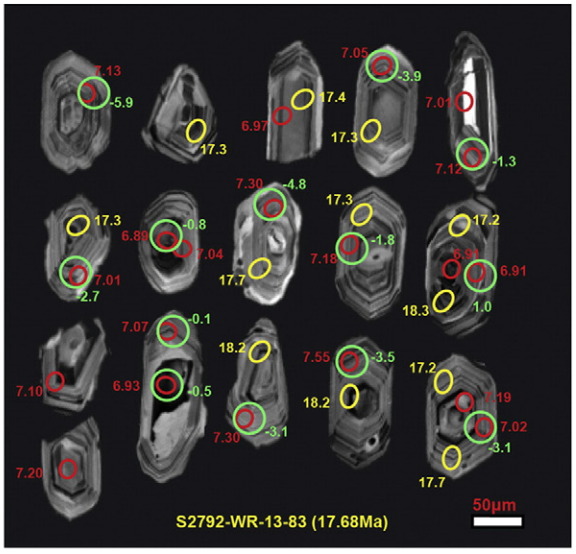

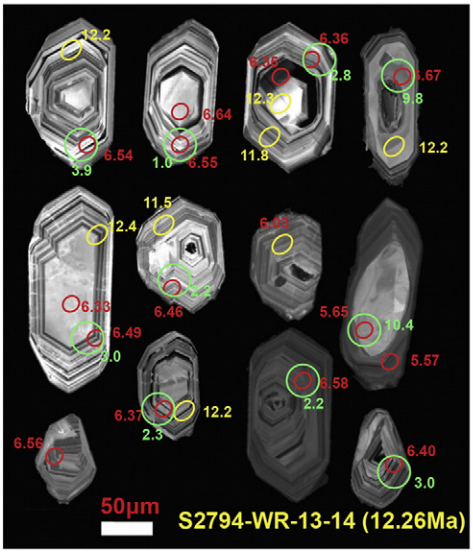

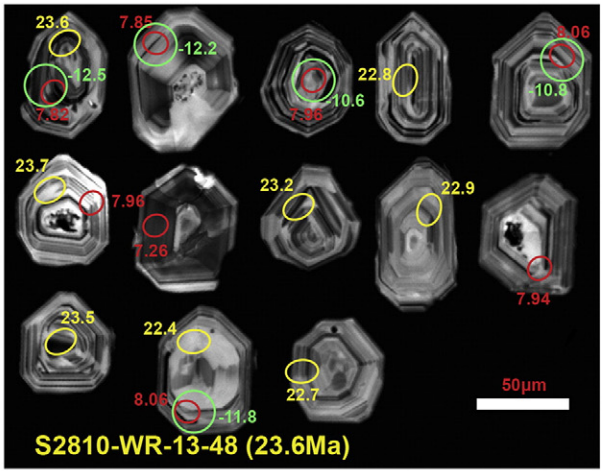

Fig. A1–A6. Cathodoluminescence images of representative analyzed zircons with in situ U–Pb (yellow circle), O (red circle), and Hf isotope (green circle) data for the Miocene igneous rocks in the Gangdese belt.

References

Aitchison, J.C., Ali, J.R., Davis, A.M., 2007. When and where did India and Asia collide. J. Geophys. Res. 112, B05423. http://dx.doi.org/10.1029/2006JB004706.

Ali, J.R., Aitchison, J.C., 2005. Greater India. Earth Sci. Rev. 72, 169–188.

Allégre, C.J., Courtillot, V., Taponnier, P., Hirn, A., Mattauer, M., Coulon, C., Jaeger, J.J., Achache, J., Schärer, U., Marcoux, J., Burg, J.P., Girardeau, J., Armijo, R., Gaiety, C., Göpel, C., Li, T., Xiao, X., Chang, C., Li, G., Lin, B., T.J., Wang, N., Chen, G., Han, T., Wang, X., Den, W., Sheng, H., Gao, Y., Zhou, J., Qiu, H., Bao, P., Wang, S., Wang, B., Zhou, Y., Xu, R., 1984. Structure and evolution of the Himalayan–Tibet orogenic belt. Nature 307, 17–22.

Arculus, R., Powell, R., 1986. Source component mixing in the regions of arc magma generation. J. Geophys. Res. 91, 5913–5926.

Armijo, R., Tapponnier, P., Mercier, J.L., Han, T.L., 1986. Quaternary extension in southern Tibet. Field observations and tectonic implications. J. Geophys. Res. 9, 13,803–13,872.

Black, L.P., Kamo, S.L., Allen, C.M., Davis, D., Aleinikoff, J.N., Valley, J.W., Mundil, R., Campbell, I.H., Korsch, R.J., Williams, I.S., Foudoulis, C., 2004. Improved $^{206}Pb/^{238}U$ microprobe geochronology by the monitoring of a trace-element-related matrix effect; SHRIMP, ID-TIMS, ELA–ICP-MS and oxygen isotope documentation for a series of zircon standards. Chem. Geol. 205, 115–140.

Blichert-Toft, J., Albarède, F., 1997. The Lu–Hf isotope geochemistry of chondrites and the evolution of the mantle–crust system. Earth Planet. Sci. Lett. 148, 243–258.

Blisniuk, P.M., Hacker, B.R., Glodny, J., Ratschbacher, L., Bi, S.W., Wu, Z.H., McWilliams, M.O., Calvert, A., 2001. Normal faulting in central Tibet since at least 13.5 Myr ago. Nature 412, 628–632.

Bohrson, W.A., Spera, F.J., 2001. Energy-constrained open-system magmatic processes II: application of energy-constrained assimilation-fractional crystallization (EC-AFC) model to magmatic systems. J. Petrol. 42, 1019–1041.

Burchfiel, B.C., Chen, Z., Royden, L.H., Liu, Y., Deng, C., 1991. Extensional development of Gabo valley, southern Tibet. Tectonophysics 194, 187–193.

Chan, G.H.N., Waters, D.J., Searle, M.P., Aitchison, J.C., Horstwood, M.S.A., Crowley, Q., Lo, C.H., Chan, J.S.L., 2009. Probing the basement of southern Tibet: evidence from crustal entrained in a Miocene ultrapotassic dyke. J. Geol. Soc. Lond. 166, 45–52.

Chazot, G., Lowry, D., Menzies, M., Mattey, D., 1997. Oxygen isotope compositions of hydrous and anhydrous mantle peridotite. Geochim. Cosmochim. Acta 61, 161–169.

Chen, T., 2006. Geochemistry of the Qushui intrusive of Gangdese in Tibet and its implications for magma mixing. Unpublished Master thesis (in Chinese), China University of Geosciences, Beijing, (59 pp.).

Chen, L., Qin, K.Z., Li, J.X., Xiao, B., Li, G.M., Zhao, J.X., Fan, X., 2011. Fluid inclusion and hydrogen, oxygen, sulfur isotopes of Nuri Cu–W–Mo deposit in the southern Gangdese, Tibet. Resour. Geol. 62, 42–62.

Chen, L., Qin, K.Z., Li, G.M., Li, J.X., Xiao, B., Jiang, H.Z., Zhao, J.X., Fan, X., Jiang, S.Y., 2012. Geological and skarn mineral characteristics of Nuri Cu–W–Mo deposit in southern Gangdese, Tibet. Mineral Deposits 31, 417–437 (in Chinese with English abstract).

Chiaradia, M., 2014. Copper enrichment in arc magmas controlled by overriding plate thickness. Nat. Geosci. 7, 43–46.

Chiaradia, M., Merino, D., Spikings, R., 2009. Rapid transition to long-lived deep crustal magmatic maturation and the formation of giant porphyry-related mineralization (Yanacocha, Peru). Earth Planet. Sci. Lett. 288, 505–515.

Chu, M.F., Chung, S.L., Song, B., Liu, D.Y., O'Reilly, S.Y., Pearson, N.J., Ji, J.Q., Wen, D.J., 2006. Zircon U–Pb and Hf isotope constraints on the Mesozoic tectonics and crustal evolution of southern Tibet. Geology 34, 745–748.

Chung, S.L., Liu, D., Ji, J.Q., Chu, M.F., Lee, H.Y., Wen, D.J., Lo, C.H., Lee, T.Y., Qian, Q., Zhang, Q., 2003. Adakites from continental collision zones: melting of thickened lower crust beneath southern Tibet. Geology 31, 1021–1024.

Chung, S.L., Chu, M.F., Zhang, Y.Q., Xie, Y.W., Lo, C.H., Lee, T.Y., Lan, C.Y., Li, X.H., Zhang, Q., Wang, Y.Z., 2005. Tibetan tectonic evolution inferred from spatial and temporal variations in post-collisional magmatism. Earth Sci. Rev. 68, 173–196.

Clayton, R.N., Mayeda, T.K., 1963. The use of bromine penta-fluoride in the extraction of oxygen from oxide and silicates for isotope analysis. Geochim. Cosmochim. Acta 27, 43–52.

Cogan, M.J., Nelson, K.D., Kidd, W.S.F., Wu, C.D., Project INDEPTH Team, 1998. Shallow structure of the Yadong–Gulu rift, southern Tibet, from refraction analysis of Project INDEPTH common midpoint data. Tectonics 17, 46–61.

Copley, A., Avouac, J.P., Wernicke, B.P., 2012. Evidence for mechanical coupling and strong Indian lower crust beneath southern Tibet. Nature 472, 79–81.

Creaser, R.A., Papanastassiou, D.A., Wasserburg, G.J., 1991. Negative thermal ion mass spectrometry of osmium, rhenium and iridium. Geochim. Cosmochim. Acta 55, 397–404.

Creaser, R.A., Erdmer, P., Stevens, R.A., Grant, S.L., 1997. Tectonic affinity of Nisutlin and Anvil assemblage strata from the Teslin tectonic zone, northern Canadian Cordillera. Constraints from neodymium isotope and geochemical evidence. Tectonics 16, 107–121.

Creaser, R.A., Grutter, H., Carlson, J., Crawford, B., 2004. Macrocrystal phlogopite Rb–Sr dates for the Ekati property kimberlites, Slave Province, Canada: evidence for multiple intrusive episodes in the Paleocene and Eocene. Lithos 76, 399–414.

Davidson, J., Turner, S., Handley, H., Macpherson, C.G., Dosseto, A., 2007. Amphibole "sponge" in arc crust? Geology 35, 787–790.

de Sigoyer, J., Chavagnac, V., Blichert-Toft, J., Villa, I.M., Luais, B., Guillot, S., Cosca, M., Mascle, G., 2000. Dating the Indian continental subduction and collision thickening in the northwest Himalaya: multichronology of the Tso Morari eclogites. Geology 28, 487–490.

Defant, M.J., Drummond, M.S., 1990. Derivation of some modern arc magmas by melting of young subducted lithosphere. Nature 347, 662–665.

DePaolo, D.J., 1980. Trace element and isotopic effects of combined wallrock assimilation and fractional crystallization. Earth Planet. Sci. Lett. 53, 189–202.

Dickin, A.P., 2005. Radiogenic Isotope Geology. 2nd edition. Cambridge University Press (492 pp.).

Ding, L., Kapp, P., Zhong, D., Deng, W., 2003. Cenozoic volcanism in Tibet: evidence for a transition from oceanic to continental subduction. J. Petrol. 44, 1833–1865.

Dong, G.C., 2002. Linzizong volcanic rocks and implications for probing India–Eurasia collision process in Linzhou Volcanic Basin, Tibet. Unpublished Ph.D. Thesis, China University of Geosciences, Beijing, (150 pp. (in Chinese with English abstract)).

Dong, G.C., Mo, X.X., Zhu, D.C., Wang, L.L., Chen, T., Li, B., 2006a. Magma mixing in middle part of Gangdese magma belt: evidences from granitoid complex. Acta Petrol. Sin. 22, 835–844 (in Chinese with English abstract).

Dong, G.C., Mo, X.X., Zhao, Z.D., Zhu, D.C., Song, Y.T., Wang, L., 2006b. Gabbros from southern Gangdese: implication for mass exchange between mantle and crust. Acta Petrol. Sin. 24, 203–210 (in Chinese with English abstract).

Du, A.D., Wu, S.Q., Sun, D.Z., Wang, S.X., Qu, W.J., Markey, R., Stein, H., Morgan, J., Malinovskiy, D., 2004. Preparation and certification of Re–Os dating reference materials: molybdenite HLP and JDC. Geostand. Geoanal. Res. 28, 41–52.

Eiler, J.M., 2001. Oxygen isotope variations of basaltic lavas and upper mantle rocks. In: Valley, J.W., Cole, D.R. (Eds.), Stable Isotope GeochemistryRev. Mineral. Geochem. 43, 319–364.

France-Lanord, C., Sheppard, S.M.F., Le Fort, P., 1988. Hydrogen and oxygen isotope variations in the High Himalaya peraluminous Manaslu leucogranites: evidence for heterogeneous sedimentary source. Geochim. Cosmochim. Acta 52, 513–526.

Gao, Y.F., Hou, Z.Q., Kamber, B., Wei, R.H., Meng, X.J., Zhao, R.S., 2007. Adakite-like porphyries from the southern Tibetan continental collision zones: evidence for slab melt metasomatism. Contrib. Mineral. Petrol. 153, 105–120.

Gao, Y.F., Wei, R.H., Hou, Z.Q., Tian, S.H., Zhao, R.S., 2008. Eocene high-MgO volcanism in southern Tibet. New constraints for mantle source characteristics and deep process. Lithos 105, 63–72.

Gao, Y.F., Yang, Z.S., Santosh, M., Hou, Z.Q., Wei, R.H., Tian, S.H., 2010. Adakitic rocks from slab melt-modified mantle sources in the continental collision zone of southern Tibet. Lithos 119, 651–663.

Gramlich, J.W., Murphy, T.J., Garner, E.L., Shields, W.R., 1973. Absolute isotopic abundance ratio and atomic weight of a reference sample of rhenium. J. Res. Natl. Bur. Stand. 77A, 691–698.

Green, T.H., Pearson, N.J., 1985. Experimental determination of REE partition coefficients between amphibole and basaltic to andesitic liquids at high pressure. Geochim. Cosmochim. Acta 49, 1465–1468.

Griffin, W.L., Wang, X., Jackson, S.E., Pearson, N.J., O'Reilly, S.Y., Xu, X., Zhou, X., 2002. Zircon chemistry and magma mixing, SE China: in-situ analysis of Hf isotopes, Tonglu and Pingtan igneous complexes. Lithos 61, 237–269.

Guo, Z.F., Wilson, M., Liu, J.Q., 2007. Post-collisional adakites in south Tibet: products of partial melting of subduction-modified lower crust. Lithos 96, 205–224.

Guo, Z.F., Wilson, M., Zhang, M.L., Cheng, Z.H., Zhang, L.H., 2013. Post-collisional, K-rich mafic magmatism in south Tibet: constraints on Indian slab-to-wedge transport processes and plateau uplift. Contrib. Mineral. Petrol. 165, 1311–1340.

Harris, N.B.W., Pearce, J.A., Tindle, A.G., 1986. Geochemical characteristics of collisional-zone magmatism. In: Coward, M.P., Reis, A.C. (Eds.), Collision TectonicsGeol. Soc. Lond., Spec. Publ. 19, 67–81.

Harrison, T.M., Yin, A., Grove, M., Lovera, O.M., 2000. The Zedong window: a record of superposed Tertiary convergence in southeastern Tibet. J. Geophys. Res. 105, 19,211–19,230.

Hébert, R., Guilmette, C., Dostal, J., Bezard, R., Lesage, G., Bédard, É., Wang, C.S., 2014. Miocene post-collisional shoshonites and their crustal xenoliths, Yarlung Zangbo Suture Zone southern Tibet: geodynamic implications. Gondwana Res. 25, 1263–1271.

Hou, Z.Q., Gao, Y.F., Qu, X.M., Rui, Z.Y., Mo, X.X., 2004. Origin of adakitic intrusives generated during mid-Miocene east–west extension in southern Tibet. Earth Planet. Sci. Lett. 220, 139–155.

Hou, Z.Q., Yang, Z.M., Qu, X.M., Meng, X.J., Li, Z.Q., Beaudoin, G., Rui, Z.Y., Gao, Y.F., Zaw, K., 2009. The Miocene Gangdese porphyry copper belt generated during post-collisional extension in the Tibetan Orogen. Ore Geol. Rev. 36, 25–31.

Hou, Z.Q., Zheng, Y.C., Yang, Z.M., Rui, Z.Y., Zhao, Z.D., Jiang, S.H., Qu, X.M., Sun, Q.Z., 2012. Contribution of mantle components within juvenile lower-crust to collisional zone porphyry Cu systems in Tibet. Mineral. Deposita 48, 173–192.

Hou, Z.Q., Yang, Z.M., Lu, Y.J., Kemp, A., Zheng, Y.C., Li, Q.Y., Tang, J.X., Yang, Z.S., Duan, L.F., 2015. A genetic linkage between subduction- and collision-related porphyry Cu deposits in continental collision zones. Geology 43, 247–250.

Huang, G.C., Wu, F.T., Roecker, S.W., Sheehan, A.F., 2009. Lithospheric structure of the central Himalaya from 3-D tomographic imaging. Tectonophysics 475, 524–543.

Huang, K.X., Zheng, Y.C., Zhang, S., Li, W., Sun, Q.Z., Li, Q.Y., Liang, W., Fu, Q., Hou, Z.Q., 2012. LA–ICP-MS zircon U–Pb dating of two types of porphyry in the Yaguila mining area, Tibet. Acta Petrol. Mineral. 31, 348–360 (in Chinese with English abstract).

Inger, S., Harris, N., 1993. Geochemical constraints on leucogranite magmatism in the Langtang valley, Nepal Himalaya. J. Petrol. 34, 345–368.

Irvine, T.N., Baragar, W.R.A., 1971. A guide to the chemical classification of the common volcanic rocks. Can. J. Earth Sci. 8, 523–548.

Jaffey, A.H., Flynn, K.F., Glendenin, L.E., Bentley, W.C., Essling, A.M., 1971. Precision measurement of half-lives and specific activities of 235U and 238U. Phys. Rev. C: Nucl. Phys. 4, 1889–1906.

Ji, W.Q., Wu, F.Y., Chung, S.L., Li, J.X., Liu, C.Z., 2009. Zircon U–Pb geochronology and Hf isotopic constraints on petrogenesis of the Gangdese batholith, southern Tibet. Chem. Geol. 262, 229–245.

Kapp, P., Yin, A., Harrison, T.M., Ding, L., 2005. Cretaceous–Tertiary shorting, basin development, and volcanism in central Tibet. GSA Bull. 117, 865–878.

Kapp, P., DeCelles, P.G., Leier, A.L., Fabijanic, J.M., He, S., Pullen, A., Gehrels, G.E., Ding, L., 2007. The Gangdese retroarc thrust belt revealed. GSA Today 17, 4–10.

Kay, S.M., Mpodozis, C., 2001. Central Andean ore deposits linked to evolving shallow subduction systems and thickening crust. GSA Today 11, 4–9.
Kind, R., Yuan, X., 2010. Seismic images of the biggest crash on earth. Science 329, 1479–1480.
Kumar, P., Yuan, X., Kind, R., Ni, J., 2006. Imaging the colliding Indian and Asian lithospheric plates beneath Tibet. J. Geophys. Res. 111, B6. http://dx.doi.org/10.1029/2005JB003930.
Kyser, T.K., 1986. Stable isotope variations in the mantle. Mineralogical Society of America, Reviews in Mineralogy 16 pp. 141–164.
Le Maitre, R.W., 1989. A Classification of Igneous Rocks and Glossary of Terms. Blackwell Scientific Publications, Oxford (193 pp.).
Lee, H.Y., Chung, S.L., Lo, C.H., Ji, J., Lee, T.Y., Qian, Q., Zhang, Q., 2009. Eocene Neotethyan slab breakoff in southern Tibet inferred from the Linzizong volcanic record. Tectonophysics 477, 20–35.
Lee, H.Y., Chung, S.L., Ji, J.Q., Qian, Q., Gallet, S., Lo, Q.H., Lee, T.Y., Zhang, Q., 2011. Geochemical and Sr–Nd isotopic constraints on the genesis of the Cenozoic Linzizong volcanic successions, southern Tibet. J. Asian Earth Sci. 53, 96–114.
Lee, C.T.A., Luffi, P., Chin, E.J., Bouchet, R., Dasgupta, R., Morton, D.M., Le Roux, V., Yin, Q.Z., Jin, D., 2012. Copper systematics in arc magmas and implications for crust–mantle differentiation. Science 336, 64–68.
Leng, C.B., Zhang, X.C., Zhong, H., Hu, R.Z., Zhou, W.D., Li, C., 2013. Re–Os molybdenite ages and zircon Hf isotopes of the Gangjiang porphyry Cu–Mo deposits in the Tibetan orogen. Mineral. Deposita 48, 585–602.
Li, G.M., Qin, K.Z., Ding, K.S., Liu, T.P., Li, J.X., Wang, S.H., Jiang, S.Y., Zhang, X.C., 2006. Geology, Ar–Ar age and mineral assemblage of Eocene skarn Cu–Au ± Mo deposits in the southeastern Gangdese arc, Southern Tibet: implications for deep exploration. Resour. Geol. 56, 315–336.
Li, C., van der Hilst, R.D., Meltzer, A.S., Engdahl, E.R., 2008. Subduction of the Indian lithosphere beneath the Tibetan plateau and Burma. Earth Planet. Sci. Lett. 274, 157–168.
Li, J.X., Qin, K.Z., Li, G.M., Xiao, B., Chen, L., Zhao, J.X., 2011. Post-collisional ore-bearing adakitic porphyries from Gangdese porphyry copper belt, southern Tibet. Melting of thickened juvenile arc lower crust. Lithos 126, 264–277.
Liu, S., Hu, R.Z., Feng, C.X., Zou, H.B., Li, C., Chi, G.X., Peng, J.T., Zhong, H., Qi, L., Qi, Y.Q., Wang, T., 2008. Cenozoic high Sr/Y volcanic rocks in the Qiangtang terrane, northern Tibet: geochemical and isotopic evidence for the origin of delaminated lower continental melts. Geol. Mag. 145, 463–474.
Liu, C.Z., Wu, F.Y., Chung, S.L., Zhao, Z.D., 2011. Fragments of hot and metasomatized mantle lithosphere in Middle Miocene ultrapotassic lavas, southern Tibet. Geology 39, 923–926.
Liu, C.Z., Wu, F.Y., Chung, S.L., Li, Q.L., Sun, W.D., Ji, W.Q., 2014a. A 'hidden' ^{18}O-enriched reservoir in the sub-arc mantle. Sci. Rep. 4, 4232. http://dx.doi.org/10.1038/srep04232.
Liu, D., Zhao, Z.D., Zhu, D.C., Niu, Y.L., Harrison, T.M., 2014b. Zircon xenocrysts in Tibetan ultrapotassic magmas: imaging the deep crust through time. Geology 42, 43–46.
Luck, J.M., Allègre, C.J., 1983. ^{187}Re–^{187}Os systematics in meteorites and cosmochemical consequence. Nature 302, 130–132.
Ludwig, K.R., 2009. SQUID2: A User's Manual, Rev. 12 Apr, 2009. Berkeley Geochronology Center Special Publication v. 5 (110 pp. http://www.bgc.org/isoplot_etc/squid/SQUID2_5Manual.pdf).
Ludwig, K.R., 2012. Isoplot 3.75: A Geochronological Toolkit for Microsoft Excel. Berkeley Geochronology Center Special Publication v. 5 (75 pp. http://www.bgc.org/isoplot_etc/isoplot/Isoplot3_75-4_15manual.pdf).
Martin, H., 1999. Adakitic magmas: modern analogues of Archaean granitoids. Lithos 46, 411–429.
Mattey, D.P., Lowry, D., Macpherson, C.G., Chazot, G., 1994a. Oxygen isotope compositions of mantle minerals by laser fluorination analysis: homogeneity in peridotite, heterogeneity in eclogites. Mineral. Mag. 58A, 573–574.
Mattey, D., Lowry, D., Macpherson, C.G., 1994b. Oxygen isotope composition of mantle peridotite. Earth Planet. Sci. Lett. 128, 231–241.
Meisel, T., Walker, R.J., Irving, A.J., Lorand, J.P., 2001. Osmium isotopic compositions of mantle xenoliths: a global perspective. Geochim. Cosmochim. Acta 65, 1311–1323.
Meng, J., Wang, C.S., Zhao, X.X., Coe, R., Li, Y.L., Finn, D., 2012. India–Asia collision was at 24° N and 50 Ma: paleomagnetic proof from southern Asia. Sci. Rep. 2, 925. http://dx.doi.org/10.1038/srep00925.
Middlemost, E.A.K., 1994. Naming materials in the magma/igneous rock system. Earth Sci. Rev. 37, 215–224.
Miller, C., Schuster, R., Klotzli, U., Mair, V., Frank, W., Purtscheller, F., 1999. Post-collisional potassic and ultrapotassic magmatism in SW Tibet: geochemical Sr–Nd–Pb–O isotopic constraints for mantle source characteristics and petrogenesis. J. Petrol. 40, 1399–1424.
Mo, X.X., Dong, G.C., Zhao, Z.D., Guo, T.Y., Wang, L.L., Chen, T., 2005. Timing of magma mixing in the Gangdese magmatic belt during the India–Asia collision: zircon SHRIMP U–Pb dating. Acta Geol. Sin. 79, 66–76.
Mo, X.X., Hou, Z.Q., Niu, Y.L., Dong, G.C., Zhao, Z.D., Yang, Z.M., 2007. Mantle contributions to crustal thickening during continental collision: evidence from Cenozoic igneous rocks in southern Tibet. Lithos 96, 225–242.
Mo, X.X., Niu, Y.L., Dong, G.C., Zhao, Z.D., Hou, Z.Q., Zhou, S., Ke, S., 2008. Contribution of syncollisional felsic magmatism to continental crust growth: a case study of the Paleogene Linzizong volcanic succession in southern Tibet. Chem. Geol. 250, 49–67.
Müntener, O., Kelemen, P.B., Grove, T.L., 2001. The role of H_2O during crystallization of primitive arc magmas under uppermost mantle conditions and genesis of igneous pyroxenites: an experimental study. Contrib. Mineral. Petrol. 141, 643–658.
Naney, M.T., 1983. Phase equilibria of rock-forming ferromagnesian silicates in granitic systems. Am. J. Sci. 283, 993–1033.
Niu, Y.L., Zhao, Z.D., Zhu, D.C., Mo, X.X., 2013. Continental collision zones are primary site for net continental crust growth — a testable hypothesis. Earth Sci. Rev. 127, 96–110.
Pan, G.T., Ding, J., Yao, D., Wang, L., 2004, The guide book of 1:1,500,000 geologic map of the Qinghai–Xizang (Tibet) plateau and adjacent areas. Chengdu Cartographic Publishing House, (44 pp. (in Chinese)).
Pearce, J.A., 1982. Trace element characteristics of lavas from destructive plate boundaries. In: Thorp, R.S. (Ed.), Andesites. Orogenic Andesites and Related Rocks. John Wiley and Sons, New York (724 pp.).
Perfit, M.R., Gust, D.A., Bence, A.E., Arculus, R.J., Taylor, S.R., 1984. Chemical characteristics of island arc basalts: implication for mantle sources. Chem. Geol. 30, 227–256.
Qu, X., Hou, Z., Li, Y., 2004. Melt components derived from a subducted slab in late orogenic ore-bearing porphyries in the Gangdese copper belt, southern Tibetan Plateau. Lithos 74, 131–148.
Qu, X., Hou, Z., Khin, Z., Li, Y., 2007. Characteristics and genesis of Gangdese porphyry copper deposits in the southern Tibetan Plateau: preliminary geochemical and geochronological results. Ore Geol. Rev. 31, 205–223.
Replumaz, A., Negredo, A.M., Villaseñor, A., Guillot, S., 2010. Indian continental subduction and slab breakoff during Tertiary collision. Terra Nova 22, 290–296.
Richards, J.P., 2009. Postsubduction porphyry Cu–Au and epithermal Au deposits: products of remelting of subduction-modified lithosphere. Geology 37, 247–250.
Richards, J.P., Mumin, H., 2013. Lithospheric Fertilization and Mineralization by Arc Magmas: Genetic Links and Secular Differences Between Porphyry Copper ± Molybdenum ± Gold and Magmatic–Hydrothermal Iron Oxide Copper–Gold Deposits. Society of Economic Geologists, Special Publications 17 pp. 277–299.
Richards, J.P., Jourdan, F., Creaser, R.A., Maldonado, G., DuFrane, S.A., 2013. Geology, geochemistry, geochronology, and economic potential of Neogene volcanic rocks in the Laguna Pedernal and Salar de Aguas Calientes segments of the Archibarca lineament, northwest Argentina. J. Volcanol. Geotherm. Res. 258, 47–73.
Rickwood, P.C., 1989. Boundary lines within petrologic diagrams which use oxides of major and minor elements. Lithos 22, 247–263.
Ridolfi, F., Renzulli, A., Puerini, M., 2010. Stability and chemical equilibrium of amphibole in calc-alkaline magmas: an overview, new thermobarometric formulations and application to subduction-related volcanoes. Contrib. Mineral. Petrol. 160, 45–66.
Rollinson, H., 1993. Using Geochemical Data: Evaluation, Presentation, Interpretation. Pearson Education Limited, Harlow, England (352 pp.).
Rooney, T.O., Franceschi, P., Hall, C.M., 2011. Water-saturated magmas in the Panama Canal region: a precursor to adakite-like magma generation? Contrib. Mineral. Petrol. 161, 373–388.
Scherer, E., Munker, C., Mezger, K., 2001. Calibration of the lutetium–hafnium clock. Science 293, 683–686.
Schmidberger, S.S., Heaman, L.M., Simonetti, A., Creaser, C.A., Whiteford, S., 2007. Lu-Hf, in-situ Sr and Pb isotope and trace element systematics for mantle eclogites from the Diavik diamond mine: evidence for Paleoproterozoic subduction beneath the Slave craton, Canada. Earth Planet. Sci. Lett. 254, 55–68.
Shirey, S.B., Walker, R.J., 1998. The Re–Os isotope system in cosmochemistry and high temperature geochemistry. Annu. Rev. Earth Planet. Sci. 26, 423–500.
Shokoohi Razi, A., Levin, V., Roecker, S.W., Huang, G.D., 2014. Crustal and uppermost mantle structure beneath western Tibet using seismic traveltime tomography. Geochem. Geophys. Geosyst. 15, 434–452.
Spera, F.J., Bohrson, W.A., 2001. Energy-constrained open-system magmatic processes I: general model and energy-constrained assimilation and fractional crystallization (EC-AFC) formulation. J. Petrol. 42, 999–1018.
Stacey, J.S., Kramers, J.D., 1975. Approximation of terrestrial lead isotope evolution by a two-stage model. Earth Planet. Sci. Lett. 26, 207–221.
Stern, R.A., Amelin, Y., 2003. Assessment of errors in SIMS zircon U–Pb geochronology using a natural zircon standard and NIST SRM 610 glass. Chem. Geol. 197, 111–146.
Stern, R.A., Ickert, R.B., 2010. Zircon oxygen isotopes by SIMS: performance evaluation of the Canadian IMS1280. Geochim. Cosmochim. Acta 74, A993.
Sun, S.S., McDonough, W.F., 1989. Chemical and isotopic systematics of oceanic basalts: implications for mantle composition and processes. Geol. Soc. Lond. Spec. Publ. 42, 313–345.
Tanaka, T., Togashi, S., Kamioka, H., Amakawa, H., Kagami, H., Hamamoto, T., Yuhara, M., Orihashi, Y., Yoneda, S., Shimizu, H., Kunimaru, T., Takahashi, K., Yanagi, T., Nakano, T., Fujimaki, H., Shinjo, R., Asahara, Y., Tanimizu, M., Dragusanu, C., 2000. JNdi-1: a neodymium isotopic reference in consistency with La Jolla neodymium. Chem. Geol. 168, 279–281.
Tapponnier, P., Xu, Z.Q., Roger, F., Meyer, B., Arnaud, N., Wittlinger, G., Yang, J.S., 2001. Oblique stepwise rise and growth of the Tibet plateau. Science 294, 1671–1677.
Tomkins, A.G., Weinberg, R.F., McFarlane, C.R.M., 2009. Preferential magma extraction from K- and metal-enriched source regions in the crust. Mineral. Deposita 44, 171–181.
Turner, S., Arnaud, N., Liu, J., Rogers, N., Hawkesworth, C., Harris, N., Kelley, S., 1996. Post-collision, shoshonitic volcanism on the Tibetan Plateau: implications for convective thinning of the lithosphere and the source of ocean island basalts. J. Petrol. 37, 45–71.
Unterschutz, J.L.E., Creaser, R.A., Erdmer, P., Thompson, R.I., Daughtry, K.L., 2002. North American margin origin of Quesnel terrane strata in the southern Canadian Cordillera: inferences from geochemical and Nd isotopic characteristics of Triassic metasedimentary rocks. Geol. Soc. Am. Bull. 114, 462–475.
Valley, J.W., Chiarenzelli, J.R., McLelland, J.M., 1994. Oxygen isotope geochemistry of zircon. Earth Planet. Sci. Lett. 126, 187–206.
Valley, J.W., Kinny, P.D., Schulze, D.J., Spicuzza, M.J., 1998. Zircon megacrysts from kimberlite: oxygen isotope variability among mantle melts. Contrib. Mineral. Petrol. 133, 1–11.
Valley, J.W., Lackey, J.S., Cavosie, A.J., Clechenko, C.C., Spicuzza, M.J., Basei, M.A.S., Bindeman, I.N., Ferreira, V.P., Sial, A.N., King, E.M., Peck, W.H., Sinha, A.K., Wei, C.S., 2005. 4.4 billion years of crustal maturation: oxygen isotope ratios of magmatic zircon. Contrib. Mineral. Petrol. 150, 561–580.

Van der Voo, R., Spakman, W., Bijwaard, H., 1999. Tethyan subducted slabs under India. Earth Planet. Sci. Lett. 171, 7–20.
van Hinsbergen, D.J.J., Lippert, P.C., Dupont-Nivet, G., McQuarrie, N., Doubrovine, P.V., Spakman, W., Torsvik, T.H., 2012. Greater India basin hypothesis and a two-stage Cenozoic collision between India and Asia. Proc. Natl. Acad. Sci. U. S. A. 20, 7659–7664.
Vervoort, J.D., Patchett, P.J., 1996. Behavior of hafnium and neodymium isotopes in the crust: constraints from Precambrian crustally derived granites. Geochim. Cosmochim. Acta 60, 3717–3733.
Völkening, J., Walczyk, T., Heumann, K.G., 1991. Osmium isotope ratio determinations by negative thermal ion mass spectrometry. Int. J. Mass Spectrom. Ion Process. 105, 147–159.
Wang, S.F., Wang, C., Phillips, R.J., Murphy, M.A., Fang, X.M., Yue, Y.H., 2012. Displacement along the Karakoram fault, NW Himalaya, estimated from LA–ICP-MS U–Pb dating of offset geologic markers. Earth Planet. Sci. Lett. 337–338, 156–163.
Wang, R., Richards, J.P., Hou, Z.Q., Yang, Z.M., DuFrane, S.A., 2014a. Increased magmatic water content—the key to Oligo-Miocene porphyry Cu–Mo ± Au formation in the eastern Gangdese belt, Tibet. Econ. Geol. 109, 1315–1339.
Wang, R., Richards, J.P., Hou, Z.Q., Yang, Z.M., 2014b. Extent of underthrusting of the Indian plate beneath Tibet controlled the distribution of Miocene porphyry Cu–Mo ± Au deposits. Mineral. Deposita 49, 165–173.
Wang, R., Richards, J.P., Hou, Z.Q., Yang, Z.M., Gou, Z.B., DuFrane, S.A., 2014c. Increasing magmatic oxidation state from Paleocene to Miocene in the eastern Tibetan Gangdese belt: implication for collision-related porphyry Cu–Mo ± Au mineralization. Econ. Geol. 109, 1943–1965.
Wang, R., Richards, J.P., Hou, Z.Q., An, F., Creaser, R.A., 2015. Zircon U–Pb age and Sr–Nd–Hf–O isotope geochemistry of the Paleocene-Eocene igneous rocks in western Gangdese: evidence for the timing of Neo-Tethyan slab breakoff. Lithos 224–225, 179–194.
Wasserburg, G.J., Jacobsen, S.B., DePaolo, D.J., McCulloch, M.T., Wen, T., 1981. Precise determination of Sm/Nd ratio, Sm, Nd isotopic abundances in standard solutions. Geochim. Cosmochim. Acta 45, 2311–2323.
Wen, D.R., 2007. The Gangdese batholith, Southern Tibet. Ages, geochemical characteristics and petrogenesis. Unpublished Ph.D. thesis, National Taiwan University, (120 pp.).
White, L.T., Ahmad, T., Ireland, T.R., Lister, G.S., Forster, M.A., 2011. Deconvolving episodic age spectra from zircons of the Ladakh batholith, northwest Indian Himalaya. Chem. Geol. 289, 179–196.
Widow, E., Hoernle, K.A., Shirey, S.B., Schmincke, H.U., 1999. Os isotope systematics in the Canary Islands and Madeira: lithospheric contamination and mantle plume signatures. J. Petrol. 40, 279–296.
Williams, H.M., 2000. Magmatic and tectonic evolution of Southern Tibet and the Himalaya (Ph.D. thesis), The Open University (329 pp.).
Williams, H.M., Turner, S.P., Pearce, J.A., Kelley, S.P., Harris, N.B.W., 2004. Nature of the source regions for post-collisional, potassic magmatism in southern and northern Tibet from geochemical variations and inverse trace element modeling. J. Petrol. 45, 555–607.
Wu, F.Y., Yang, Y.H., Xie, L.W., Yang, J.H., Xu, P., 2006. Hf isotopic compositions of the standard zircons and baddeleyites used in U–Pb geochronology. Chem. Geol. 234, 105–126.
Wu, S., Zheng, Y.Y., Sun, X., Liu, S.A., Geng, R.R., You, Z.M., Ouyang, H.T., Lei, D., Zhao, Z.Y., 2014. Origin of the Miocene porphyries and their mafic microgranular enclaves from Dabu porphyry Cu–Mo deposit, southern Tibet: implications for magma mixing/mingling and mineralization. Int. Geol. Rev. 56, 571–595.
Yang, Z. M., 2008. The Qulong giant porphyry copper deposit in Tibet. Magmatism and mineralization. Unpublished Ph.D. thesis, Institute of Geology Chinese Academy of Geological Sciences, Beijing, (144 pp. (in Chinese with English abstract)).
Yang, Z.M., Hou, Z.Q., White, N.C., Chang, Z.S., Li, Z.Q., Song, Y.C., 2009. Geology of the post-collisional porphyry copper–molybdenum deposit at Qulong, Tibet. Ore Geol. Rev. 36, 133–159.
Yang, Z.M., Lu, Y.J., Hou, Z.Q., Chang, Z.S., 2015. High-Mg diorite from Qulong in Southern Tibet: implications for the genesis of adakite-like intrusions and associated porphyry Cu deposits in collisional orogens. J. Petrol. 56, 227–254.
Yin, A., Harrison, T.M., 2000. Geologic evolution of the Himalayan–Tibetan orogen. Annu. Rev. Earth Planet. Sci. 28, 211–280.
Ying, L.J., Wang, C.S., Tang, J.X., Wang, D.H., Qu, W.J., Li, C., 2014. Re–Os systematics of sulfides (chalcopyrite, bornite, pyrite and pyrrhotite) from the Jima Cu–Mo deposit of Tibet, China. J. Asian Earth Sci. 79, 497–506.
Yu, F., Hou, Z.Q., Zhao, Z.D., Zheng, Y.C., Li, Q.Y., Duan, L.F., 2013. Geochemistry and origin of Yare complex in western Tibet: constraints from Zircon U–Pb dating and Hf–O isotopic compositions. 2013's National Symposium on Petrology and Geodynamics Abstract, pp. 521–522 (in Chinese).
Yuan, H.L., Gao, S., Dai, M.N., Zong, C.L., Günther, D., Fontaine, G.H., Liu, X.M., Diwu, C., 2008. Simultaneous determinations of U–Pb age, Hf isotopes and trace element compositions of zircon by excimer laser-ablation quadrupole and multiple-collector ICP-MS. Chem. Geol. 247, 100–118.
Zellmer, G.F., Iizuka, Y., Miyoshi, M., Tamura, Y., Tatsumi, Y., 2012. Lower crustal H_2O controls on the formation of adakitic melts. Geology 40 (6), 487–490.
Zhang, S., Zheng, Y., Huang, K., Li, W., Sun, Q., Li, Q., Fu, Q., Liang, W., 2012. Re–Os dating of molybdenite from Nuri Cu–W–Mo deposit and its geological significance. Mineral Deposits 31, 337–346 (in Chinese with English abstract).
Zhang, Z.M., Dong, X., Santosh, M., Zhao, G.C., 2013. Metamorphism and tectonic evolution of the Lhasa terrane, Central Tibet. Gondwana Res. 25, 170–189.
Zhao, Z.D., Mo, X.X., Dilek, Y., Niu, Y.L., DePaolo, D.J., Robinson, P., Zhu, D.C., Sun, C.G., Dong, G.C., Zhou, S., Luo, Z.H., Hou, Z.Q., 2009. Geochemical and Sr–Nd–Pb–O isotopic compositions of the post-collisional ultrapotassic magmatism in SW Tibet: petrogenesis and implications for India-continental subduction beneath southern Tibet. Lithos 113, 190–212.
Zhao, J., Yuan, X., Liu, H., Kumar, P., Pei, S., Kind, R., Zhang, Z., Teng, J., Ding, L., Gao, X., Xu, Q., Wang, W., 2010. The boundary between the Indian and Asian tectonic plates below Tibet. Proc. Natl. Acad. Sci. U. S. A. 107, 11229–11233.
Zhao, J.X., Qin, K.Z., Li, G.M., Li, J.X., Xiao, B., Chen, L., 2011. Geochemistry and petrogenesis of granitoids at Sharang Eocene porphyry Mo deposit in the main-stage of India–Asia continental collision, northern Gangdese, Tibet. Resour. Geol. 62, 84–98.
Zhao, J.X., Qin, K.Z., Li, G.M., Li, J.X., Xiao, B., Chen, L., Yang, Y.H., Li, C., Liu, Y.S., 2014. Collision-related genesis of the Sharang porphyry molybdenum deposit, Tibet: evidence from zircon U–Pb ages, Re–Os ages and Lu–Hf isotopes. Ore Geol. Rev. 56, 312–326.
Zheng, Y.Y., Duo, J., Cheng, S.B., Gao, S.B., Dai, F.H., 2007. Progress in porphyry copper exploration from the Gangdese belt, Tibet, China. Front. Earth Sci. China 1, 226–232.
Zheng, Y.C., Hou, Z.Q., Li, W., Liang, W., Huang, K.X., Li, Q.Y., Sun, Q.Z., Fu, Q., Zhang, S., 2012. Petrogenesis and geological implications of the Oligocene Chongmuda–Mingze adakite-like intrusions and their mafic enclaves, southern Tibet. J. Geol. 120, 647–669.
Zheng, Y.C., Hou, Z.Q., Gong, Y.L., Liang, W., Sun, Q.Z., Zhang, S., Fu, Q., Huang, K.Q., Li, Q.Y., Li, W., 2014a. Petrogenesis of Cretaceous adakite-like intrusions of the Gangdese plutonic belt, southern Tibet: implications for mid-ocean ridge subduction and crustal growth. Lithos 190–191, 240–263.
Zheng, Y.Y., Sun, X., Gao, S.B., Zhao, Z.D., Zhang, G.Y., Wu, S., You, Z.M., Li, J.D., 2014b. Multiple mineralization events at the Jiru porphyry copper deposit, southern Tibet: implications for Eocene and Miocene magma sources and resource potential. J. Asian Earth Sci. 79, 842–857.
Zhou, L.M., 2012. Research of Re–Os isotope system in intermediate–acidic rocks and the application in Tibetan plateau. Chinese Academy of Geological Science (Ph.D. thesis, 111 pp. (in Chinese with English abstract)).
Zhou, S., Mo, X.X., Zhao, Z.D., Qiu, R.Z., Zhang, S.Q., Guo, T.Y., 2004. ^{40}Ar–^{39}Ar geochronology of Yangying post-collisional volcanic rock south Tibet and its geological significance. Prog. Nat. Sci. 12, 1411–1488.
Zhou, S., Mo, X.X., Zhao, Z.D., Qiu, R.Z., Niu, Y.L., Guo, T.Y., Zhang, S.G., 2009. $^{40}Ar/^{39}Ar$ geochronology of post-collisional volcanism in the middle Gangdese belt, southern Tibet. J. Asian Earth Sci. 37, 246–258.
Zhou, L.M., Gao, B.Y., Wang, L.B., Li, C., Qu, W.J., Hou, Z.Q., Du, A.D., 2012. Improvements on the separation method of Osmium by direct distillation in Carius Tube. Rock Miner. Anal. 31, 413–418 (in Chinese with English abstract).
Zhu, D.C., Mo, X.X., Niu, Y.L., Zhao, Z.D., Wang, L.Q., Liu, Y.S., Wu, F.Y., 2009. Geochemical investigation of Early Cretaceous igneous rocks along an east–west traverse throughout the central Lhasa Terrane, Tibet. Chem. Geol. 268, 298–312.
Zhu, D.C., Mo, X.X., Zhao, Z.D., Niu, Y.L., Wang, L.Q., Chu, Q.H., Pan, G.T., Xu, J.F., Zhou, C.Y., 2010. Presence of Permian extension- and arc-type magmatism in southern Tibet: petrogeographic implications. Geol. Soc. Am. Bull. 122, 979–993.
Zhu, D.C., Zhao, Z.D., Niu, Y.L., Mo, X.X., Chung, S.L., Hou, Z.Q., Wang, L.Q., Wu, F.Y., 2011. The Lhasa terrane: record of a microcontinent and its histories of drift and growth. Earth Planet. Sci. Lett. 301, 241–255.
Zhu, D.C., Zhao, Z.D., Niu, Y.L., Dilek, Y., Hou, Z.Q., Mo, X.X., 2013. The origin and pre-Cenozoic evolution of the Tibetan Plateau. Gondwana Res. 23, 1429–1454.